PhD thesis

Damping and spin rectification in synthetic antiferromagnets

Muhammad Asmat Pervez

Centro Brasileiro de Pesquisas Físicas

2021

Orientador : Rubem Luís Sommer
Co- Orientador: Diego Ernesto González Chávez

"DAMPING AND SPIN RECTIFICATION IN SYNTHETIC ANTIFERROMAGNETS"

MUHAMMAD ASMAT PERVEZ

Tese de Doutorado em Física apresentada no Centro Brasileiro de Pesquisas Físicas do Ministério da Ciência Tecnologia e Inovação. Fazendo parte da banca examinadora os seguintes professores:

Rubem Luís Sommer – Presidente/Orientador/CBPF

Diego Ernesto González Chávez – Coorientador/CBPF

Roberto Bechara Muniz - UFF

Angela Burlamaqui Klautau– UFPA

Lucio Strazzabosco Dorneles - UFSM

Carlos César Bof Bufon – Inst. Presbiteriano Mackenzie

Rio de Janeiro, 05 de novembro de 2021.

Resumo

Nesta tese são estudados o amortecimento magnético e os efeitos de retificação de spin que ocorrem devido às correntes de spin em anti-ferromagnetos sintéticos (SAF). Estas propriedades foram estudadas usando técnicas de ressonância ferromagnética (FMR) de banda larga e medidas de voltagem DC gerado por ressonância ferromagnética. As amostras analisadas foram SAF simétricos NiFe/Ru/NiFe/NM baseados em Permalloy ($Ni_{81}Fe_{19}$), com espaçador de Rutênio (Ru) de diferentes espessuras, e com uma camada de cobertura não magnética (NM) de Ru, tântalo ou platina.

Para o estudo do amortecimento magnético, foram medidas as larguras de linha em frequência e em campo, para os modos de ressonância óptico e acústico do SAF, ao longo da toda a relação de dispersão, nos estados magnéticos saturados e não colineares. Os resultados obtidos foram comparados com um modelo baseado na equação de Landau Lifshitz Gilbert sem termos adicionais de bombeamento de spin ou torque induzido por transferência de spin. É mostrado que este modelo explica a maioria das caraterísticas observadas nas medidas de largura de linha em campo, com muita boa concordância para o modo acústico. Enquanto para o modo óptico é observado que a largura de linha medida é maior que a do modelo LLG. Estes resultados concordam com os reportados na literatura, onde é esperado que no modo acústico as correntes de spin entre as camadas sejam canceladas entre si, enquanto no modo óptico o aumento do amortecimento extra é explicado pelo bombeamento de spin entre as camadas do SAF. A contribuição desta tese é apresentar medidas detalhadas para as magnetizações não colineares, além de analisar o efeito do alargamento inomogêneo da linha de FMR nestas medidas.

No estudo da retificação de spin, foram identificados dois efeitos que geram voltagem DC: o

efeito inverso Hall de spin (ISHE) e a retificação por magneto resistência anisotrópica (AMR) transversal conhecida também como efeito Hall planar. Este segundo efeito acontece devido à geometria particular do nosso sistema de medida, onde a guia de onda tipo microstrip utilizada induz uma corrente de rádio frequência (RF) na amostra. É mostrado que o sinal do ISHE é observado para camadas finas de NiFe, enquanto para camadas maiores de 10 nm o efeito da AMR é dominante. A retificação de spin em SAFs foi medida para o modo acústico ao longo de toda a relação de dispersão, incluído o estado antiparalelo, não colinear e saturado. No estado não colinear é observada e analisada a inversão do sinal da voltagem DC quando a magnetização entre as camadas do SAF fazem um angulo de $90^{\underline{o}}$. O estado antiparalelo também gera um sinal de voltagem DC com um perfil antissimétrico em relação ao campo zero. Estes resultados são explicados pela retificação de uma corrente RF, induzida na amostra, devido à magneto resistência anisotrópica e tem como resultado a geração de uma voltagem DC transversal à direção da corrente.

Palavras chave

Dinâmica de magnetização , anti-ferromagnetos sintéticos, amortecimento magnético, retificação de spin.

Abstract

In this thesis the magnetic damping and spin rectification effects that occur due to spin currents in synthetic anti-ferromagnets (SAF) are studied. These properties were studied using broadband ferromagnetic resonance (FMR) techniques and measurements of DC voltage generated due to ferromagnetic resonance. The analyzed samples were symmetrical SAF NiFe/Ru/NiFe/NM based on Permalloy ($Ni_{81}Fe_{19}$), with Ruthenium (Ru) spacer of different thicknesses, and with a non-magnetic (NM) capping layer of Ru, tantalum or platinum.

For the study of magnetic damping, frequency and field line widths were measured in the optical and acoustic resonance modes of the SAF. These were carried along the entire dispersion relation, in the saturated and non-collinear magnetic states. The results obtained were compared with a model based on the Landau Lifshitz Gilbert equation without additional terms of spin pumping or spin transfer torque. It is shown that this model explains most of the characteristics observed in field linewidth measurements, with very good agreement for the acoustic mode. While for the optical mode it is observed that the measured linewidth is greater than the obtained from the LLG model. These results are in agreement with those reported in the literature. It is expected that in the acoustic mode the spin currents between the layers cancel each other, while in the optical mode the increase in extra damping is explained by the spin pumping between the layers of the SAF. The contribution of this thesis is to present detailed measurements for non-collinear magnetizations, in addition to analyze the effect of phenomenological inhomogeneous linewidth not predicted in the LLG model.

In the study of spin rectification, two effects that generate DC voltage were identified: the inverse spin Hall effect (ISHE) and the rectificationd due transverse anisotropic magneto re-

sistance (AMR), also known as the planar Hall effect (PHE). This second effect is due to the particular geometry of our measurement system, where the microstrip waveguide induces a radio frequency (RF) current in the sample. It is shown that typical ISHE signals are observed for NiFe thin layers, while for layers larger than 10 nm the AMR effect is dominant. Spin rectification in SAFs was measured for the acoustic mode over the entire dispersion relation, including the antiparallel, non-collinear and saturated state. In the non-collinear state, an inversion of the DC voltage signal is observed when the magnetization between the SAF layers makes an angle of 90^{o}. The antiparallel state also generates a DC voltage signal with an antisymmetric profile with respect to the zero field. These results are explained by the rectification of an RF current, induced in the sample, due to the anisotropic magneto resistance effect, which results in the generation of a DC voltage transverse to the current direction.

Keywords

Magnetization dynamics, synthetic anti-ferromagnets, magnetic damping, spin rectification.

Acknowledgement

All praises to ALLAH ALMIGHTY, The Creator and Sustainer of The Universe, The most gracious, The invincible and the all-wise. Darood o Salaam to His Holy Prophet Muhammad (Peace be upon Him), his family (RA) and his companions (RA).

This work would not have been possible without the help and support of many people, and I hereby would like to take the opportunity to thank them. First of all, my supervisor Professor Rubem Luís Sommer and Co supervisor Diego Gonzalez Chavez. Their enthusiasm for my project and constant believe in my abilities. They always encouraged my ideas, and gave me the freedom to realize them. I really enjoyed my discussions with my Co supervisor Diego Chavez , and highly appreciate that he always found time for me, also his help with simulation work, practical stuff or repairing lab equipment's. Then my colleagues in the campus and Post doctoral fellows, most notably B. G. Silva, Gabriela, Juciane, Adnan and Roberta Dutra. Thank you to my friends out of campus who made my stay in Rio de janeiro more enjoyable without them it was difficult. I would like to mention Carioca Cricket Club (CCC) for having amazing cricketing memories with them. Thank you to my Pakistani friends who give me the backup all the time, not a single moment I felt that I am away from my family, namely, Rafqat Ali, Adnan, Quaid Zaman, Khalil, Tahir Jan and hamza.

I would like to thank my parents, my family Hina Asmat, Amna Asmat, Ahmad Ali, Tehmina Iram, my uncles, Muhammad Shabbeer Saifi and Zafar Raja Qalander Saifi who gave me continuous attention and motivation during this period.

Finally , I would like you thanks Institute of Space Technology, Islamabad and Higher Education Commission (HEC), Pakistan for scholarship funds. furthermore, I am very grateful to

Post Graduate Office (COEDU) and their administrative staff for their technical support and the Brazilian funding agencies CNPq and CAPES.

Contents

1 Introduction

In a Ferromagnetic materials atoms are arranged in a lattice, and their magnetic moments interact each other to align themselves parallel to each other. The ferromagnetism effect is described in classical theory by the presence of a molecular field within the ferromagnetic material. This field is large enough to magnetize the material to saturation. In the 20th century, the quantum mechanics revealed the concept spin of electron. Many famous names comes e.g Pauli, Dirac, Fermi, Heisenberg, Bloch and Neel for the significant contributions to the theory of metals and magnetism. The Heisenberg model of ferromagnetism describes the parallel alignment of magnetic moments in terms of exchange interactions between neighboring moments. With the evolution of time, the phenomenon of giant magnetoresistance (GMR) was discovered by Baibich et al. in 1988 [1], then this concept is used to prepare spin valves and magnetic tunnel junction, thus introducing the new field, called spintronics, where spins of electrons are used to transfer information.

In spintronics, ferromagnetic materials have caught extensive interest due to their applications. Moreover, in recent times, the discovery of new ferromagnetic materials and exploration of their dynamic magnetic characteristics, open new horizons to develop and optimize the wide range of technological devices. [2–5].

Dynamical measurements provide a lot of information about magnetic materials [6]. They have an ability to determine the magnetic parameters (magnetization, bulk and surface anisotropies, exchange constants, dipole fields) of individual films and can also determine the strength of the exchange bias and Ruderman-Kittel-Kasuya-Yosida (RKKY) coupling. Dynamical measurements also give insight of one additional parameter, linewidth of resonance absorption that

characterizes the damping in the system. narrower is the linewidth, better will be the quality of ferromagnetic film.

At present, research on magnetic devices operating at high frequencies is at the peak. Particularly, spintronics devices with applications in sensing and data storage are used at frequencies comparable to the natural ferromagnetic resonance frequency. Complex magnetization dynamics relies on the anisotropy and non-uniformity of the magnetization, which are governed by structural properties of the samples [7]. Due to structural imperfections, we observe the magnetic noise and unpredictable magnetic responses in our spintronics devices, which alters the proper functioning of magnetic sensors [8–10]. This intensified the efforts to develop the soft magnetic materials with high magnetic homogeneity for fast magnetic switching or high frequency applications [8].

Ferromagnetic resonance (FMR) is one of the basic physical phenomena of soft magnetic materials, which dictates the operational speed of these magnetic materials in devices [11–13] . Radio-frequency (RF) and microwave devices based on FMR are extensively used in information, aerospace, communication and many other fields, where high FMR frequency f_r is required [14]. Broadband ferromagnetic resonance is a well understood experimental technique [15–18] which not only provides, information about the intrinsic and extrinsic magnetic properties but also gives insight about magnetic anisotropies, magnetization relaxation mechanisms, microscopic interactions and high frequency magnetic response of ferromagnetic thin films . Furthermore, due to broadband system, FMR system has great advantage on other techniques that the measurements can be performed without remounting the sample on different waveguides and cavities.

In this scenario, A synthetic antiferromagnet (SAF), which, consists of two magnetic layers, coupled antiferromagnetically through a thin metallic layer via the Ruderman-Kittel-Kasuya-Yosida (RKKY) interaction [19–25]. SAF systems are proved far better candidate in high frequency devices because of their thermal stability and easy to control in magnetic field [26, 27]. Moreover, SAF systems are important constituents of complex layered structures used in magnetic sensors, magnetic random access memories, nano-oscillators, and other spintronic

devices [28–34].

Concerning the magnetization dynamics, it is also important to analyze the two observed ferromagnetic resonance (FMR) modes: an in-phase precession (acoustical mode) and out-of-phase precession (optical mode) [35–38]. Until now, only the acoustic modes are well studied and employed in practical devices, while, optical modes are neglected because of their rather small permeability [39–41].

The linewidth is a fascinating feature in FMR measurements. There exists two kinds of linewidths, intrinsic linwidth, is due to damping and it is a fundamental property of the material, while the second is extrinsic linwidth due to magnetic inhomogeneities within the sample and the anisotropy dispersion in the film, it does not depend on the microwave frequency [42,43]. In all these applications the magnetic damping is an important issues defining the performance and general behavior [44]. To analyze damping is important to take into account the magnetization states, where the relative angle between the magnetizations defines three magnetic regions: saturation, spin-flop and antiparallel. [27, 45–47].

It is well established that FMR in SAF systems produces spin currents through the non-magnetic spacer, resulting in spin pumping and spin transfer torque effects. Spin pumping theory predicts enhancement on the magnetic damping when the ferromagnetic layers oscillate with different amplitudes or opposite phases [48–52]. This behavior has been experimentally observed for the saturated state, where the layers magnetization are in the same direction [48, 49, 53–55]. On the other hand, the spin flop or noncollinear state has been addressed theoretically by Chiba et. al. [56], while no detailed analysis is found on the very few [47,57,58] experimental investigations found on the literature.

In an anisotropic magnetoresistance (AMR) effect, the electrical resistance depends on a relative angle between the magnetization direction and the electric current direction. It has been studied extensively both experimentally and theoretically. A voltage signal generated in FM/NM and FM/SAF may contain the contribution from anisotropic magnetoresistance (a DC voltage is generated because of nonlinear coupling between an oscillating current and an oscillating resistance, this effect is known as spin rectification effect (SRE).

The inverse spin Hall effect [59–63] is a remarkable phenomenon that turns so-called spin current into an electric current. and it has many technical applications. The inverse spin Hall effect (ISHE) is induced by spin pumping, generated by the precession of ferromagnetic resonance magnetization in an interface of a FM/NM. ISHE is commonly used to study the spin orbit interactions in non-magnetic (NM) heavy metals in contact with a ferromagnet (FM) using FM/NM bilayers. In the experiments, in most cases, the ISHE signal is mixed with spin rectification effect (SRE) signal, because the SRE cannot be neglected in the transmission line (CPW or short circuit microstrip), and it may contribute voltages with the same line shape as the ISHE [64–67]. Then, it is necessary to extract the ISHE signal from the mixed signal.

In this work, we study the anisotropies, damping and linewidth of a symmetric NiFe/Ru/NiFe synthetic antiferromagnet using broadband ferromagnetic resonance. We measure field and frequency linewidth for both, acoustic and optical modes, all along the dispersion relations. We first analyzed the acoustic mode. For a symmetric SAF, as it is our case, we do not expect any linewidth enhancement due to interlayer spin pumping, as both spin currents compensate each other [51, 68]. The sole addition of the ΔH_0 (inhomogeneous linewidth, not predicted by LLG equation) to the results from our LLG model ends in an excellent agreement with the experimental data not only for the saturated state but also for the spin flop state. This agreement with the LLG theory indicates that in fact, the interlayer spin current interactions do not produce any significant damping enhancement in neither saturated nor spin flop states. As our ΔH vs. f relationship in the spin flop region is almost linear. In the case of the optical mode, we observed a disagreement between the LLG model and the experimental results. For this mode, the LLG model shows that Δf is smaller when compared to the acoustic mode and decreases with H in the spin flop region. While experimental Δf is larger for the optical mode and increases with field. We correlate these linewidth enhancements to the optical mode out-of-phase oscillations, where the interlayer spins currents do not compensate each other.

Furthermore, we studied the spin current to charge current conversion in NiFe based bilayers and SAF systems. For this end, we have measured the generated DC voltage in the samples due to spin currents exited by broadband ferromagnetic resonance. We have studied the DC voltage

signal generated by inverse spin hall effect in NM/FM and FM/NM. Spin to charge conversion in NiFe based systems is also studied, in which, we reinforce the fact that the DC voltage signal we observe in or experiments is dominated by the NiFe signal. Finally, we presented and discussed the measured DC voltages in SAF systems, in all their magnetic states. we have studied the spin rectification and ISHE signal in FM/NM, NM/FM and SAF/NM by means of broadband FMR. Due to our extended research, we are able to differentiate the V_{DC} due to ISHE and SRE .

This thesis is structured as follows. Chapter 1 shows the motivation and the literature review on the topics studied by this work. In Chapter 2 a detailed theoretical concepts relevant to this thesis are presented including magnetization dynamics and spin rectification effects. Chapter 3 presents the experimental techniques that were used to produce and characterize the samples.

The main results are presented in chapters 4 and 5. Chapter 4 is devoted to the study of magnetic damping on synthetic antiferromagnets, while on chapter 5 the spin rectification effects on these systems is analyzed. Finaly the conclusion and future prespectives are shown in chapter 6.

2 Theoretical background

In this chapter, detailed theoretical concepts relevant to this thesis are presented. The concept of magnetization and its relationship to angular momentum is given in first section. In the following section, the different energetic contributions to the free energy of a ferromagnetic system are presented. Subsequently, the Landau-Lifshitz-Gilbert equation, which describes the magnetization dynamics of ferromagnetic systems, is discussed. In later section, spin pumping and inverse spin hall effect is included. Finally at the end, spin rectification efects in ferromagnets and anisotropic magnetoresistance is presented.

2.1 Magnetic materials

Magnetic materials can be represented as a set of magnetic moments [69] or spins that interact with each other and / or with an external magnetic field $\vec{H}$. The type of interaction of these spins, between them or with the external field, leads to different types of the magnetism such as: diamagnetism, paramagnetism, ferromagnetism and anti-ferromagnetism, etc.

From a microscopic point of view, a magnetic material is constituted by a set of spins $\vec{S}_i$ at the $\vec{r}_i$ positions within the material. These spins generate a effective magnetic moment that can be described in terms of a vector field called magnetization $\vec{M}_{(\vec{r})}$ which completely characterizes the magnetic state of the material and represents the magnetic moment density per unit of volume within the material. Local magnetization is related to the spin $\vec{S}$ at the

position of the magnetic ion $\vec{r}$ by the following expression [70]:

$$\vec{M}_{(\vec{r})} = g\mu_B \frac{\vec{S}_{(\vec{r})}}{\vec{\Omega}_{(\vec{r})}} \tag{2.1}$$

where g is the Landé factor,($\mu_B = \frac{e\hbar}{2m_e}$) is the Bohr magneton and $\vec{\Omega}_{\vec{(r)}}$ is the atomic volume per magnetic ion. This expression can be rewritten in terms of the gyromagnetic factor $\gamma = g\mu_B$ which relates the magnetization to the angular momentum per unit volume $\frac{\vec{L}}{V}$.

$$\vec{M}_{(\vec{r})} = \gamma \frac{\vec{L}}{V} \tag{2.2}$$

In ferromagnetic materials (FM) the spins interacts through the exchange energy and they align parallel to each other. In this case the intensity of the local magnetization $\vec{M}$is always the saturation magnetization $\vec{M}_S$ characteristic of the material. The magnetization then can be described only by its direction, given by the vector field $\vec{m}$ with $\|\vec{m}\| = 1$

$$\vec{M}_{(\vec{r})} = \vec{M}_s \vec{m}_{(\vec{r})} \tag{2.3}$$

2.2 Magnetic free energy

The behavior of a ferromagnetic sample as a function of the magnetic field can be explained by analyzing its free energy [69–71]. This free energy can be expressed as the sum of the energy contributions dependent on magnetization. The contributions of interest to this work are: the exchange energy, anisotropy interactions and magnetostatic energy. When the system is composed of more than one magnetic element, it also has interaction energies among them we have the exchange energy by contact between a FM and an antiferromagnet (AFM); and the coupling energy between two FMs which can be by Ruderman-Kittel-Kasuya-Yosida (RKKY) interaction, dipolar coupling or direct contact exchange interaction.

In the following subsections, the different energy terms that contribute to free magnetic energy will be described.

2.2.1 Exchange energy

The exchange energy is the product of a quantum effect of the electrostatic interaction between two electrons. In the interaction between neighboring atoms, this interaction tends to guide the electronic spin in a parallel or antiparallel way. In the quantum calculation of the energy involved there is a certain integral of energy J whose algebraic sign describes the orientation of the spins.

$$E_{Ex} = -2\sum_{i\neq\ j} J_{ij}\vec{S}_i.\vec{S}_j \tag{2.4}$$

Where, S is the spin of the atoms in the material. This interaction has a very short-range. If only interactions between the closest neighbors are considered, then the exchange energy density can be written as [70]:

$$e_{Ex} = -2JS^2\frac{1}{\Omega}\sum_{i\neq\ j}\vec{m}_i.\vec{m}_j \tag{2.5}$$

where the sum of the dot product of the directions $\vec{m}_i$ and $\vec{m}_j$ of the magnetic moments is performed only for the first neighbors. The value of J defines the type of magnetic ordering of the material. In the case of FM materials J $>$ 0, , and the spins tend to orient themselves in a parallel way. When J $<$ 0 the material is an AFM. For isotropic materials or with cubic symmetry, the exchange energy can be expressed as a function of the continuous field of the magnetization direction $\vec{m}$ as [72]

$$e_{Ex} = A(\nabla m)^2 \tag{2.6}$$

where A is the exchange stiffness constant (of dimension erg/cm) which is, in the case of a simple cubic crystal, a function of the exchange integral J_0, of the number of atoms of a unit cell of the lattice n, of the network parameter a and the spin of the atoms of the network S.

$$A = \frac{nj_0S^2}{a} \tag{2.7}$$

2.2.2 Anisotropy energies

The free energy in a magnetic material can depend on the orientation of the magnetization in relation to one axis or several preferred axes of magnetization. The energy density per unit volume e_K can be modeled using the following mathematical expression:

$$e_K = -K_1 \frac{1}{(M_s)^2}(\vec{M}.\vec{u}_1)^2 - K_2 \frac{1}{(M_s)^4}(\vec{M}.\vec{u}_2)^4 - ... \tag{2.8}$$

where the K_i values are the anisotropy constants with units of erg / cm^3, and the unit vectors u_i define the preferred magnetization axis. In polycrystalline materials, this energy is the result of different factors, among them: the magneto crystalline anisotropy of the material, the texture of the material, the possible internal stresses and the defects within the material. When anisotropy is small, the material is considered to be magnetically soft. In magnetic materials, whether soft or not, an effective anisotropy can be explicitly induced by some type of process, among them: the application of a magnetic field during production or during the thermal treatment of the material; and deposition of the material with moving substrate. This induced anisotropy can be described by an effective anisotropy, usually of a uniaxial nature and can be described by the first term of equation 2.8. In order to compare the contribution of this energy with the other energies involved in the system, it is convenient to define a uniaxial anisotropy field $H_K = 2\frac{K_1}{M_s}$. Therefore; the energy density can be expressed as:

$$e_k = -\frac{H_K}{2(M_s)^2}(\vec{m}.\vec{u}_k)^2 \tag{2.9}$$

where u_k is the unit vector that defines the direction of the anisotropy axis. In the magnetization curves (M vs. H) of a magnetic sample described only by a uniaxial anisotropy, the H_K field is equal to the coercive field or the saturation field, when the external field is applied along or perpendicular to the anisotropy axis respectively.

2.2.3 Magnetostatic energy

Magnetostatic energy originates from the interaction of the sample's magnetization with the magnetic field generated by itself, and also with the applied external magnetic field. This energy can be divided into two parts, external field energy or Zeeman energy and the demagnetization field energy. The Zeeman energy is due to the interaction between the magnetization $\vec{M}$ of the sample and the external field $\vec{H}$. The local density per unit volume of Zeeman's energy is:

$$e_{Zeeman} = -\vec{\mathrm{H}}.\vec{\mathrm{M}} \tag{2.10}$$

The demagnetization energy E_{demag} is related to the field generated by the sample magnetization itself, known as the sample demagnetizing field $\vec{H}_d$.

$$E_{demag} = \frac{1}{2}\int^{\infty} H_d^2 dV = -\frac{1}{2}\int_{sample} \vec{H}_d.\vec{M}dV \tag{2.11}$$

The problem for calculating this energy is in the calculation of the demagnetizing field itself, which depends on the sample geometry and the configuration of the magnetic domains within it. For a uniformly magnetized element, the demagnetizing energy can be calculated using the demagnetizing factors obtained from the sample geometry. These factors are η_x, η_y and η_z with $\eta_x + \eta_y + \eta_z = 4\pi$ relate the demagnetizing field to the magnetization of the sample in each of the axes $\hat{x}, \hat{y}$ and $\hat{z}$.

$$\vec{H}_d = \frac{1}{2}\left(-\eta_x(\vec{M}.\hat{x})\hat{x} - \eta_y(\vec{M}.\hat{y})\hat{y} - \eta_z(\vec{M}.\hat{z})\hat{z}\right) \tag{2.12}$$

This demagnetizing field is uniform within a magnetic element only if that element has ellipsoid geometry. But in the general case, while uniform magnetization, demagnetizing factors can be calculated for different geometries [73, 74] . In this approximation, the demagnetizing energy density per unit volume can be expressed as:

$$e_{demag} = \frac{1}{2}\left(-\eta_x(\vec{M}.\hat{x})^2 - \eta_y(\vec{M}.\hat{y})^2 - \eta_z(\vec{M}.\hat{z})^2\right) \tag{2.13}$$

2.2.4 Exchange interaction FM / AFM

The contact between a ferromagnetic material and an antiferromagnetic material leads to the coupling of its magnetizations through an exchange interaction. The main manifestation of this phenomenon is the displacement in the field of the magnetization curve (M vs. H) of samples that present this type of system, this displacement is associated with an exchange interaction field or exchange-bias field. This type of samples usually also presents a shift in frequency of the resonance frequencies as a function of the external field (f_R vs. H), an effect associated with a rotatable anisotropy field. In polycrystalline materials, these phenomena are well described by the model presented by Harres and Geshev [75]. This model considers the interaction of FM with two types of interfacial grains in AFM. These grains are classified according to their anisotropy and coupling with the FM. The resulting coupling energy for each grain can be described as:

$$E_{FM/AFM} = -J_{FM/AFM} S(\vec{m}_{FM}.\vec{m}_{AFM}) \tag{2.14}$$

where $J_{FM/AFM}$ is the coupling constant, S is the effective contact surface between the grain and the FM, and m_{AFM} is the direction of AFM magnetization in the surface layer of the grain. AFM grains with strong anisotropy are classified as stable grains, which are responsible for the exchange-bias field. In these grains, the anisotropy sets m_{AFM} in a specific direction, so the magnetization of the FM tries to orient itself in the same direction. The sum of the interaction of all stable grains from the origin to an effective unidirectional anisotropy, the related energy density term is:

$$E_{EB} = -H_{EB}\, M_s\, (\vec{m}.\ \vec{u}_{EB}) \tag{2.15}$$

here u_{EB} is the direction of unidirectional anisotropy, and H_{EB} is the effective field of this anisotropy, or exchange-bias field. For grains with low anisotropy, $\vec{m}_{AFM}$ is free to rotate following the magnetization of the FM. The angle between $\vec{m}_{AFM}$ and $\vec{m}_{FM}$ depends on the relationship between the anisotropy of the grain and the coupling with the FM, and also depends

on the magnetic history of the sample. When a grain has a very low anisotropy, $\vec{m}_{AFM}$ is oriented in the same direction as $\vec{m}_{FM}$, the collective effect of this type of grains gives rise to a rotatable anisotropy, and the associated energy density is described by:

$$e_{RA} = -H_{RA}\, M_s\, (\vec{m}.\vec{u}_{RA}) \tag{2.16}$$

with $\vec{u}_{RA} \approx \vec{m}$, and an effective anisotropy field given by H_{RA}, The effects of this type of anisotropy can be observed in measures of magnetization dynamics such as the frequency shift in the curves (f_R vs. H). For static measurements (M vs. H) the effects depend on the type of measurement. No effect is observed when the angle of $\vec{m}$ varies gradually, but when the direction of $\vec{m}$ is reversed abruptly, an increase in the field required for this inversion is observed. In this sense, the rotateable anisotropy is responsible for the increase in the coercive field in samples that exhibit the effect of exchange-bias.

2.2.5 Interaction between two ferromagnetic films

There are several mechanisms for coupling or interacting between two ferromagnetic elements. One mechanism to highlight is the dipolar interaction, mediated by the magnetic field generated by the magnetization of each element, this interaction is long-range and depends on the geometry of the elements and the spatial distribution between them. For thin films of FM materials separated by a metal spacer or not, the relevant coupling mechanisms are: Exchange interaction, when the elements are in direct contact, either on the entire surface of the elements, or due to faults ("pin-holes") in the spacer; Neel interaction, also known as Orange peel interaction, observed when the surface roughness generates magnetic charges on it, which are coupled by dipolar interaction. Ruderman-Kittel-Kasuya-Yosida (RKKY) interaction, which in the case of metallic spacers, the layers interact by itinerant magnetism mediated by the conduction electrons that pass through the spacer between the two magnetic layers. The magnetic energy density, per surface unit, related to this type of interactions, for two elements with magnetization $\vec{M}_A$ and $\vec{M}_B$, can be described by the terms of bilinear and biquadratic

coupling.

$$e_{int} = -J_1 \left(\frac{\vec{M}_A . \vec{M}_B}{M_s^A M_s^B} \right) + J_2 \left(\frac{\vec{M}_A . \vec{M}_B}{M_s^A M_s^B} \right)^2 \tag{2.17}$$

where J_1 and J_2 are the bilinear and biquadratic interaction constants respectively.

2.3 Magnetization dynamics

The magnetization dynamics of a ferromagnetic material is governed by Landau-Lifshitz-Gilbert (LLG) equation [76].

$$\frac{d\vec{M}}{dt} = -\gamma(\vec{M} \times \vec{H}_{eff}) + \frac{\alpha}{M_s} \left(\vec{M} \times \frac{d\vec{M}}{dt} \right) \tag{2.18}$$

The first term of above equation corresponds to the torque that makes the magnetization vector precesses around the effective magnetic field in an orbit as shown in figure 2.1a, with an angular frequency $\omega = \gamma H_{eff}$. Where the effective magnetic field H_{eff} is sum of all the field like contributions obtained from the energy terms. i.e.

$$H_{\text{eff}} = \boldsymbol{H_0} + \boldsymbol{h(t)} + \boldsymbol{H_{Ex}} + \boldsymbol{H_{dem}} + \boldsymbol{H_{ani}} \tag{2.19}$$

Here H_0 is the applied magnetic field, h(t) is the dynamic component of external field, H_{Ex} is the exchange field and H_{dem} represents the demagnetization field created by the dipolar interaction of magnetic surface and volume charges. The field H_{ani} includes all kinds of anisotropic fields. All these magnetic fields can be calculated as the first derivatives of the corresponding energies with respect to the magnetization vector.

$$\vec{H}_{\text{eff}} = -\frac{de_{\text{free}}}{d\vec{M}} \tag{2.20}$$

The second term in the LLG represents the damping in the magnetic systes. Due to damping the precession amplitude of the magnetization decreases with time, and the tip of the magnetization

vector follows a spiral path (see figure. 2.1b). The damping is related to the rate at which energy is lost from the precessing magnetization.

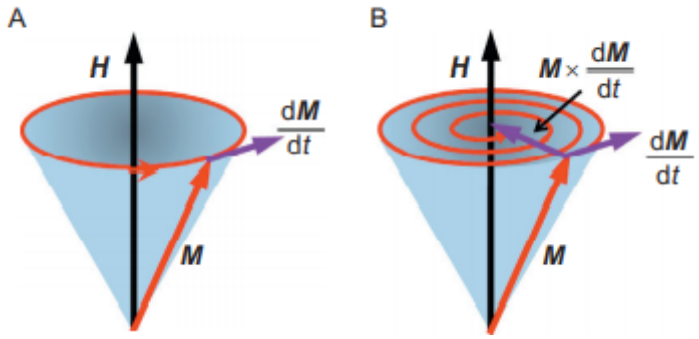

Figure 2.1: Precession of magnetization vector (M) around magnetic field (H) (A) in absence of damping term and (B) in presence of damping term. [77]

The solutions of the LLG equation show that when the magnetic system is out of balance, the magnetization vector describes a precession movement around its equilibrium position. If there is no force to keep the system out of balance, the oscillating part of the magnetization vector oscillates with the natural frequency of the system, and its amplitude decreases exponentially with a rate proportional to the damping parameter α. When the magnetization is forced to oscillate at a given frequency, for example by the action of an external radio frequency field, the amplitude of the oscillating part of the magnetization vector depends on the damping parameter, as well as the difference of the system natural frequency and the frequency of the excitation field. When these two frequencies are equal, the amplitude of oscillation is maximum, and the system is in the condition of ferromagnetic resonance (FMR). FMR can be measured by obtaing the power absortion profiles with respect to the field at a fixed frequency (Traditional FMR) or varing both, frequency and field (Broadband FMR) [78].

In terms of ferromagnetic resonance, the damping is responsible for the finite linewidth of the measured FMR power absorption profile, as shown in figure.2.2. The widths of half maximum power $\Delta\omega$ (in frequency unit) and ΔH (in magnetic field unit), which are shown in figure.2.2 (a) and 2.2(b), respectively, are the standard experimental measurements of loss in ferromagnetic materials. The damping parameter α can be extracted from the analysis of the FMR linewidths [79].

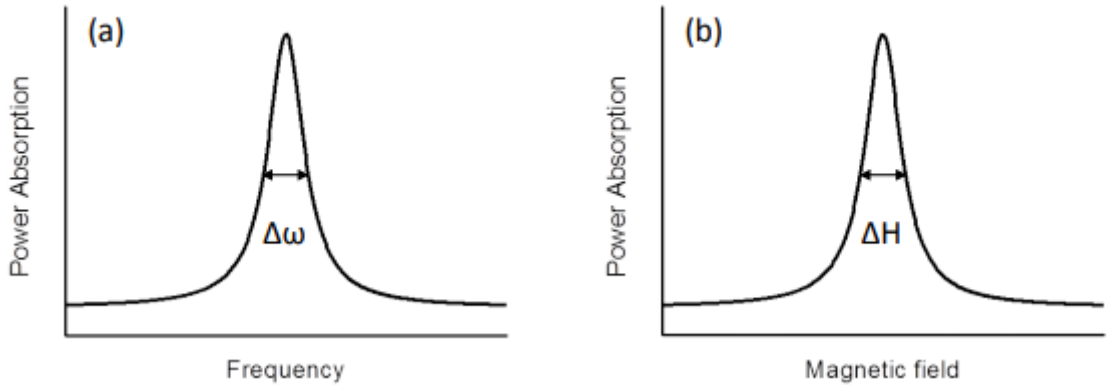

Figure 2.2: Schematics of ferromagnetic resonance (FMR) power absorption profiles. (a) FMR power absorption profile for sweeping the microwave frequency at a fixed external magnetic field. (b) FMR power absorption profile for sweeping the external magnetic field at a fixed microwave frequency [79].

In the literature we can find very important solutions to the LLG equation for simple magnetic systems [78]. The formula obtained from the Smith-Beljers approach [80] relates the resonance frequency f_R with the curvature of the free energy density (E) and the system, as a function of the polar θ and azimuthal ϕ angles of the magnetization, with equilibrium positions θ_0 and ϕ_0.

$$2\pi f_R = \omega_R = \frac{1}{\sqrt{1+\alpha^2}} \frac{\gamma}{M_s \sin\theta_0} \sqrt{\frac{\partial^2 E \partial^2 E}{\partial\theta^2 \partial\phi^2} - \left(\frac{\partial E}{\partial\theta\partial\phi}\right)^2} \tag{2.21}$$

This expression has evolved as the standard method to determine the precession frequency of the magnetization.

2.4 Spin currents and spin rectification effects

As compared to simple charge based electronics, spintronics has an extra degree of freedom, which is known as spin polarized current. There are several methods of producing spin currents in FMs and non magnetic metal (NM) e.g.:

(1) In FMs, spin currents are mostly generated by virtue of applied magnetic field or radio frequency field h_{rf}.

(2) In NM metals, spin currents can be produced from FM by pumping of spins.

Spin rectification effect is discussed in section 2.4.3.

2.4.1 Spin Pumping

We can generate a spin current by pumping the spins from a ferromagnet into an adjacent non magnetic (NM) metal structure using the magnetization precession caused by ferromagnetic resonance (FMR) [81–83]. When this effect happens, from the FM a spin current $\bar{\bar{\boldsymbol{J}}}_S$ flows into the non-magnetic layer, the spin polarization $\boldsymbol{J}_S$ carried by this spin current is given by [82]:

$$\boldsymbol{J_S} = \frac{h}{4\pi} G^{\uparrow\downarrow} \left(\boldsymbol{m} \times \frac{\boldsymbol{dm}}{\boldsymbol{dt}} \right) \tag{2.22}$$

where $G^{\uparrow\downarrow}$ is the interface spin mixing conductance, which describes efficiency of the spin transport through the interface [84].

Due to the emission of a spin current from the FM into the NM, the magnetization precession looses spin angular momentum, which gives rise to additional magnetic damping.

2.4.2 Inverse Spin Hall Effect (ISHE)

In solids spin of the electron is coupled with its momentum due to the spin-orbit interaction. This coupling gives rise to mutual conversion between charge and spin currents: the direct and inverse spin Hall effects [85]. The process in which a spin current $\bar{\bar{\boldsymbol{J}}}_S$ is converted into charge current $\boldsymbol{J_C}$ is known as Inverse Spin Hall Efect (ISHE) as shown in figure 2.3.

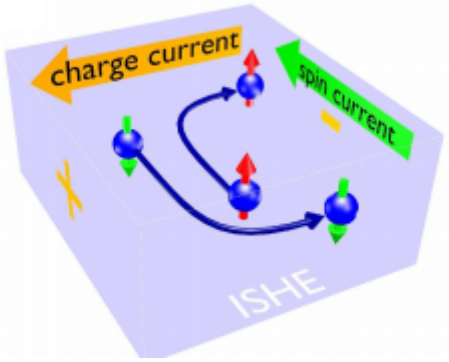

Figure 2.3: The generation of an unpolarized charge current in a normal metal perpendicular to a spin-polarized electron current. [86]

The existence of a pure spin current can be seen as the two electrons traveling in the opposite directions along the spin current flow direction and with opposite spins, as shown in figure 2.3, then in the NM metal the spin-orbit interaction bends these two electrons in the same direction and induces a charge current J_C transverse to both the spin current polarization and flow direction. Finally, J_C generated by the ISHE causes charge accumulation at the edges of the NM layer, and setup a electric potential difference between the edges. Therefore, from this method we can detect the ISHE as a DC voltage on the NM layer [83].

Mathematically the ISHE can be understood as the following: A spin current $\mathrm{J^S}$ is related to the spin polarization density P, through the spin diffusion equation [87], and can be written in tensor form as

$$\frac{\mathrm{J^S}_{ij}}{\hbar} = -D\frac{\partial P_j}{\partial x_i} \tag{2.23}$$

where the index i corresponds the direction of flow and j indicates wich component of the spin is flowing, D is the diffusion coefficient and $\hbar$ is the reduced Planck constant. In ISHE, the charge current $\mathrm{J^C}$ is related to the rotational of P and can be written as:

$$\frac{\mathrm{J^C}}{e} = \Theta_{\mathrm{SH}} D(\nabla \times P) \tag{2.24}$$

where, e is the electron charge and Θ_{SH} is the spin hall angle of the material. The components

of $\nabla \times P$ can be written in terms of the Levi-Civita tensor ϵ_{ijk} as:

$$[\nabla \times P]_i = \sum_{j,k} \epsilon_{ijk} \frac{\partial P_k}{\partial x_j} \tag{2.25}$$

then, mixing equations 2.25, 2.24 and 2.23 we obtain the relation between the charge current components $\mathrm{J^C}_i$ and the spin current components $\mathrm{J^S}_{jk}$

$$\mathrm{J^C}_i = -e\Theta_{\mathrm{SH}} \sum_{j,k} \epsilon_{ijk} \frac{\partial P_k}{\partial x_j} = -\frac{e}{\hbar}\Theta_{\mathrm{SH}} \sum_{j,k} \epsilon_{ijk} \mathrm{J^S}_{jk} \tag{2.26}$$

the term $\epsilon_{ijk}\mathrm{J^S}_{jk}$ can be understood as the cross product $\epsilon_{ijk}\hat{n}_j\vec{\sigma}_k = [\hat{n} \times \vec{\sigma}]_i$ between the unit vector $\hat{n}$ that indicates the flow direction of $\mathrm{J^S}$ and the vector $\vec{\sigma}$ that correspond to the spin orientation and amplitude of $\mathrm{J^S}$. Thus, the charge current vector $\mathrm{J^C}$ can be expressed as

$$\mathrm{J^C} = -\frac{e}{\hbar}\Theta_{\mathrm{SH}}(\hat{n} \times \vec{\sigma}) \tag{2.27}$$

.

2.4.3 Spin rectification effects in ferromagnets

By the rectification effect of high frequency magnetization dynamics dc currents and dc voltages can be generated, which are known as spin rectification current and spin rectification voltage. [88–92].

Under the application of resonance field h_{rf} magnetization start precessing around the static field H and this precession will produce an dynamic resistance $R_{(H_{(t)})}$. Spin rectification (SR) is the production of a dc voltage V_{DC} in a ferromagnetic structure due to the nonlinear coupling between a dynamic resistance $R_{(H_{(t)})}$ and a dynamic current $I_{(t)}$. As a consequence, a nonzero time averaged voltage can be measured along the current direction.

$$V_{\mathrm{DC}} =< \mathrm{Re}[R_{(H_{(t)})}]\mathrm{Re}[I_{(t)}] > \tag{2.28}$$

So, we can summarize that for spin rectification following three conditions must be satisfied: (1) Presence of magnetoresistance effect (2) A torque which drives the magnetization, resulting in a time varying magnetoresistance (3) An rf current which can couple to the resistance and produce a dc voltage. These conditions are shown in figure 2.4

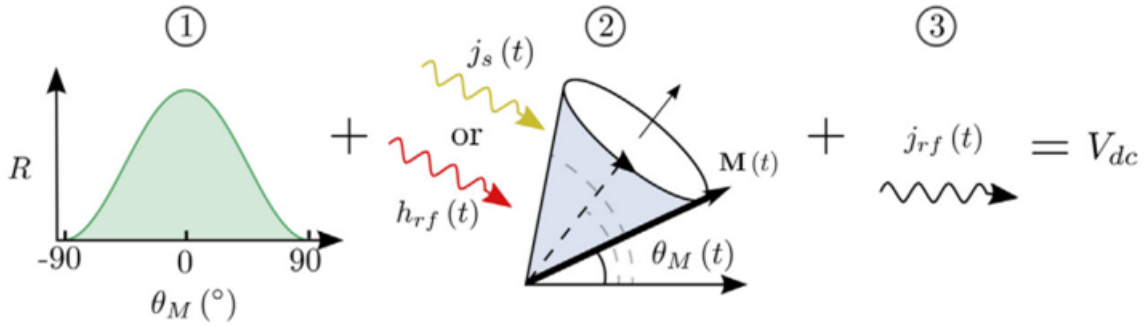

Figure 2.4: Three conditions of spin rectification effect. [93]

In this figure, we can see that the precessing magnetization is producing rf resistance. Furthermore, magnetization is precessing by field torque or from spin torque, produced by h_{rf} and spin current j_s respectively. The rf resistance can then couple nonlinearly to an rf current and produce a rectified voltage V_{dc}. The well known magneto resistance are: anisotropic magnetoresistance (AMR) and giant magnetoresistance (GMR) etc.

2.4.4 Anisotropic magnetoresistance

The magnetoresistance which dependence on the relative angle between the direction of the current and the magnetization is known as anisotropic magnetoresistance. The anisotropic magneto resistance effect is shown in figure 2.5:

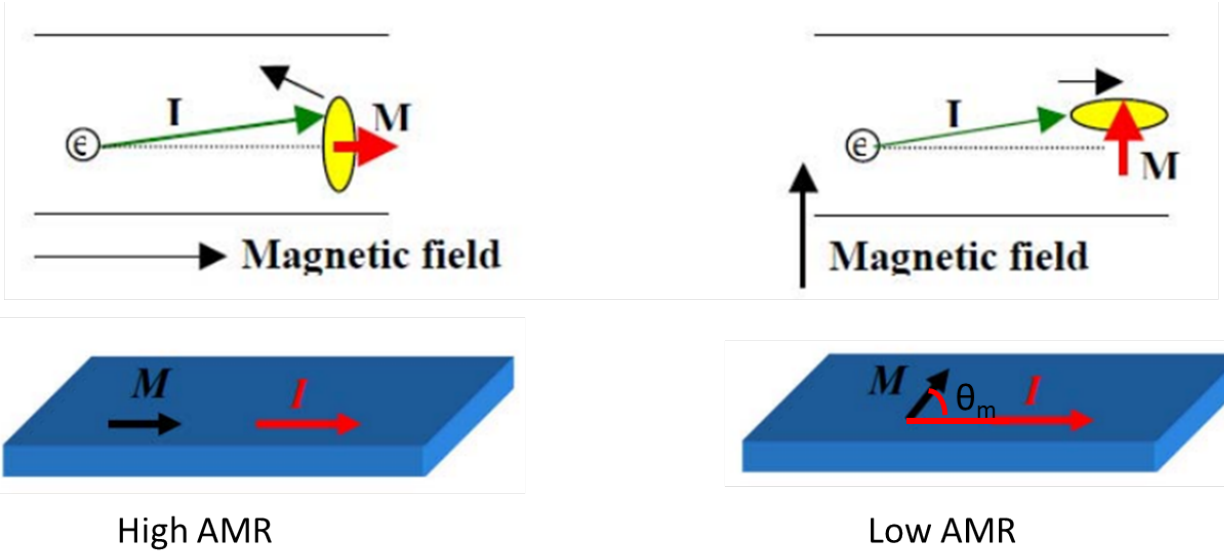

Figure 2.5: Anisotropic magnetoresistance, Left panel: direction of magnetic field, magnetization and current are held perpendicular to electronic orbit (yellow color), Right panel: direction of magnetic field, magnetization and current are held parallel to electronic orbit

In this figure (left panel), electronic orbital is shown in yellow color, which is oriented perpendicular to current direction (red color) , thus increasing the scattering cross section, therefore, AMR will be increased. In right panel of figure, we can see that electronic orbital is oriental parallel to current direction, decreasing the scattering cross section, the system will have low AMR.

The physical origin of AMR is spin-dependent scattering in ferromagnetic metals due to their band structure and the spin–orbit interaction [94,95], also it is highly angular dependent, mathematically :

$$\rho(\theta_m) = \rho_\perp + (\rho_\parallel - \rho_\perp)\cos^2(\theta_m) \tag{2.29}$$

where, θ_M is the angle between the current and the magnetization direction, while $\rho_\parallel$ and $\rho_\perp$ are the resistivities, when current and the orientation of magnetization are parallel and perpendicular, respectively.

AMR produces a rectification effect (already explained in 2.4.3).

2.4.5 Giant magnetoresistance (GMR)

The phenomenon of GMR was discovered by Baibich et al. in 1988 [1] and its orign lies in the spin dependent scattering of electrons under the action of applied magnetic field. Moreover, it is associated with spin valve structures (FM/NM/FM) . GMR of magnetic system, changes with the relative magnetization orientation of the ferromagnetic layers and it is maximum when the orientation of magnetization is antiparallel in both FMs and is minimum when orientation of magnetization is parallel, mathematically it is written as (2.30):

$$GMR = \frac{R_{AP} - R_P}{R_P}\% \tag{2.30}$$

where R_{AP} and R_{AP} represents resistance in antiparallel and parallel state respectively.

3 Experimental Techniques

This chapter presents the experimental techniques that were used to produce and characterize the samples, analyzed in this work. In section 3.1 I will discuss all about sample fabrication techniques while in section 3.2, I will discuss sample characterization techniques in detail.

3.1 Sample Preparation Techniques

3.1.1 Magnetron sputtering

Deposition of films was carried out with magnetron sputtering technique, as shown in the figure 3.1.

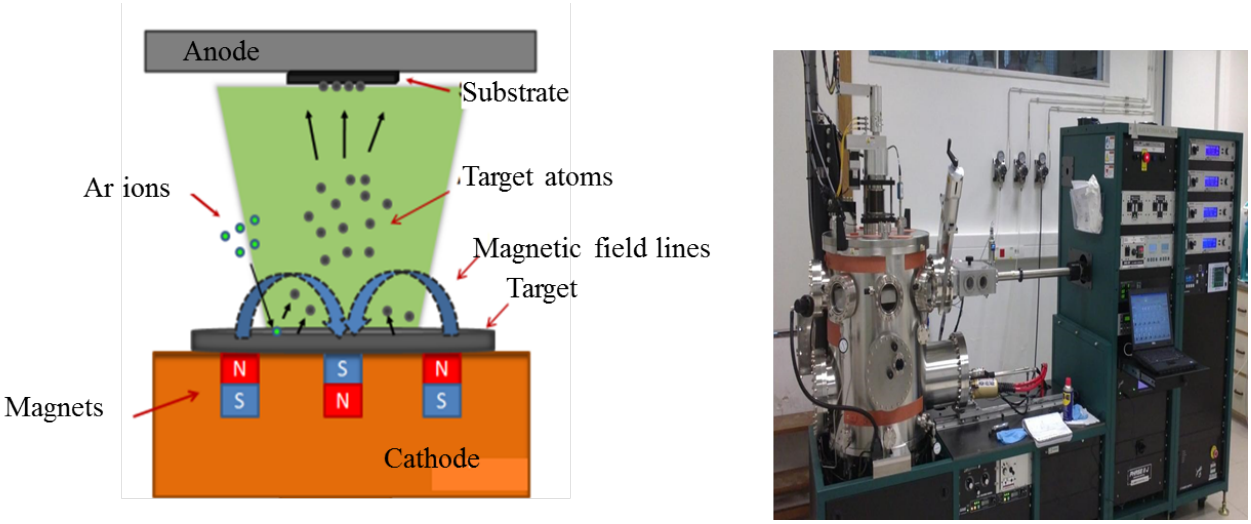

Figure 3.1: Left: Physical Process of sputtering, Right: Magnetron sputtering deposition system in CBPF.

Sputtering is based on the momentum transfer process and this process consists of ionizing

a gas between two electrodes, generating an ion plasma. These ions are then accelerated by a electric field towards the target where, when collide, they are able to eject the atoms from the target that will finally be deposited on the surface of a substrate placed in the vicinity. Free electrons are trapped in the presence of magnetic field increasing the ionization rate, thus more ions are available to hit the target. The sputtering process can be seen at left side of the figure 3.1. This is a basic technique for the production of single layers and multilayers samples, which are studied in this work. Most deposition processes of magnetic layers, oxide layers, metallic non-magnetic layers, have been realized in the AJA sputtering machine , that is part of the equipment of the multi-user laboratory LABSURF/LABNANO/CBPF, that can be seen at right side of the figure 3.1. This system has capacity of six targets installed at the same time.The targets are connected to DC and RF sources to power the plasma. In general , the RF-powered discharge operates in the same way as the dc-powered. In both cases, a voltage is applied between the cathode and the anode, a breakdown occurs and plasma is formed and sustained.RF power, though, allows the use of insulating materials as sputtering targets, and it increases the level of ionization in the plasma.

The main vacuum pump is a turbo pump that allows a pressure down to 10^{-8} Torr in the main chamber of the system.A secondary load-lock chamber allows the exchange of samples without breaking the vacuum in the main chamber.

The samples are placed in a rotating turret that allows you to take them to the position of each target and control the distance between the target and the substrate. A shutter over the target allows the control of exposure on the substrate and the precise control of the deposition time via software. Different substrate holders allow the application of a magnetic field over the substrates during deposition.

The entire system is automated and controlled by a computer, allowing automated production of multilayers and other complex structures. The deposition times of each layer, the pressure of argon gas during deposition, and the powers of the DC and RF sources can be automated.

3.1.2 Calibration of deposition rates

The deposition rates were calibrated with X-ray reflectometry (XRR), which is an analytical technique for investigating thin layered structures, surfaces and interfaces using the effect of total external reflection of X-rays. Reflectometry is used to characterize single and multi-layer structures and coatings in magnetic, semiconducting and metals among others. X-Ray Diffraction (XRD) is a basic technique for the structural characterization of deposited films. It allows the calibration of the deposition rate, film thickness and roughness by low angle diffraction. XRD measurements were performed in the crystallography and Xray laboratory using a Panalytical X Pert PRO (Philips, Panalytical) diffractometer. The source of this diffractometer emits $Cu - K_\alpha$ radiation with a waveform of 1.54045 $A°$. The film thickness is calculated by analyzing the Bragg interference peaks obtained experimentally. For each peak found at angle θ_n , the scattering vector q_n is found given by:

$$q_n = \frac{4\pi \sin \theta_n}{\lambda} \tag{3.1}$$

The linear fitting of (q = an + b) of these values vs. the peak number found n the thickness is obtained $t = 2\pi/a$ that of the measured film. When dividing this thickness between the deposition time is found to deposition rate (τ) .

$$\tau = \frac{\text{Thickness}}{\text{Deposition Time}} \tag{3.2}$$

The X-ray spectrum at grazing angles for Ni81Fe19 thin film deposited on Si (100) is shown in figure 3.2.(adopted from [96]), along with the graph of the scattering vector q vs. index n and the linear fitting ($q = an + b$) of each measured value [97].

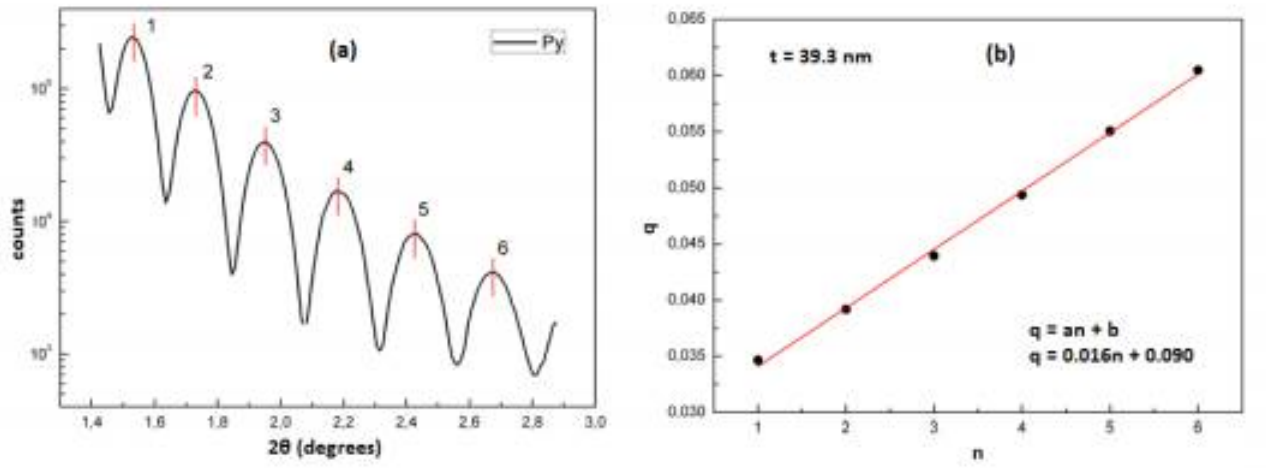

Figure 3.2: (a) X-ray spectra at grazing angles of a Ni81Fe19 film. (b) Shows the linear fitting (q = an + b) of each measured value. The black dots indicate the n indices and the red line is the linear fitting .

The deposition rates and deposition parameters are shown in table 3.1.

Target	Sputtering Source	Current(DC)/ Power(Rf)	Deposition Rate (A/s)
IrMn	DC	200 mA	4.25
CoFe	DC	200 mA	2.15
Ru	DC	100 mA	0.570
NiFe	DC	100 mA	0.970
CoFeB	DC	100 mA	0.626
Al_2O_3	RF	75 W	0.155
Al	DC	150 mA	1.283
Ta	DC	150 mA	1.995
Cu	DC	150 mA	3.940

Table 3.1: Deposition rates, calculated by XRR, for various sputtering targets.

3.2 Sample Characterization Techniques

3.2.1 Alternative Gradient Field Magnetometer (AGFM)

The Alternating Gradient Field Magnetometer is used to obtain the magnetization curves and it works on the principle of the vibration of a magnetic sample due to the force resulting from the interaction between its magnetic moment and an alternating magnetic field gradient applied on it. In addition to the field gradient, a static field is applied through a Helmholtz coil. The amplitude of vibration is amplified when the frequency of the field gradient approaches the resonance frequency of the rod that holds the sample. This vibration is transduced to a signal, using a piezoelectric sensor, which is subsequently measured by a Lock-In amplifier, and this signal is proportional to the magnetic moment of the sample in the direction of the static field. This system has a sensitivity of 10^{-7} emu, sufficient for measurements of the sample studied in this project. The schematic presentation of the AGFM is shown in figure 3.3

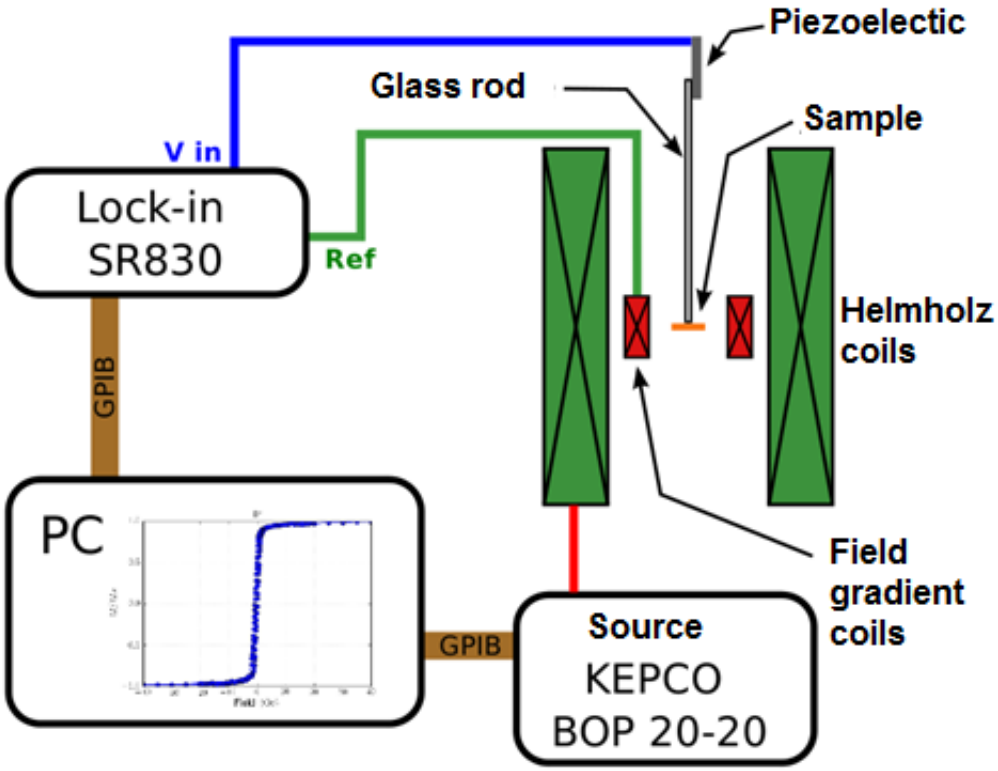

Figure 3.3: The experimental setup of AGFM.

3.2.2 Vibrating sample magnetometer (VSM)

The vibrating sample magnetometer is a magnetometer whose operation principle is based on Faraday's law of induction (a variable magnetic flux induces an electromotive force in a closely located conductor). The sample is attached to the end of a rod that vibrates with constant amplitude at a certain frequency. A VSM operates by first placing the sample to be studied in a constant magnetic field. If the sample is magnetic, this constant magnetic field will magnetize the sample by aligning the magnetic domains, or the individual magnetic spins, with the field. The stronger the constant field, the larger the magnetization will be. The magnetic dipole moment of the sample will create a magnetic field around the sample, sometimes called the magnetic stray field. As the sample is moved up and down, this magnetic stray field is changing as a function of time and can be sensed by a set of pick-up coils. The alternating magnetic field will cause an electric field in the pick-up coils according to Faraday's Law of Induction. This current will be proportional to the magnetization of the sample. The greater the magnetization, the greater the induced current. Our PPMS dynacool system for measuring the M x H response is shown in 3.4

Figure 3.4: PPMS dynacool in CBPF

3.2.3 Broadband Ferromagnetic Resonance

Conventional ferromagnetic resonance is one of the best established techniques for measuring spin waves in magnetic systems. In this technique, a electromagnetic wave with constant frequency is applied over the magnetic system, by means of a resonant cavity. By varying the external magnetic field, the system can be carried to the ferromagnetic resonance condition. When measuring the absorption of the electromagnetic wave within the cavity, the resonance field is obtained when the absorption is maximum. A broadband ferromagnetic resonance system is a system that, in contrast to the conventional FMR technique, allows us to explore the dynamic response of a magnetic system by varying both the frequency of the excitation wave and the applied magnetic field. In this system the resonant cavity is replaced by a broadband waveguide connected to a vector network analyzer (VNA), allowing measurements over a wide range frequencies ranging from a few MHz to several GHz. The power absorption in the magnetic system is obtained form the electrical properties (S parameters) of the waveguide . The VNA can measure beyond the total absorption in the waveguide, both the real part and the imaginary part of the response of the system.

$$P_{Absorbed} = P_{Incident}\left[1 - |S_{21}|^2 - |S_{11}|^2\right] \tag{3.3}$$

Where, S_{11} and S_{21} are the reflection and transmission coefficients.

The typical setup of our VNA-FMR system is show in figure 3.5. Our system is able to measure not only the broadband power absorption spectra but also the absorbed power derivative with respect to the external field (dP/dH) for a broadband frequency range around a fixed field (see left panel of figure 3.5c), and dP/dH for a fixed frequency and variable field (see right panel of figure 3.5c). In both dP/dH measurements, at fixed frequency or fixed field, dP/dH is calculated numerically from the absorption measurements around a set field H_0,

$$\frac{dP}{dH}_{(H_0)} = \frac{P(H_0 + \delta H) - P(H_0 - \delta H)}{2\delta H} \tag{3.4}$$

where δH is a small DC field applied using the same solenoid or Helmholtz coil used to apply

the H_0 field. In the fixed frequency sweep we can measure the field linewidth ΔH, while on the fixed field case we obtain the frequency linewidth Δf

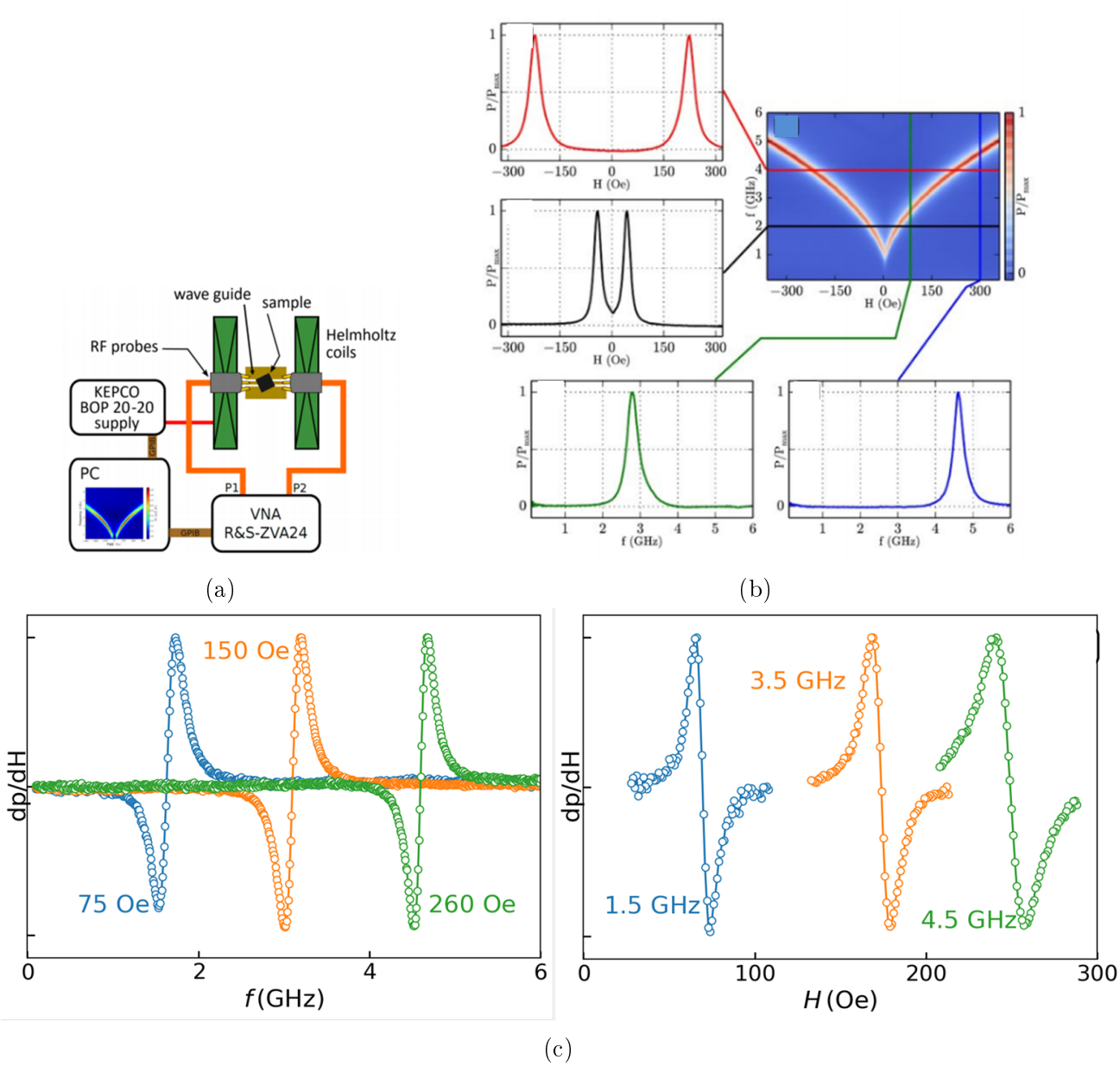

Figure 3.5: (a) Scheme of a Broadband-FMR spectrometer (b) An example of a broadband FMR spectrum. (c) L, dP/dH as function of frequency measured at a fixed field, R dP/dH as function of field measured at a fixed frequency.

Dispersion relations and effective damping

In order to obtain the values of resonance field H_R or resonance frequency f_R and their respective linewidths form the measured dP/dH curves we fit them using the following equation [98]:

$$\frac{dP}{dH} = K_1 \frac{2(X - X_R)}{\Delta X^2 + (X - X_R^2)^2} + K_2 \frac{\Delta X^2 - (X - X_R)^2}{\Delta X^2 + (X - X_R^2)^2} \tag{3.5}$$

where K_1 and K_2 are the amplitudes of the asymmetric and symmetric parts of the equation, and X can be replaced with field H or frequency f. Thus we can obtain, as fitting parameters, the resonance field H_R and field linewidth ΔH for fixed frequency measurements or the resonance frequency f_R and frequency linewidth Δf for fixed field measurements. The dispersion relation is obtained from the correspondences of resonant frequency to measurement field ($\mathrm{f_R}$) vs. H) or resonant field to measurement frequency (H_R) vs. f).

Once we have obtained the field linewidths ΔH the damping parameter α can be obtained by fitting ΔH as function of frequency f to:

$$\Delta H_{\mathrm{Measured}} = \alpha \frac{4\pi}{\gamma} \mathrm{f} + \Delta H_0 \tag{3.6}$$

here the line width at zero frequency ΔH_0 is attributed to the inhomogeneous widening of the FMR line. To obtain α from the measured frequency linewidths Δf one must first transform them to field linewidths ΔH:

$$\Delta H = \left(\frac{d\mathrm{f}_R}{dH} \right)^{-1} \Delta \mathrm{f} = \alpha \frac{4\pi}{\gamma} \mathrm{f}_R + \Delta H_0 \tag{3.7}$$

where $\mathrm{df_R/dH}$ is the derivative of the dispersion relation.

The result obtained from the measurement of a 100 nm NiFe film is shown in figure 3.6. (P_{abs}) vs. H vs. f is displayed using a color map [figure 3.6 (a)] where the color of each point in space H vs. f represents the intensity of (P_{abs}) in the respective fields and frequencies, the blue colors represent low or no absorption, while the red color indicates high absorption which occur

in FMR condition. In the color map presented, two branches can be clearly seen, which vary in position in the field and frequency, follow the dispersion relation (f_R Vs H) of the sample.

In the color map cross sections are made at a fixed frequency, in these sections it is possible to observe the amplitude and resonance peaks as a function of the external field [figure 3.6 (b) and (c)]. It is also possible to carry out cross sections for a fixed field [figure 3.6 (d) and (e)]. In these graphs, resonance peaks are also observed where the maximum amplitude of the peak occurs at a certain frequency of resonance f_R.

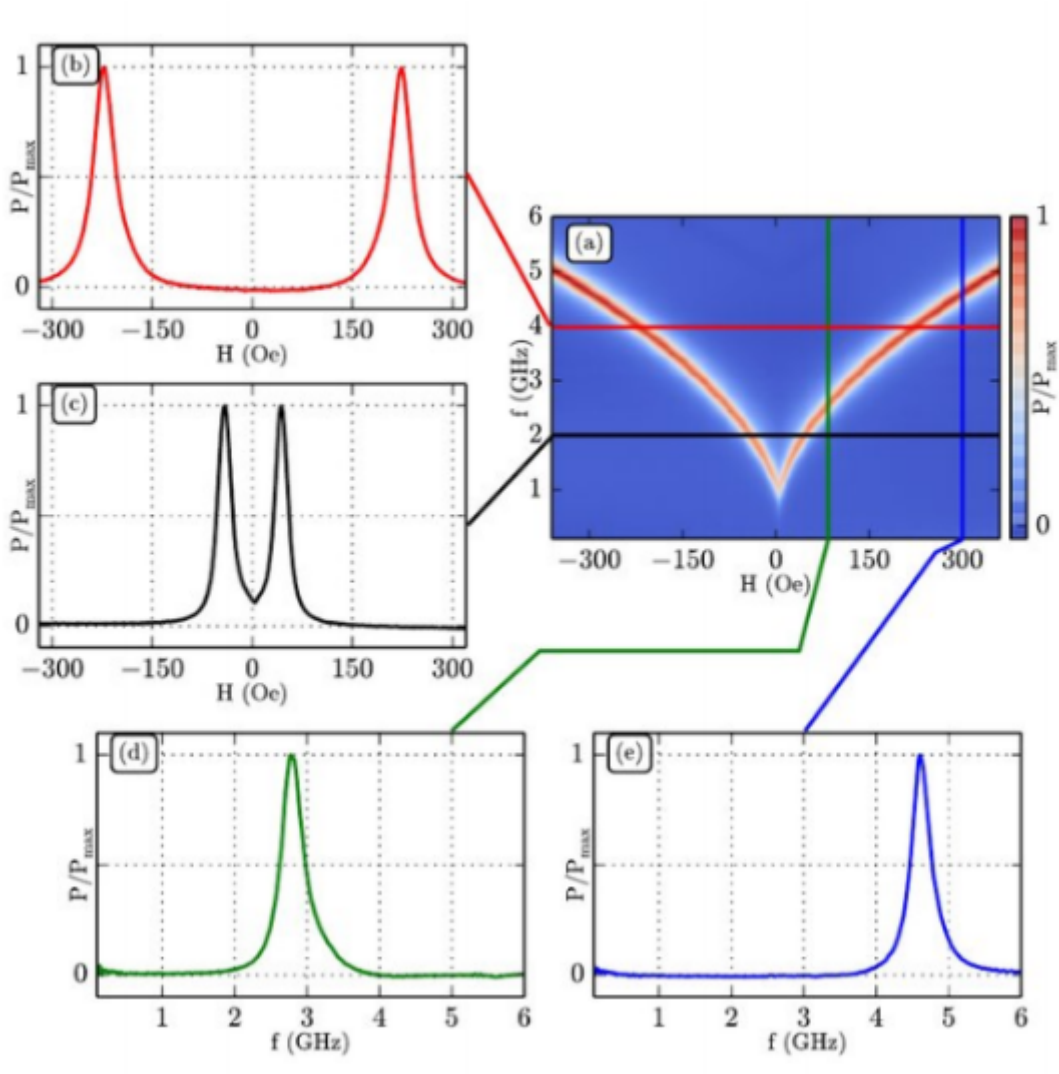

Figure 3.6: Resonance measurements for a sample composed of Ta (5 nm) / NiFe (100 nm) / Ta (5nm). (a) Color map depicting the broadband resonance spectrum. (b) and (c) Absorption profiles at 4 GHz and 2 GHz frequencies, respectively. (d) and (e) Absorption profiles in the fields of 100 Oe and 300 Oe respectively.

3.3 Spin rectification voltage measurements

The experimental setup for measuring spin rectification voltage is shown in figure 3.7

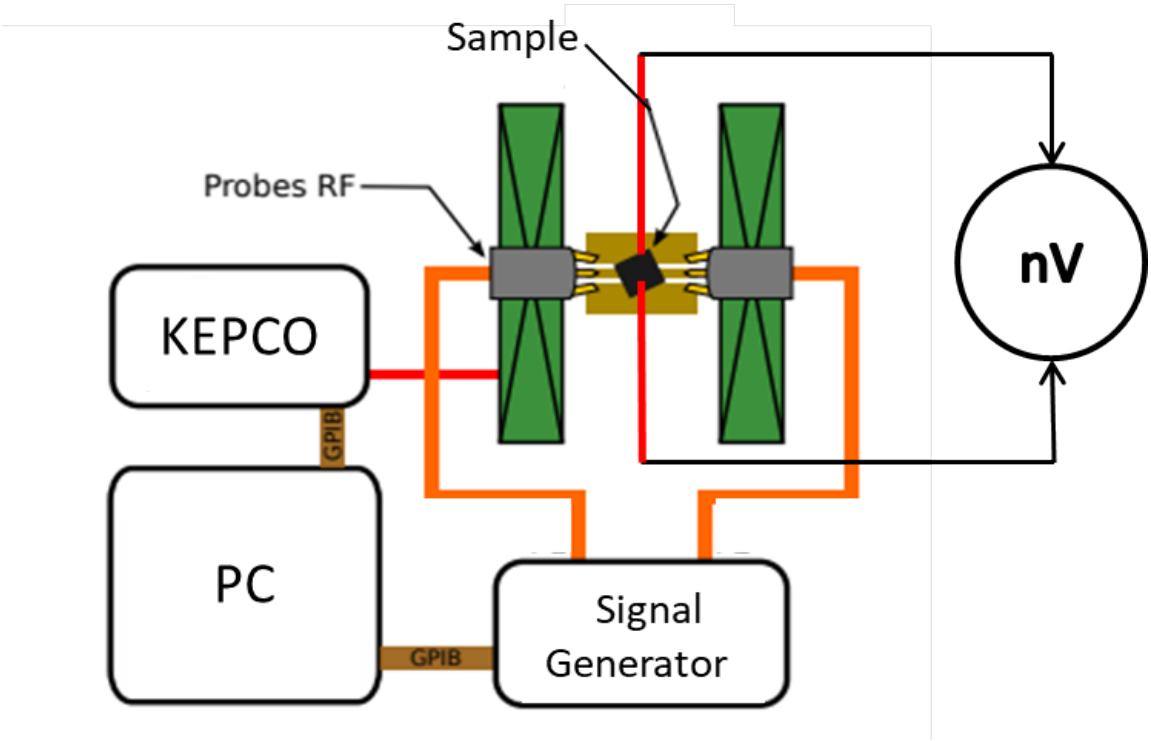

Figure 3.7: Experimental setup for measuring V_{DC}

The sample (FM/NM, NM/FM or SAF/NM) is placed on a short circuit microstrip waveguide. The Helmholtz coils are connected to KEPCO power supply, by Helmholtz coils we generate a static field H of 350 Oe applied to align the magnetization of sample along the field H. For excitation, a rf field h_{rf} is applied through a signal generator (Rohde and Schwardz, with broadband frequency range 1 GHz to 22 GHz). Furthermore, for V_{DC} measurements, a nano voltmeter (Keysight 34420A) is connected to a sample using DC probes. The measured voltage signal (spin rectification or ISHE) as a function of applied magnetic field in NM by using nano voltmeter is shown in figure 3.8.

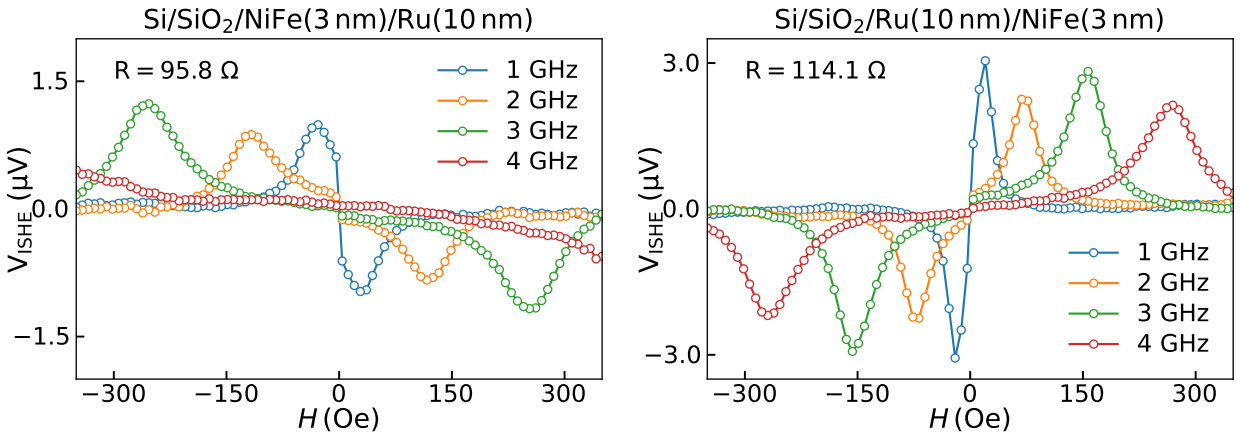

Figure 3.8: V_{ISHE} vs H response, over fixed frequencies for the samples, presented in figure 5.1.

Voltages signal are shown at different broadband frequencies. The peak value of voltage signal is presenting the resonant modes over the dispersion relation of sample, while the overall amplitude signal is due to NiFe and Ru layers.

4 Intrinsic and spin pumping damping in synthetic antiferromagnets

In this chapter we will extensively study, synthetic antiferromagnet systems, their fabrication method, static and dynamic, magnetization. In the first section and its subsections, we will discuss basic concept about SAFs. The purpose of study and their applications are also included in this section. In the second section, we will provide samples details and fabrication techniques. Third section and its subsection will be about static magnetization experimental results of all our samples. In the fourth section, we will discuss our macrospin model. Fifth section will be about dynamic magnetic characterization including broadband FMR, calculation of magnetic anisotropies and comparing them with macrospin model results. The sixth section and its subsections, will be about linewidth and damping calculations, including absorbed power derivative. In the 7th section, we will disscuss all the results. Lastly, we will conclude the chapter in the 8th section.

4.1 Introduction

A SAF consists of two magnetic layers, coupled through a thin metallic layer via the Ruderman - Kittel- Kasuya - Yosida (RKKY) interaction [19,20]. The coupling between ferromagnets can be ferromagnetic (when orientation of magnetization in both magnetic layers are parallel) or anti ferromagnetic (when orientation of magnetization in both magnetic layers are antiparallel magnetic layers are antiparallel), and it depends on the sign of coupling constant J as

mentioned in equation 2.5 in chapter 2. It is reiterated that the equation 2.5 clearly indicates that for negative value of J SAF has antiferromagnetic coupling between both magnetic layers and for positive values of J it has ferromagnetic coupling. This dependence is shown in figure 4.1 In this figure a stack of two ferromagnets(FM) separated by a non magnetic (NM)

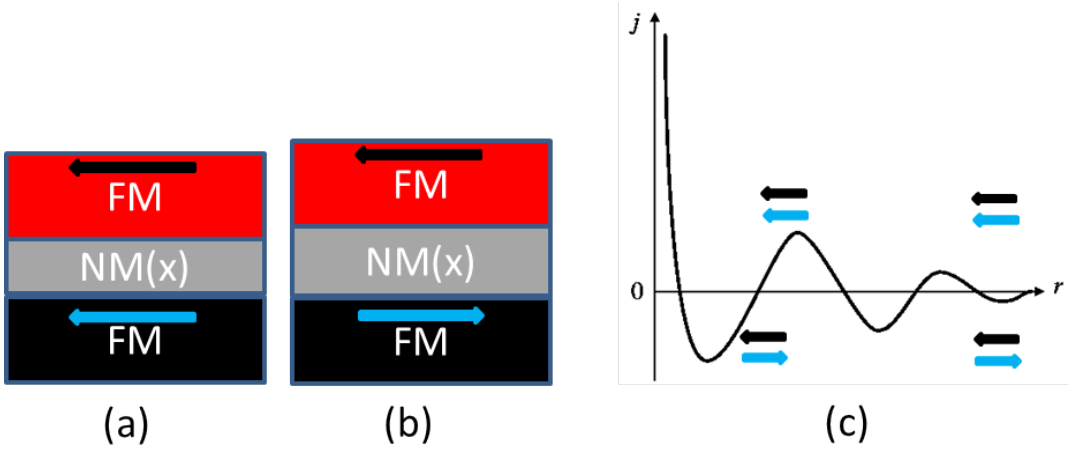

Figure 4.1: In SAF(a) Ferromagnetic coupling, (b) Antiferromagnetic coupling and (c) Relationship between coupling constant J and the separation distance r between two ferromagnetic layers.

spacer (Ru) is presented. The direction of magnetization is indicated by arrows. Figure 4.1 (a) presents ferromagnetic coupling between the two magnetic layers , figure 4.1 (b) presents the antiferromagnetic coupling, while 4.1(c) shows the relationship of the exchange coupling constant J with respect to the thickness of the spacer. The interaction between the ferromagnets is of oscillatory kind, and it dies out when the separation distance becomes large.

SAF systems are important constituents of complex layered structures used in magnetic sensors, magnetic random access memories, nano-oscillators, and other spintronic devices. Thermal stability is a important feature of SAF, [28–34, 99, 100] which reduces the thermal fluctuations and the probability of a spontaneous switching. Moreover, SAF structure has gained more attention since it enhanced the output power of STOs (spin torque oscillators) and for the possibility to show two excitations modes (1-10GHz) at zero applied field [101]. Also, the magnetic orientations of the SAF can be manipulated, providing an important magnetic versatility. So, in order to optimize and design futures spintronic devices, the understanding, of the mechanism

of the magnetization dynamics i.e. the excitations modes in the SAF, in the different magnetic configurations, is required. In all these applications, the magnetic damping is an important issue, defining the performance and general behavior. To analyze damping it is important to take into account the magnetization states, where the relative angle between the magnetizations defines three magnetic regions: saturation, spin-flop and antiparallel. [45–47].

To understand the SAF structures, we must study their static and dynamics properties. Different methods have been implemented in the past in order to study the excitations modes or ferromagnetic resonance (FMR) in thin films. In this work, the broadband ferromagnetic resonance, based on a network analyzer (VNA-FMR), is used to study the high frequency magnetic response of a SAF. In broadband FMR, an external rf magnetic field (h_{rf}) is responsible for inducing the excitation in the range of few MHz to dozens of GHz. The relative orientation between the h_{rf} and the sample magnetization (M) will define which fundamental resonant mode is excited. Concerning the magnetization dynamics, it is also important to analyze the two observed ferromagnetic resonance modes: an in-phase precession (acoustical mode) and out-of-phase precession (optical mode) [35,36].

It is well established that FMR in SAF systems produces spin currents through the non-magnetic spacer, resulting in spin pumping and spin transfer torque effects. Spin pumping theory predicts enhancement of the magnetic damping when the ferromagnetic layers oscillate with different amplitudes or opposite phases [48–51]. This behavior has been experimentally observed for the saturated state, where the layers magnetization are in the same direction [48, 49, 53–55]. On the other hand, the spin flop or noncollinear state has been addressed theoretically by Chiba et. al. [56], while no detailed analysis is found on the very few [47,57,58] experimental investigations found on the literature.

In this work, we study the damping and linewidth of a NiFe/Ru/NiFe SAF systems by means of broadband FMR. We measure the FMR response of two configurations, with the radio frequency field either perpendicular or parallel to the applied DC field. Over the observed acoustic and optical FMR modes, we measured, both, field and frequency linewidth all along the dispersion relation. We also calculate the FMR linewidth using a numerical model based

on the Landau Lifshitz Gilbert (LLG) equation without any additional spin torque terms. Our field linewidth results for the acoustic mode are well explained by the model, with an excellent agreement not only for the saturated region but also for the spin flop region. For the optical mode, the LLG model is not sufficient to explain the linewidth enhancement observed in the experimental data. We correlate these results to the spin pumping theory, where the interlayer spins currents compensate each other in the acoustic mode but not in the optical mode.

4.2 Sample Preparation

Synthetic antiferromagnets with structure $Ni_{81}Fe_{19}$/Ru/$Ni_{81}Fe_{19}$ were produced by DC magnetron sputtering on a SiO_2/Si(100) substrate as shown in figure 4.2. Total six samples were

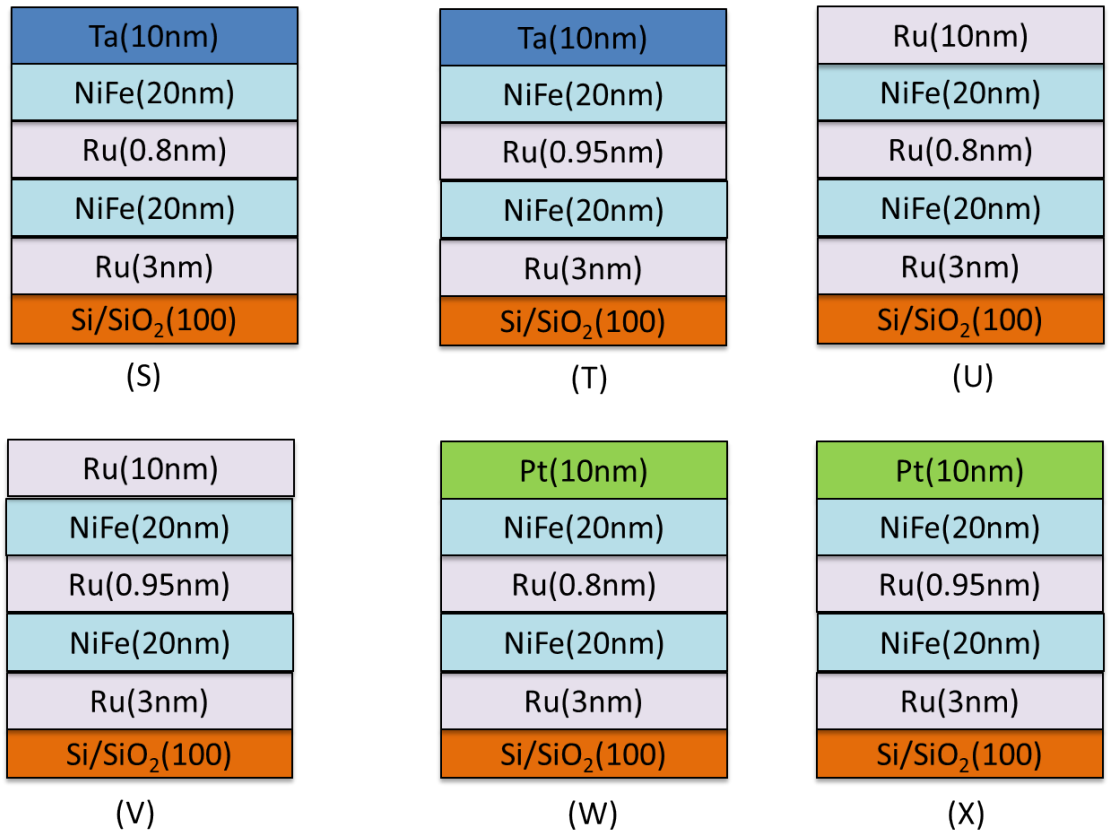

Figure 4.2: SAF structure

prepared and labelled as S, T, U, V, W and X. Ruthenium (3 nm) is used as buffer layer in all samples. Permalloy $Ni_{81}Fe_{19}$ (20 nm) is used as magnetic layers. Ru spacers (0.8 nm or 0.95

nm) are used to set up interlayer exchange coupling between both ferromagnetic layers. For capping Ta(10 nm), Ru(10 nm) and Pt(10 nm) are used.

For deposition in our sputtering chamber, we established a working pressure of 5 mTorr and Ar gas flow rate equal to 50 SCCM, after we attained a base pressure of 1×10^{-8} Torr. The deposition rates of each target were calculated by XRR and shown in the table 3.1. An in-plane magnetic field of around 1.6 kOe was applied during the film's deposition in order to induce an in-plane magnetic anisotropy. This field also keeps the magnetic layers aligned during the deposition process.

4.3 Experimental Results

4.3.1 Static magnetic measurements (M x H)

Synthetic antiferromagnets have a characteristic magnetization curve, where the relative angle between the magnetizations defines three magnetic regions: saturation, spin-flop and antiparallel [102]. These regions can be seen in the static magnetic measurements (M vs. H) with the external field H aligned with the sample anisotropy axis.

Experimental results for sample T are shown in figure. 4.3 (a), compared to a macrospin model (see section 4.4) shown as a solid green line. Figure 4.3(b) presents the angle alignment between top (T) and bottom (B) ferromagnetic layers with respect to H. The top layer is presented with red color while, the bottom layer is presented with blue color.

The relative magnetic orientation of the constituting magnetizations on a SAF defines three regions on the M vs H curve. The saturation region, is where both spins are aligned towards H, and are parallel to each other, this happens when the applied magnetic field has defeated both, the anisotropy and the interlayer exchange coupling. In figure 4.3 positive (or negative) saturation is seen for H larger than the saturation field H_{sat}. In the spin flop region, also described as the canted state or the non co-linear state, the spins deviate from the H direction and away from each other. For a symmetric SAF, as is this case, both spins deviate with the same angle with respect to the external field. This region can be observed in figure 4.3 for the

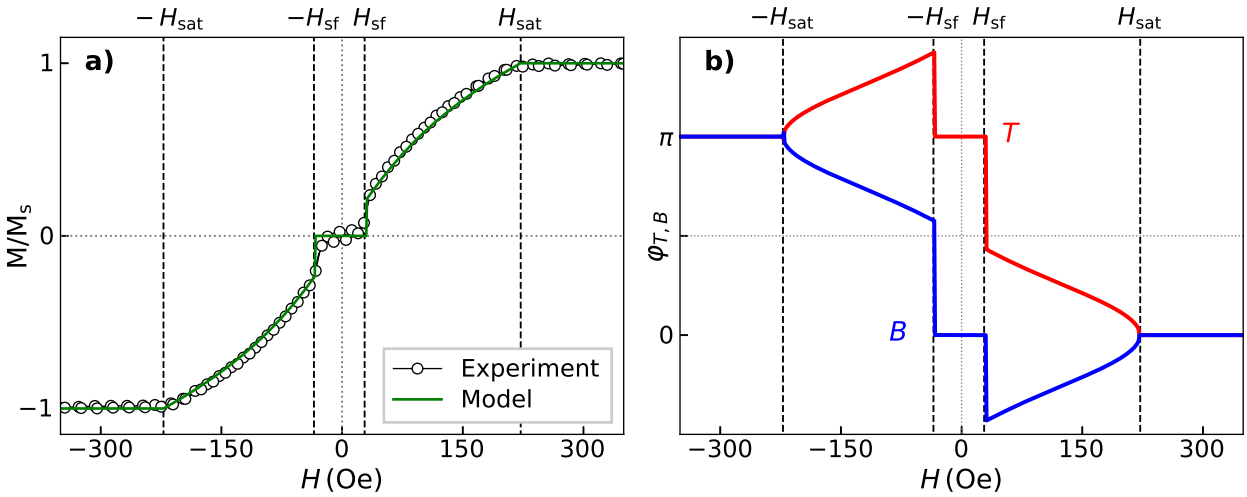

Figure 4.3: (a) Magnetization curve of the SAF system: experiment (symbols) and simulation (solid line). (b) magnetization angles φ for top T and bottom B layers with respect to applied external magnetic field direction.

fields between H_{sat} and the spin flop field H_{sf}. Near H_{sat} the angle between T and B spins is small, it increases towards H_{sf} and then at H_{sf} the spins "flops" into the anti parallel state where both spins make a $180^{\underline{o}}$ angle. The saturation H_{sat} and spin flop H_{sf} fields of sample T are shown in table 4.1.

Sample T	
Fields	Values (Oe)
H_{sat}	222
H_{sf}	33

Table 4.1: Saturation (H_{sat}) and spin flop (H_{sf}), fields of sample T

We have also performed static magnetization (M x H) measurements of all other samples mentioned in figure 4.2, and all of them shows the typical SAF behavior described before. These measurements are shown in figure 4.4. The main difference between them are the observed saturation H_{sat} and spin flop H_{sf} fields, due to the differences in the coupling fields of each sample. The difference of fields is summarized in table 4.2. Also, we observed that the magnetization curve of U and V is a bit different in antiparallel state, this difference will be

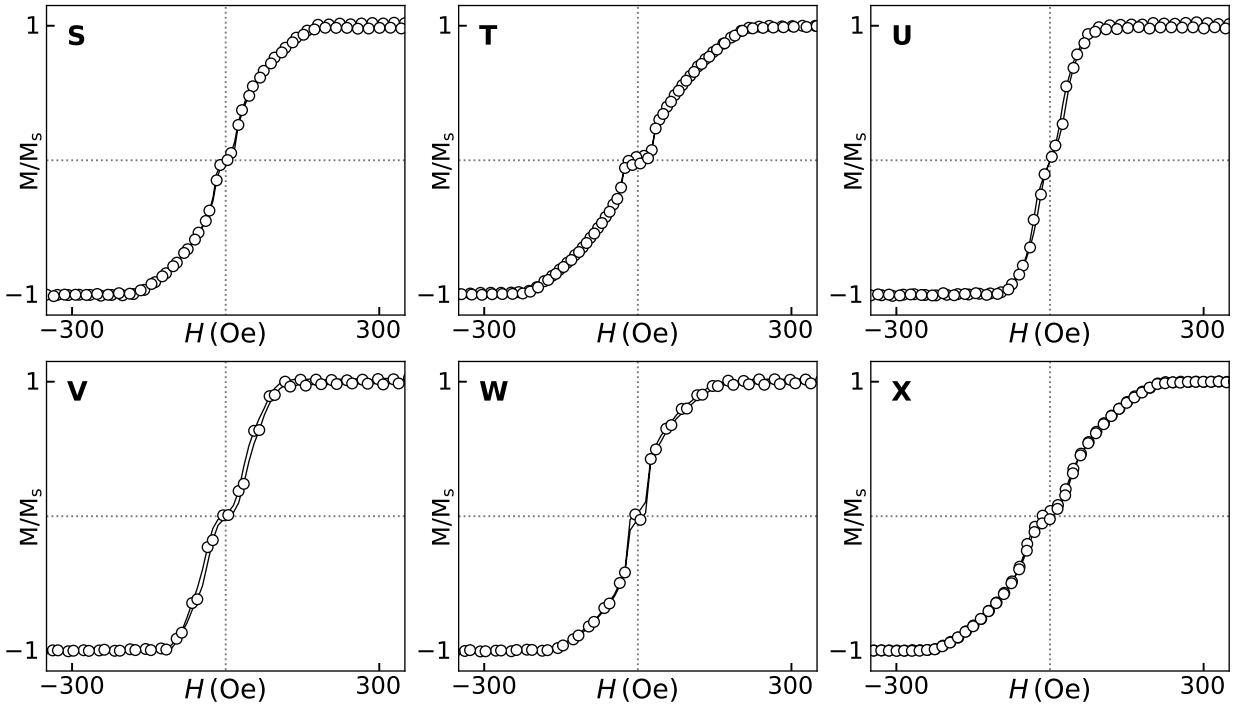

Figure 4.4: Magnetization curve of all SAF samples.

explained in broadband section. 4.5.

Samples						
Samples	S	T	U	V	W	X
H_{sat} (Oe)	168	222	78	113	171	226
$H_{sf}(Oe)$	17	33	17	26	17	33

Table 4.2: Saturation (H_{sat}) and spin flop (H_{sf}), fields, of all samples.

4.4 Macrospin LLG Model

In this thesis we have used a macrospin model to describe and calculate the magnetic behavior/anisotropies, damping and linewidth of SAF samples. The macrospin model is shown in figure 4.5. The magnetization vectors (filled arrows) are in the plane of the sample, and their orientations are defined by the angles θ and $\phi_{T/B}$ measured from the plane's normal and the easy axis (e.a.), respectively. Oscillating vectors (hollow arrows) are perpendicular to the magenetization directions. The radio field frequency h_{rf} (not shown) can be parallel or per-

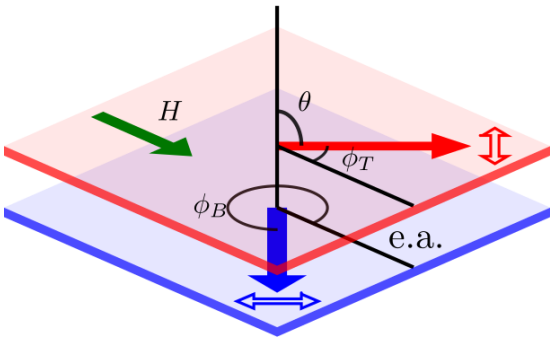

Figure 4.5: Pictorial description of our macrospin model showing top and bottom ferromagnetic layers with applied field H parallel to easy axis.

pendicular to the sample plane. The external field H (green arrow), is applied along the easy axis of the sample.

The free energy on our SAF systems is the sum of the Zeeman's, in plane uniaxial anisotropy, shape anisotropy and out-of-plane anisotropy energy contributions of each layer, plus the interaction energy. The total energy density e_{Total} of the system can be written as:

$$e_{\text{Total}} = e_T + e_B + e_I \tag{4.1}$$

where e_T and e_B are the energy density of top, bottom layers while e_I is the interaction energy density of both layers. The energy density of top layer is expressed as :

$$e_T = M_s \left[2\pi M_s (\vec{m_T}.\hat{n})^2 - \frac{1}{2} H_\perp^T (\vec{m}_T.\hat{n})^2 - H(\vec{m}_T.\hat{u}_H) - \frac{1}{2} H_K^T (\vec{m}_T.\hat{u}_{e.a})^2 \right] \tag{4.2}$$

while the energy density of bottom layer is written as :

$$e_B = M_s \left[2\pi M_s (\vec{m_B}.\hat{n})^2 - \frac{1}{2} H_\perp^B (\vec{m}_B.\hat{n})^2 - H(\vec{m}_T.\hat{u}_H) - \frac{1}{2} H_K^B (\vec{m}_B.\hat{u}_{e.a})^2 \right] \tag{4.3}$$

and the interaction energy is written as :

$$e_I = M_S \left[-H_{J1} (\vec{m_T}.\vec{m_B}) + H_{J2} (\vec{m_T}.\vec{m_B})^2 \right] \tag{4.4}$$

where $H_{J1} = \frac{J_1}{tM_S}$, $H_{J2} = \frac{J_2}{tM_S}$, $M_S(emu/cm^3)$ is saturation magnetization of Permalloy and

t is the thickness, $\vec{m}_T$ and $\vec{m}_B$ are the unit vectors that indicate the magnetization direction of top and bottom layers, $\hat{n}$ is the unit vector normal to the sample surface, $\vec{u}_{e.a}$ is a vector that defines the uniaxial anisotropy axis , and H, $H_\perp$ and H_k are the external, out-of-plane anisotropy and in-plane sample anisotropy fields, respectively.

For the analysis of the system, it is convenient to express the free energy in terms of the polar θ and azimuthal ϕ angles of the magnetization. In this model the magnetization is considered always in the plane of films, so $\theta = \frac{\pi}{2}$. The external field is applied in the direction of easy axis. And we suppose we have a symmetric SAF, therefore, $H_\perp^T = H_\perp^B = H_\perp$ and $H_k^T = H_k^B = H_k$. Under these conditions, for the spin flop and saturated states, both layers deviates with same angle from the anisotropy axis, thus the in plane angles ϕ can be written as:

$$\phi_T = 2\pi - \phi_B = \phi, \tag{4.5}$$

The normalized free energy density ($\eta = \frac{e}{M_s}$) can be expressed keeping only the terms dependent on ϕ, such as:

$$\eta_T = \eta_B = -H\cos(\phi) - \frac{1}{2}H_k\cos^2(2\phi) \tag{4.6}$$

and

$$\eta_I = -H_{J1}\cos(2\phi) + H_{J2}\cos^2(\phi) \tag{4.7}$$

We can then obtain the magnetization equilibrium angle ϕ values by minimizing $\eta = \eta_T + \eta_B + \eta_I$ for each H field value along the hysteresis curve.

To calculate the magnetic dynamic properties, we used the model described in reference [78]. The dispersion relation is calculated by solving the eigenvalue problem shown in equation 4.8, by obtaining $\omega_r = 2\pi f_r$ as a function of H.

$$-\Lambda\eta_{\Omega\Omega}\delta\Omega = j\omega_r\delta\Omega \tag{4.8}$$

where

$$[\Lambda] = \frac{\gamma}{1+\alpha^2}\begin{pmatrix} \alpha & 1 & 0 & 0 \\ -1 & \alpha & 0 & 0 \\ 0 & 0 & \alpha & 1 \\ 0 & 0 & -1 & \alpha \end{pmatrix} \tag{4.9}$$

and $\alpha_T = \alpha_B = \alpha$ are the intrinsic damping of our top and bottom ferromagnetic layers. The $\eta_{\Omega\Omega}$ matrix is composed by the derivatives of the normalized free energy density with respect to the ϕ and θ angles

$$\eta_{\Omega\Omega} = \begin{pmatrix} \partial_{\theta_T}\partial_{\theta_T}\eta & \partial_{\theta_T}\partial_{\phi_T}\eta & \partial_{\theta_T}\partial_{\theta_B}\eta & \partial_{\theta_T}\partial_{\phi_B}\eta \\ \partial_{\phi_T}\partial_{\theta_T}\eta & \partial_{\phi_T}\partial_{\phi_T}\eta & \partial_{\phi_T}\partial_{\theta_B}\eta & \partial_{\phi_T}\partial_{\phi_B}\eta \\ \partial_{\theta_B}\partial_{\theta_T}\eta & \partial_{\theta_B}\partial_{\phi_T}\eta & \partial_{\theta_B}\partial_{\theta_B}\eta & \partial_{\theta_B}\partial_{\phi_B}\eta \\ \partial_{\phi_B}\partial_{\theta_T}\eta & \partial_{\phi_B}\partial_{\phi_T}\eta & \partial_{\phi_B}\partial_{\theta_B}\eta & \partial_{\phi_B}\partial_{\phi_B}\eta \end{pmatrix} = \begin{pmatrix} \eta_{\theta_T\theta_T} & \eta_{\theta_T\phi_T} & \eta_{\theta_T\theta_B} & \eta_{\theta_T\phi_B} \\ \eta_{\phi_T\theta_T} & \eta_{\phi_T\phi_T} & \eta_{\phi_T\theta_B} & \eta_{\phi_T\phi_B} \\ \eta_{\theta_B\theta_T} & \eta_{\theta_B\phi_T} & \eta_{\theta_B\theta_B} & \eta_{\theta_B\phi_B} \\ \eta_{\phi_B\theta_T} & \eta_{\phi_B\phi_T} & \eta_{\phi_B\theta_B} & \eta_{\phi_B\phi_B} \end{pmatrix} \tag{4.10}$$

The non zero values of the matrix $\eta_{\Omega\Omega}$ are:

$$\begin{aligned} \eta_{\theta_T\theta_T} = \eta_{\theta_B\theta_B} &= 4\pi M_{\text{eff}} + H\cos\phi + H_k\cos^2\phi + H_{J1}\cos 2\phi - 2H_{J2}\cos^2 2\phi \\ \eta_{\phi_T\phi_T} = \eta_{\phi_B\phi_B} &= H\cos\phi + H_k\cos^2 2\phi + H_{J1}\cos 2\phi - 2H_{J2}\cos^2 4\phi \\ \eta_{\theta_T\theta_B} = \eta_{\theta_T\theta_B} &= -H_{J1} + 2H_{J2}\cos 2\phi \\ \eta_{\phi_T\phi_B} = \eta_{\phi_B\phi_T} &= -H_{J1}\cos 2\phi + 2H_{J2}\cos 4\phi \end{aligned} \tag{4.11}$$

where M_{eff} is the effective magnetization

$$M_{\text{eff}} = M_S - H_\perp/4\pi \tag{4.12}$$

For power absorption calculations, we first obtain the susceptibility tensor $[X]$, (see equation 6.17 of reference [78])

$$[X] = [j2\pi f + \eta_{\Omega\Omega}]^{-1} \tag{4.13}$$

and then the mean absorbed power is calculated by

$$< P >= \pi f \sum_{k,l=1}^{n} h^{rf}_{\mathbf{\Omega}k}[\boldsymbol{X}_{kl}]h^{rf}_{\mathbf{\Omega}l} \tag{4.14}$$

where, for $h_{rf} \perp H$

$$h^{rf}_{\Omega} = |h^{rf}| \begin{bmatrix} 0 \\ \cos\phi \\ 0 \\ \cos\phi \end{bmatrix} \tag{4.15}$$

and for $h_{rf} \parallel H$

$$h^{rf}_{\mathbf{\Omega}} = |h^{rf}| \begin{bmatrix} 0 \\ -\sin\phi \\ 0 \\ \sin\phi \end{bmatrix} \tag{4.16}$$

As $< P >$ is calculated for all fields H and frequencies f, we can also calculate the derivatives $\frac{d<P>}{dH}$ numerically.

Oscillation modes

In a magnetic system, coupled spins can oscillate simultaneously in different resonance modes. For example, in the case of two spins in FMR, acoustic mode appears when the two spins oscillate in phase (0°) , and an optical mode appears when the oscillation is out of phase (180°). To discuss these cases, it is necessary to analyze the spin oscillating part of magnetization vector. For the case of harmonic oscillations, the $\delta\boldsymbol{M}_i$ oscillating vectors are:

$$\delta\boldsymbol{M}^i = M^i_S[\delta\theta_i\hat{\theta}_i + \sin\theta_i\delta\phi_i\hat{\phi}_i] \tag{4.17}$$

where

$$\hat{\theta}_i = \cos\phi_i \cos\theta_i \hat{x} + \sin\phi_i \cos\theta_i \hat{y} - \sin\theta_i \hat{z} \tag{4.18}$$

$$\hat{\phi}_i = -\sin\phi_i \hat{x} + \cos\phi \hat{y}$$

define the unit vectors perpendicular to the magnetization vector of element i. It can be seen from equation (4.17) that the amplitude and instantaneous direction of the oscillating vector depends of the intensities and temporal phases of $\delta\theta_i$ and $\delta\phi_i$, and also of the angles θ_i and ϕ_i that define the orientation of the magnetization vector. The oscillation modes can then be described as the different possible configurations of the oscillating vectors. As an example,

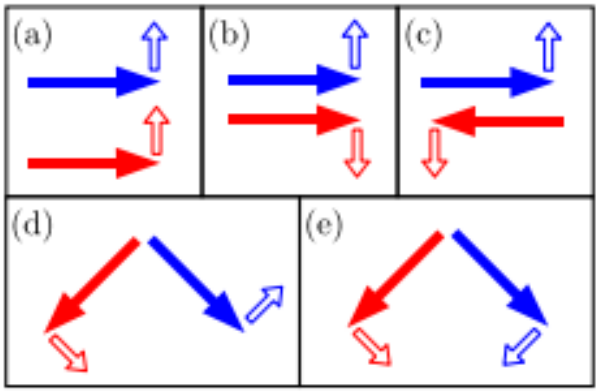

Figure 4.6: Examples of oscillation modes for different magnetic configurations in a two-spin system. Magnetization vectors (filled arrows) and oscillating vectors (hollow arrows) are shown. The magnetizations are shown in parallel states (a) and (b), antiparallel states (c) and non-collinear states (d) and (e). At oscillations are in phase in (a), (c) and (d) or out of phase in (b) and (e).

in figure 4.6 some simple cases of oscillation modes are presented for a system of two spins oscillating in a plane $\theta_i = \frac{\pi}{2}, \delta\theta_i = 0$. The static magnetization vectors are represented by filled arrows and oscillating vectors δM by hollow arrows. The time phase (0° or 180°) of δM is represented by the direction of the hollow arrow in relation to the magnetization vector arrow. Cases (a) and (b) present magnetized spins in the same direction (as in the case of saturation system). In case (a) the oscillating vectors are in phase, and corresponds to the acoustic mode.

The optical mode is represented in the case (b) where the oscillating vectors are out of phase. Cases (c), (d) and (e) present spins outside the saturation setting. In case (c) the oscillations are in phase, but due to the configuration of antiparallel spins the oscillating vectors are in a configuration similar to that of the mode optics of the case (b). In cases (d) and (e), in phase and out of phase, respectively, the oscillating vectors are no longer collinear due to the direction of the respective magnetization vectors. It is clear that to analyze the oscillation modes it is necessary to know the angles that define the directions of the system spins and the $\delta\Omega$ oscillations of these angles.

4.5 Broadband FMR

Broadband ferromagnetic resonance measurements were performed using a short-circuited microstrip waveguide (the whole setup is shown in figure 4.7). The microstrip contains the

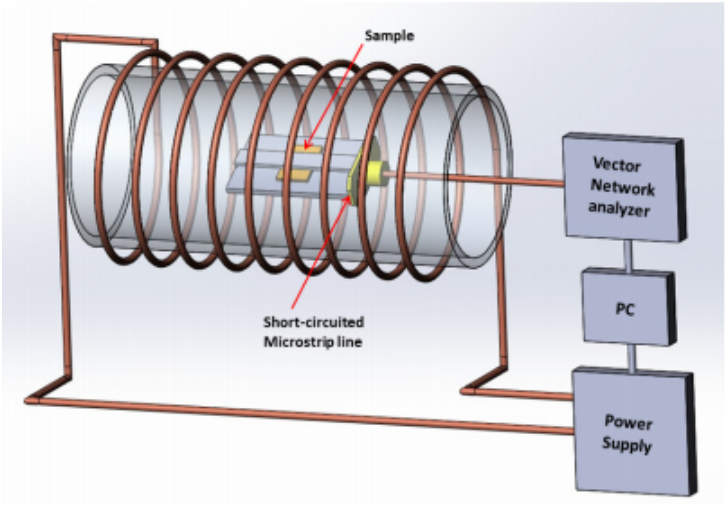

Figure 4.7: Micro-strip method for VNA-FMR differential measurements.

sample and is connected to vector network analyzer (VNA). The microstrip waveguide can generate a rf signal (10MHz to 26GHz) on the sample surface. H_{DC} is applied through a solenoid connected to a Kepco power supply. The whole setup is controlled through a computer (PC). The absorbed power (P) in the magnetic sample was obtained from the S_{11} parameter measured

by the vector network analyzer with respect to the substrate reference P_{ref}.

$$P = 1 - |S_{11}|^2 - P_{ref} \tag{4.19}$$

We measured the broadband absorbed power spectra of all our samples with, both, the radio frequency field h_{rf} parallel and perpendicular to the DC field H.

The SAF systems present two oscillating modes , in phase precession FMR mode (acoustic) and out of phase precession FMR mode (optical) of top and bottom magnetizations. These two modes are shown in figure 4.8, where top and bottom magnetizations are represented as

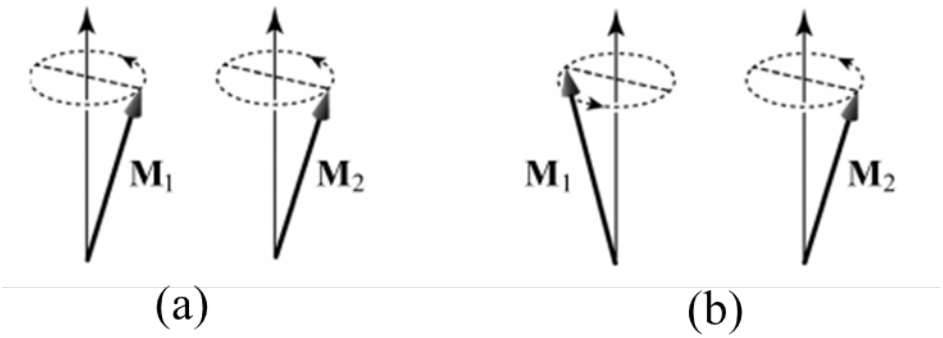

Figure 4.8: (a) Ferromagnetic acoustic mode and, (b) optical mode

M_1 and M_2 respectively.

The broadband results of Sample T are shown in the figure. 4.9 (a and b). In this figure, the color scale denotes P amplitude from blue (minimum) to red (maximum). The amplitude maxima on the branches correspond to the resonant modes. As we can observe, both measurement schemes ($h_{rf} \perp H$, figure. 4.9 a) and ($h_{rf} \parallel H$, figure. 4.9 b), are complementary to each other. In the saturation region, we only observe the acoustic resonance mode, where the spins precess in phase to each other. In this region, for our symmetric SAF, the optical mode (out-of-phase mode) can not be excited with a uniform h_{rf}. On the other hand, in the spin flop region, we can observe both resonant modes due to the relative orientation of h_{rf} to the oscillating magnetizations. In the antiparallel state, only the higher frequency mode is excited by $h_{rf} \perp H$.

Figure 4.9 also includes the dispersion relations calculated using the macro spin model (see

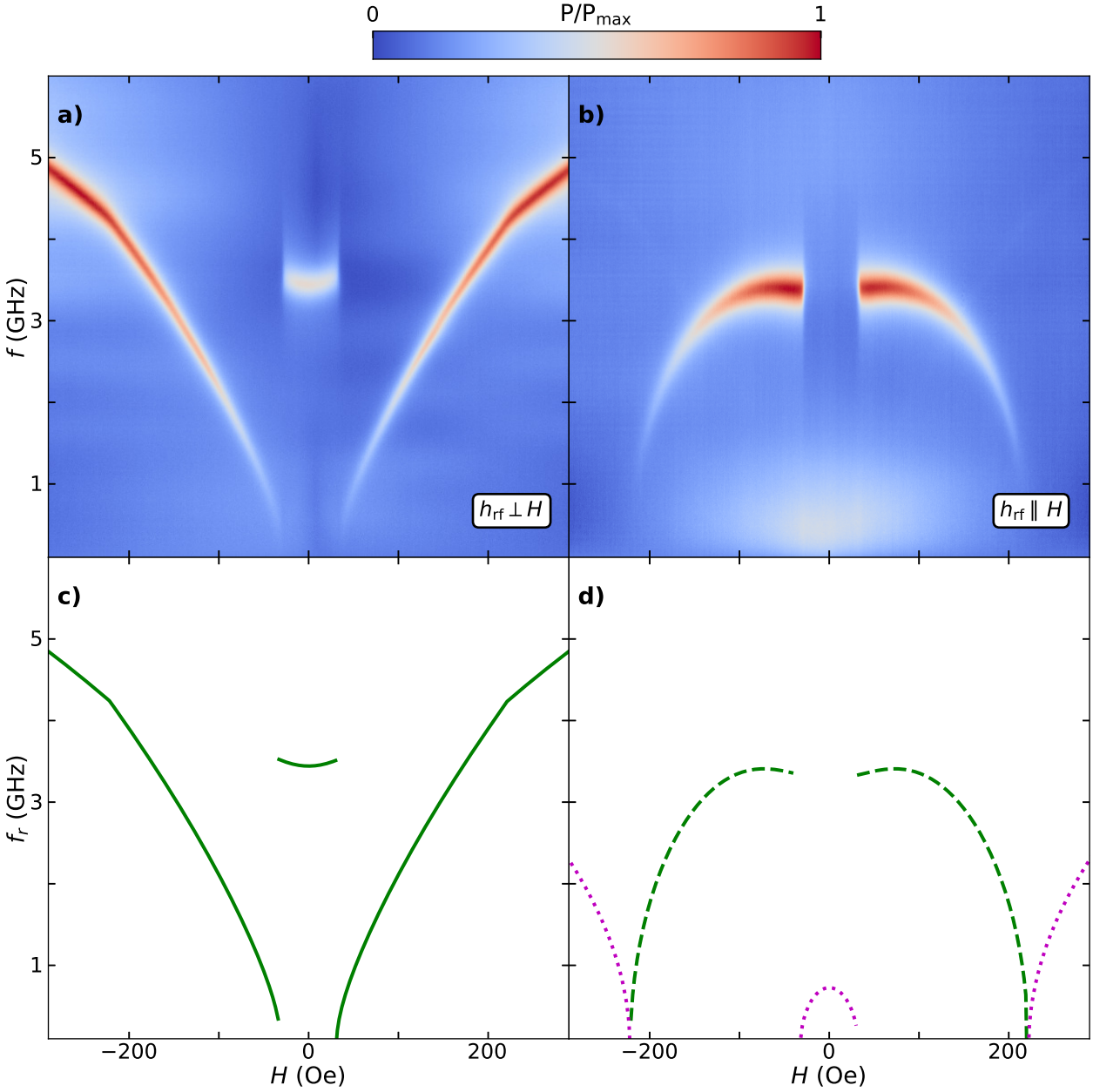

Figure 4.9: Experimental broadband spectra for our SAF (T) measured with (a) $h_{\mathrm{rf}} \perp H$. (b): same as (a) but with $h_{\mathrm{rf}} \parallel H$. (c) Dispersion relations for the acoustic mode (green solid lines) and (d) Optical mode (dashed green lines). The optical mode is observed (dashed lines) only on the spin flop state. Resonant conditions not excited by an uniform h_{rf} are drawn as dotted magenta lines.

section 4.4). In figure 4.9 c, the dispersion relation of the acoustic mode is presented by a continuous green line while in figure 4.9 d, the optical mode are presented by a dashed green line. The magenta dotted line presents the modes which could not be excited with uniform rf

field. The parameters used in the dispersion relation calculation of sample T are presented in table 4.3

Sample T	
magnetic anisotrpies	Values
$H_k^T = H_k^B = H_k(Oe)$	7
H_{J1} (Oe)	-94
H_{J2} (Oe)	10.2
M_{eff} (emu/cm^3)	780

Table 4.3: Parameters used in dispersion relation calculation of sample T

The broadband measurements for all the other samples also showed similar results, and are shown below one by one.

FMR spectra of sample S is shown in figure 4.10. In this figure, for $h_{rf} \perp H$, we observed that the broadband spectra is of V shape and a transition from H_{sf} to H_{sat} is observed as a change in the slope of the dispersion relations. Also the resonant mode of antiparallel state is shifted towards a lower frequency when compared to sample T, this effect is due to lower coupling constants H_{J1} and larger H_{J2}. We also observe a clear arc shape in optical modes wich is more bent when compared to sample T this is due to the larger H_{J2} coupling. In figure 4.10 c, the dispersion relation of the acoustic mode is presented by a continuous green line while in figure 4.10 d, the optical mode are presented by a dashed magenta line, this time we did not differentiate the regions where this mode is observed or excited.

The broadband spectra of sample U and V are shown in figure 4.11 and 4.12, respectively. Coupling fields for sample U are H_{J1} = -33 Oe and H_{J2} = 3.5 Oe. For these values we can expect the shifting of the spin flop and antiparallel state FMR modes to lower frequencies and fields. Similarly, coupling fields for sample V are H_{J1} = -56 Oe and H_{J2} = 3 Oe. Therefore, we observe a similar behavior of resonant modes.

For U and V samples, we observed that the antiparallel state is not fully straight in the M

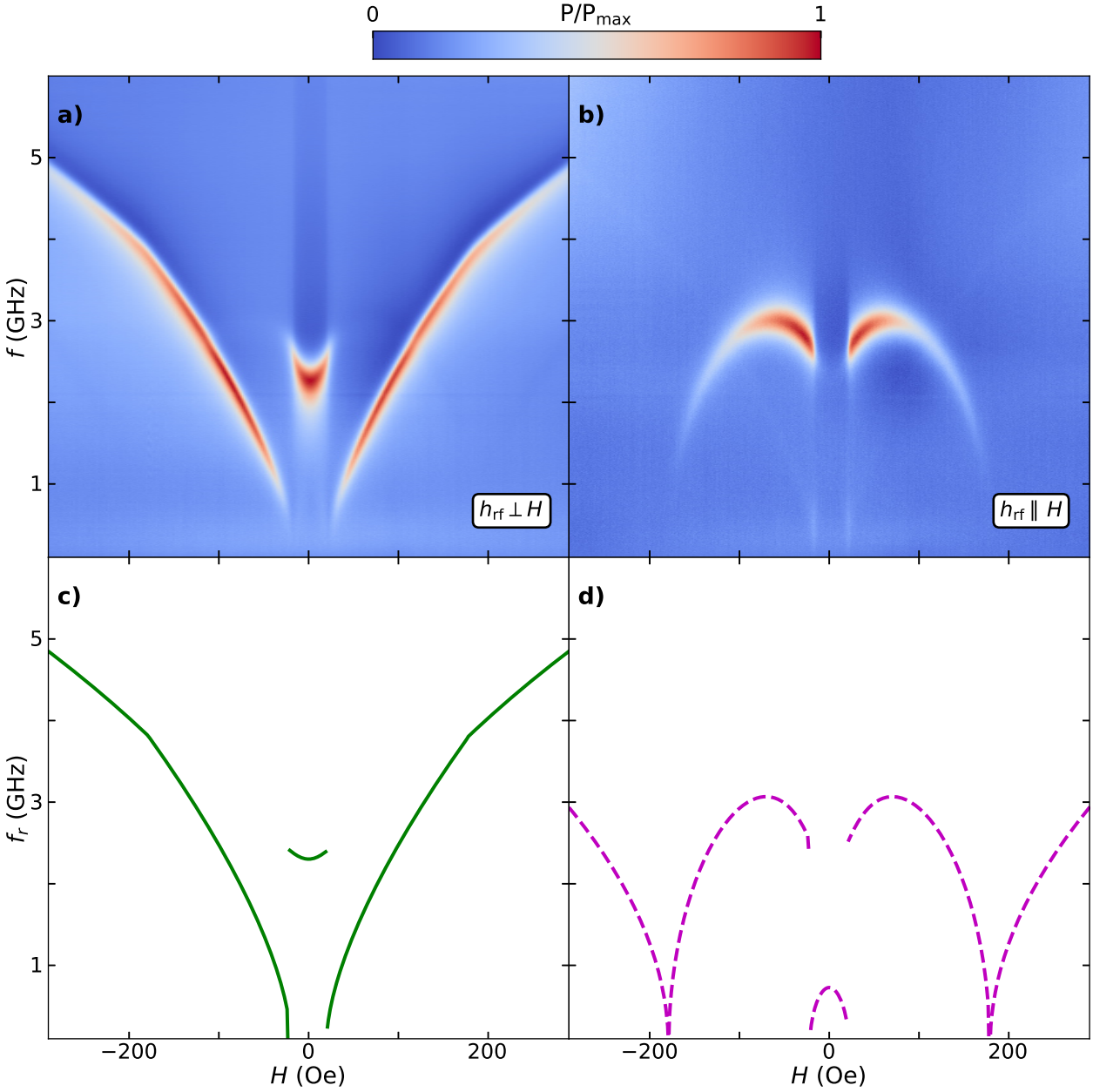

Figure 4.10: Experimental broadband spectra of S, measured with (a) $h_{\mathrm{rf}} \perp H$. (b): same as (a) but with $h_{\mathrm{rf}} \parallel H$. (c) Dispersion relations for the acoustic mode (green solid lines) and (d) Optical mode (dashed green lines). The optical mode is observed (dashed lines) only on the spin flop state.

x H curves. They also have different broadband spectra for $h_{\mathrm{rf}} \parallel$ H as compared to other samples. The experimental resonant modes are sharper in the spin flop region than the calculated dispersion relation. We have also noticed that they have less effective magnetization value as compared to other samples. We attribute these effects to a large out of plane anisotropy $H_{\perp}$

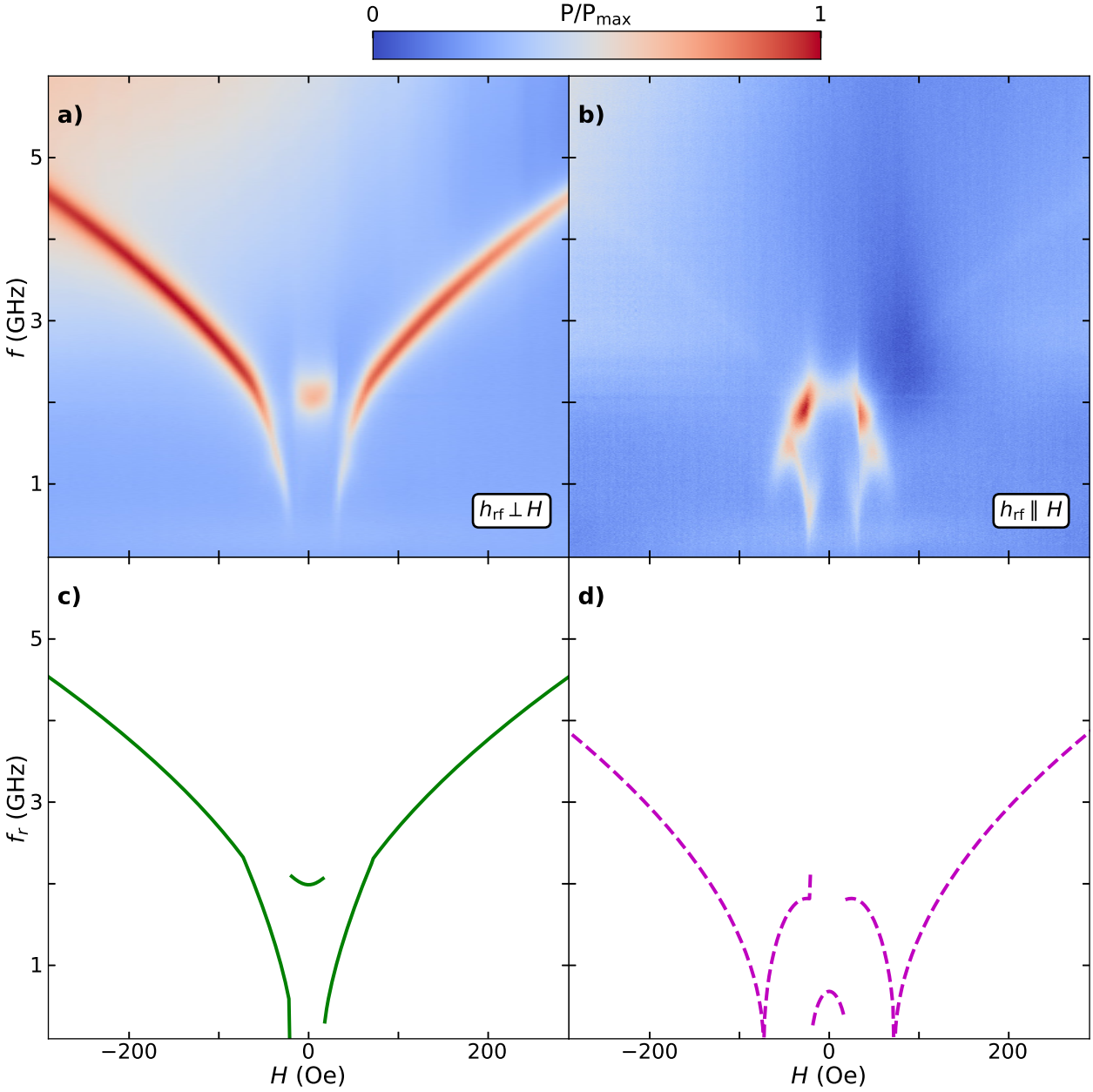

Figure 4.11: Experimental broadband spectra of U, measured with (a) $h_{rf} \perp H$.(b): same as (a) but with $h_{rf} \parallel H$. (c) Dispersion relations for the acoustic mode (green solid lines) and (d) Optical mode (dashed green lines). The optical mode is observed (dashed lines) only on the spin flop state.

that not only reduces the effective magnetization (see table 4.4) but could also make that the spin flop transition occurs with out of plane components in the layers' magnetization. This later effect is not taken into account in our model.

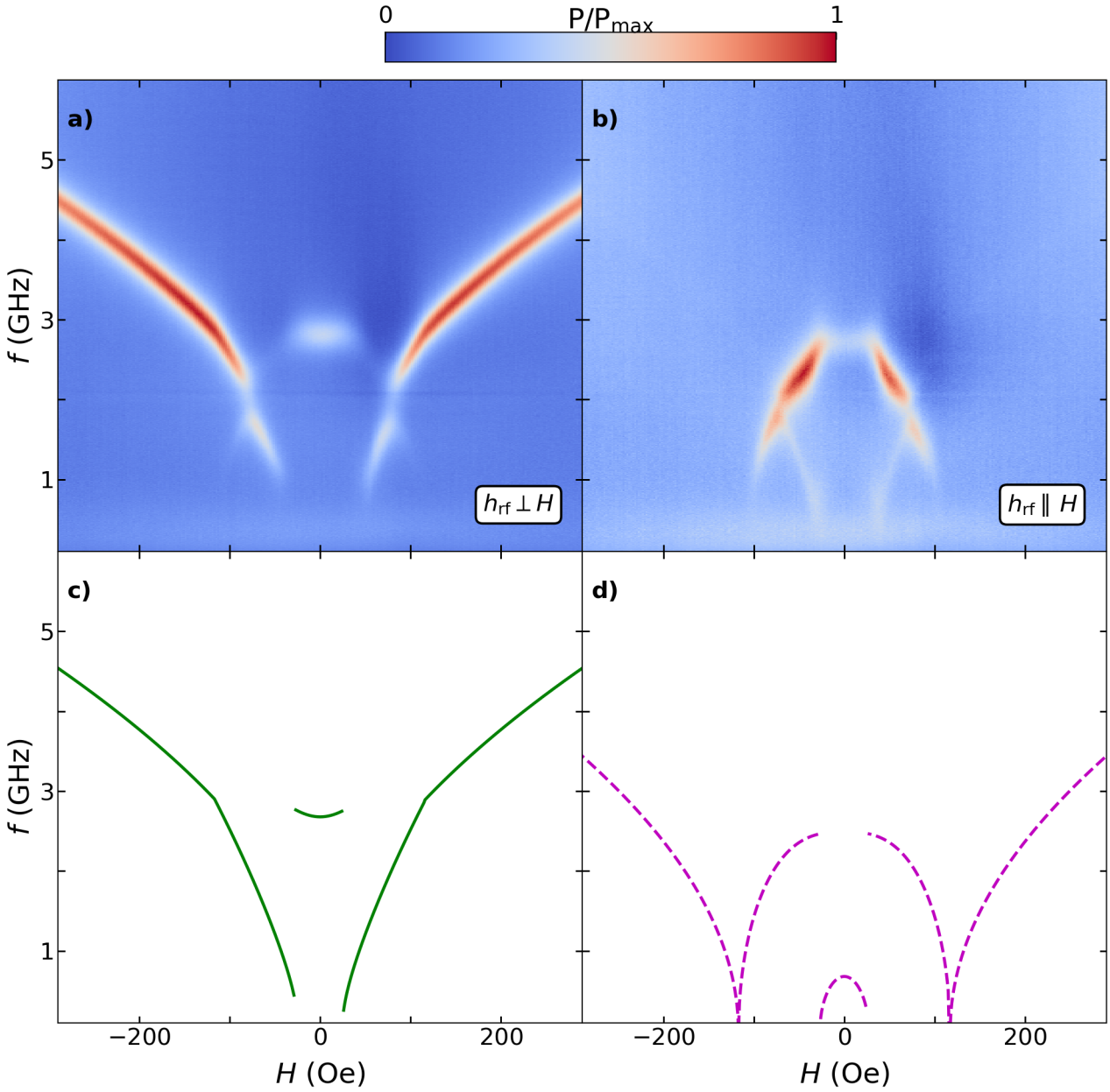

Figure 4.12: Experimental broadband spectra of V, measured with (a) $h_{rf} \perp H$. (b): same as (a) but with $h_{rf} \parallel H$. (c) Dispersion relations for the acoustic mode (green solid lines) and (d) Optical mode (dashed green lines). The optical mode is observed (dashed lines) only on the spin flop state.

The broadband spectra of samples W and X are shown in figures 4.13 and 4.14. These samples behave very similar to samples S and T, including similar H_{J1} and H_{J2} coupling fields, but have a slightly smaller efective magnetization (see table 4.4)

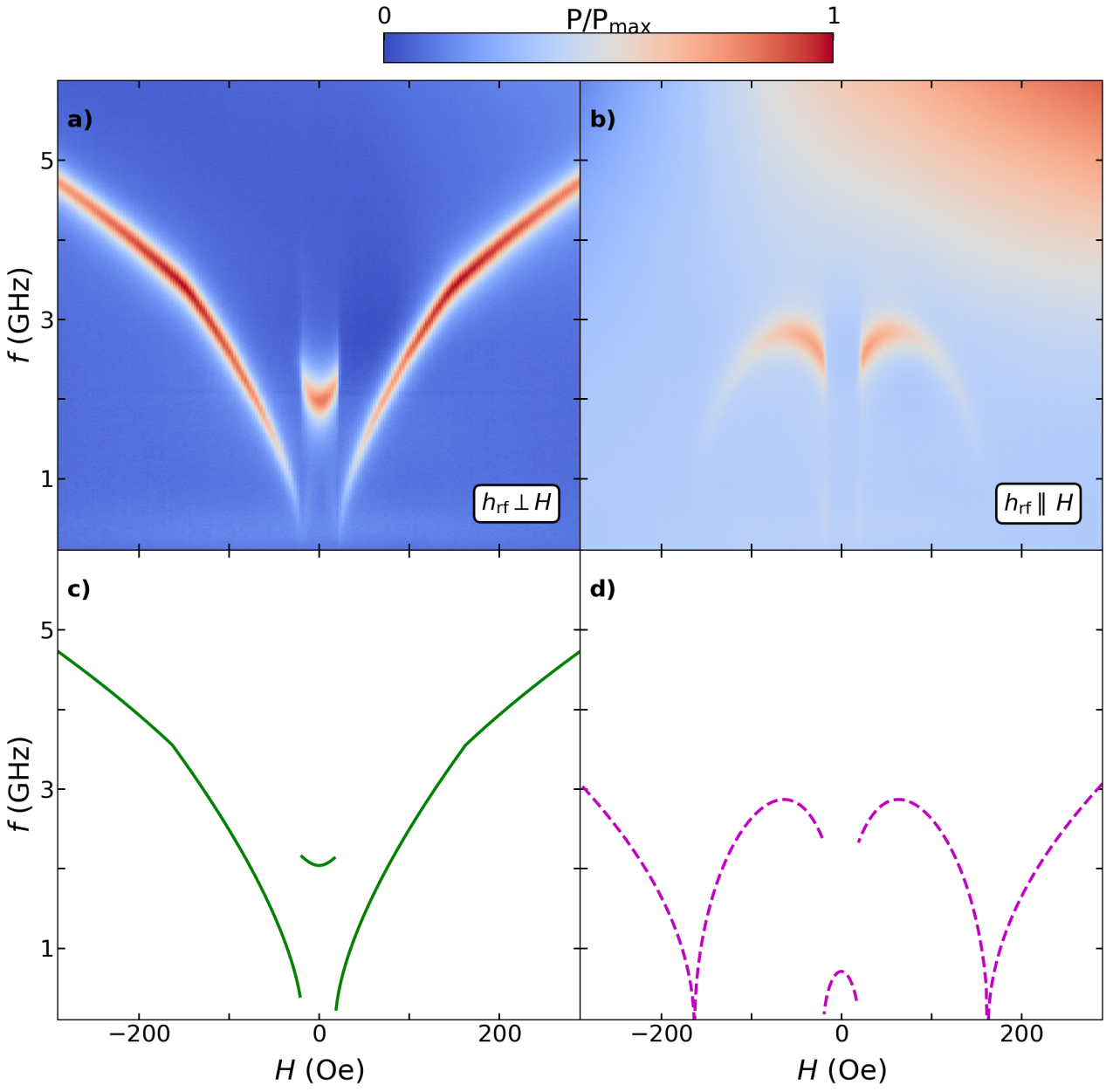

Figure 4.13: Experimental broadband spectra of W, measured with (a) $h_{rf} \perp H$.(b): same as (a) but with $h_{rf} \parallel H$. (c) Dispersion relations for the acoustic mode (green solid lines) and (d) Optical mode (dashed green lines). The optical mode is observed (dashed lines) only on the spin flop state.

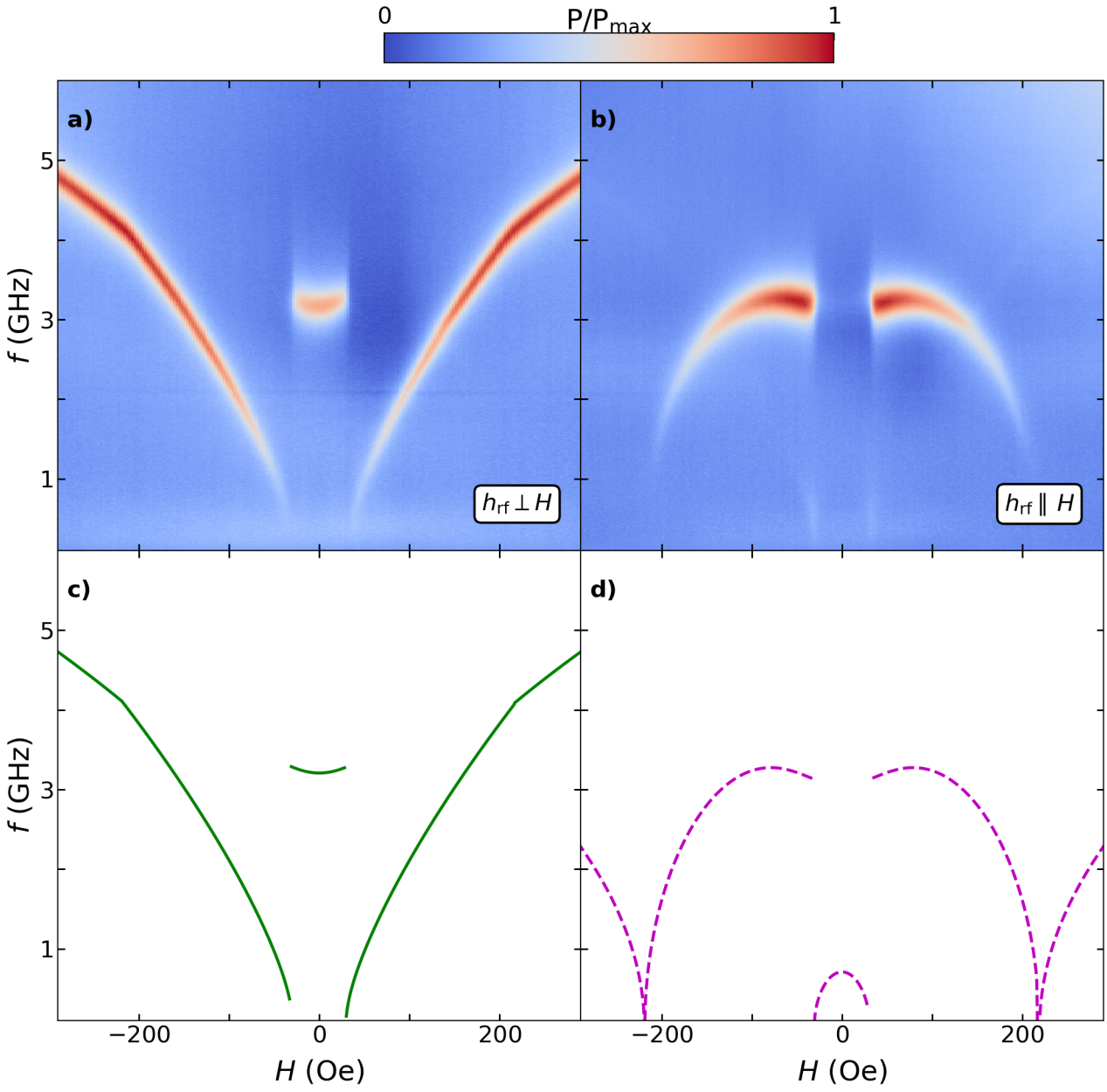

Figure 4.14: Experimental broadband spectra of X, measured with (a) $h_{\mathrm{rf}} \perp H$.(b): same as (a) but with $h_{\mathrm{rf}} \parallel H$. (c) Dispersion relations for the acoustic mode (green solid lines) and (d) Optical mode (dashed green lines). The optical mode is observed (dashed lines) only on the spin flop state.

We summarize the magnetic anisotropies obtained from dispersion relations of all samples in table 4.4

Samples						
Samples	S	T	U	V	W	X
H_k (Oe)	7	7	7	7	7	7
H_{J1} (Oe)	-62	-94	-33	-56	-55	-90
H_{J2} (Oe)	15.5	10.2	3.5	3	15	11.5
M_{eff} (emu / cm^3)	780	780	680	680	740	744

Table 4.4: Parameters used in broadband FMR for calculations of anisotropies

We can see that the difference between the samples are only the coupling fields, which is expected to change with the Ru thickness and the small differences during the fabrication process. But we also observe different effective magnetization which should be attributed to the capping of the top layer, and thus affect only this layer making the SAF not symmetric. Even so our symmetric model explains very well all samples.

4.6 Linewidth and damping

In order to obtain precise linewidth ΔH and damping α measurements in acoustic and optical mode, we calculated the absorbed power derivatives dP/dH with respect to the applied field for $h_{rf} \perp H$ and $h_{rf} \parallel H$. This is performed by doing accurate measurements of S_{11} at $H \pm \delta H$ were $\delta H = 2$ Oe and then calculate the derivative numerically:

$$\frac{dP}{dH} = \frac{(|S_{11}|^2_{(H-\delta H)} - |S_{11}|^2_{(H+\delta H)})}{2\delta H} \tag{4.20}$$

For sample T, dP/dH measurements were carried over fixed frequencies, while sweeping H and also for a broadband frequency around a fixed field. In all our measurements we apply h_{rf} either perpendicular to H or parallel to H. For both $h_{rf} \perp H$ and $h_{rf} \parallel H$, the dP/dH measurements

over fixed frequencies and sweeping H, are shown in figure 4.15. For $h_{rf} \perp H$, the absorbed

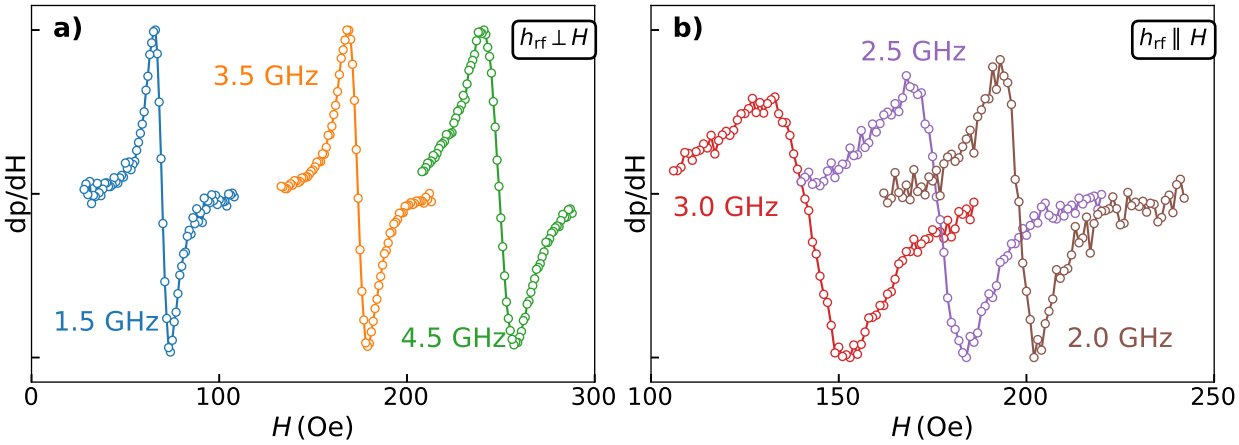

Figure 4.15: (a) For $h_{rf} \perp H$, absorbed power derivative $\frac{dP}{dH}$ vs H at fixed frequency of 1.5 GHz , 3.5 GHz and 4.5 GHz (b) For $h_{rf} \parallel H$, absorbed power derivative $\frac{dP}{dH}$ vs H at fixed frequency of 3.0 GHz , 2.5 GHz and 2.0 GHz.

power derivatives vs field for 1.5 GHz , 3.5 GHz and 4.5 GHz are shown in figure 4.15a. From these spectra we can obtain values of resonance field H_R and ΔH. At higher frequencies, we observe those resonant modes, occur at high magnetic field and vice versa Similarly, for $h_{rf} \parallel H$, the absorbed power derivatives vs field for 2 GHz , 2.5 GHz and 3 GHz are shown in figure 4.15b. We observe that with high frequency, we can excite the resonant modes, occur at low magnetic field and vice versa. For sample T, absorbed power derivatives vs frequencies over a fixed field of 75 Oe, 150 Oe and 260 Oe are shown in figure 4.16a, when $h_{rf} \perp H$. We can calculate resonance frequency f_r and frequency linewidth Δf from each dP/dH. Moreover, lower magnetic field corresponds to resonant modes at lower resonant frequency.

For $h_{rf} \parallel H$, absorbed power derivatives vs frequencies over a fixed field of 200 Oe, 150 Oe and 100 Oe are shown in figure 4.16b. For optical mode, we can calculate resonance frequency f_r and frequency linewidth Δf from each dP/dH.

For $h_{rf} \perp H$, dP/dH vs f, has a positive slope around resonant field and for $h_{rf} \parallel H$ the slope is negative. This is due to the opposite dispersion relation slopes of the optical and acoustic modes around the measurement field.

By fitting the dP/dH using equation 3.6 measurements we obtained the field linewidth ΔH or frequency linewidth Δf for both, optical and acoustic, modes. Also, using our LLG model

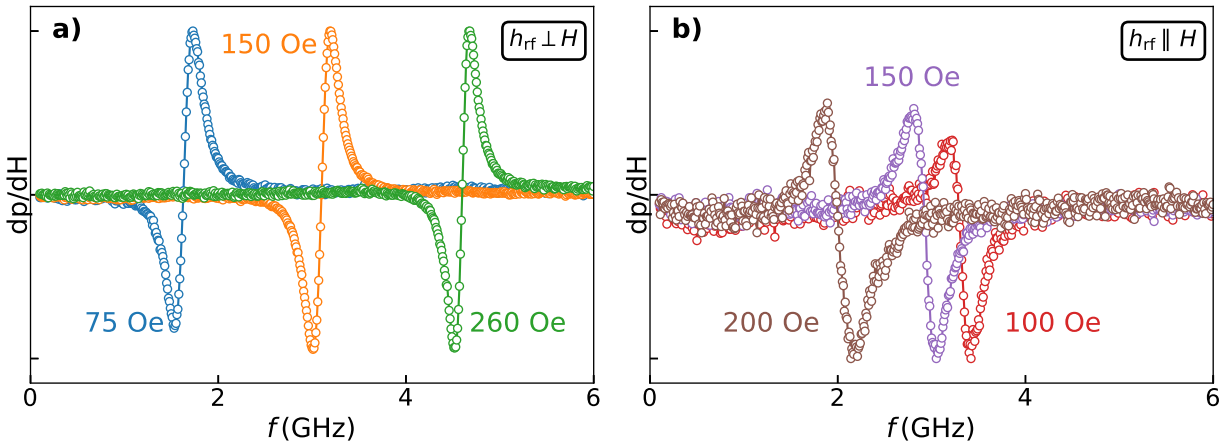

Figure 4.16: (a) For $h_{rf} \perp H$, absorbed power derivative dP/dH vs f at fixed field of 75 Oe , 150 Oe and 260 Oe. (b) For $h_{rf} \parallel H$, absorbed power derivative dP/dH vs f at fixed field of 200 Oe , 150 Oe and 100 Oe.

described in section 4.4, we obtained the dP/dH and from there we have calculated ΔH or Δf, numerically. These numerical solutions only take into account the LLG equation without spin pumping or spin torque effects.

The experimental results of ΔH vs. f are shown in figure. 4.17. In this figure, we observe that ΔH increases with f. For the acoustic mode, we see two different regimes, one for the spin flop region and the other for the saturated region, with a significant increment in ΔH in the transition between these regions at around 4.3 GHz. The optical mode has always larger experimental ΔH when compared to the acoustical mode, also the growth rate is much larger. In figure. 4.17 we also present the ΔH calculations from our LLG model with the addition of a constant $\Delta H_0 = 2.3$ Oe. For optical mode, on the contrary of the calculated results, ΔH is smaller than on the acoustic mode up to around 2.7 GHz. We also noticed that, for this mode, the growth rate on the experimental ΔH is larger than the obtained from the LLG model.

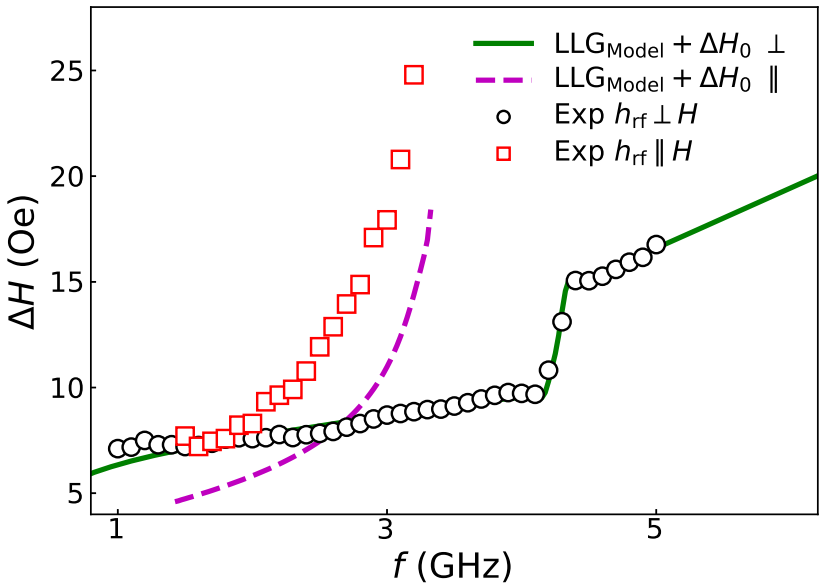

Figure 4.17: Field linewidth measurements vs. frequency for the acoustic mode (circles) and the optical mode (squares). The corresponding numerical values obtained using an LLG model plus a manually added $\Delta H_0 = 2.3$ Oe: acoustic mode (solid line) and optical mode (dashed line).

In order to compare linewidth in different magnetic states, we must look upon the frequency linewidth Δf measured at a fixed H, where the magnetic state is stable. These measurements are shown in the top panel of figure. 4.18.

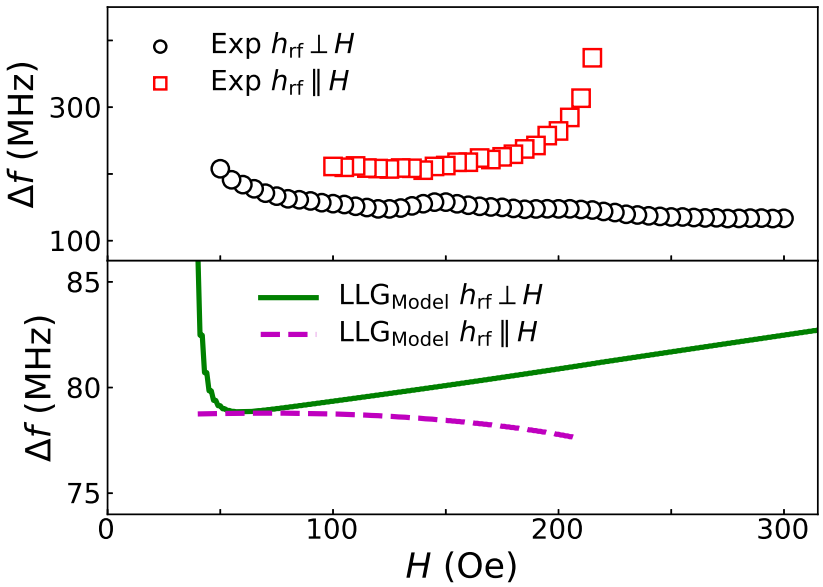

Figure 4.18: Top: Experimental frequency linewidth Δf for the acoustic (circles) and optical (squares) modes as a function of measured field H. Bottom: numerically calculated Δf from the LLG model for the acoustic (solid line) and optical (dashed line) modes.

Here, we observe that for the acoustic mode, experimental Δf is almost continuous and slightly decreases with the field. While Δf for the optical mode has a larger value and slowly increases with the field up to 200 Oe, where then sharply increases. Calculated Δf values are also shown in the bottom panel of figure. 4.18. The LLG model does not display any abrupt transition on Δf between the spin flop and saturation region for the acoustic mode. Also, for the LLG model Δf the optical mode is always smaller than the acoustic mode.

Other samples also showed the similar behavior in acoustic and optical modes all along the dispersion relation. The acoustic mode ΔH results are shown in figure 4.19.

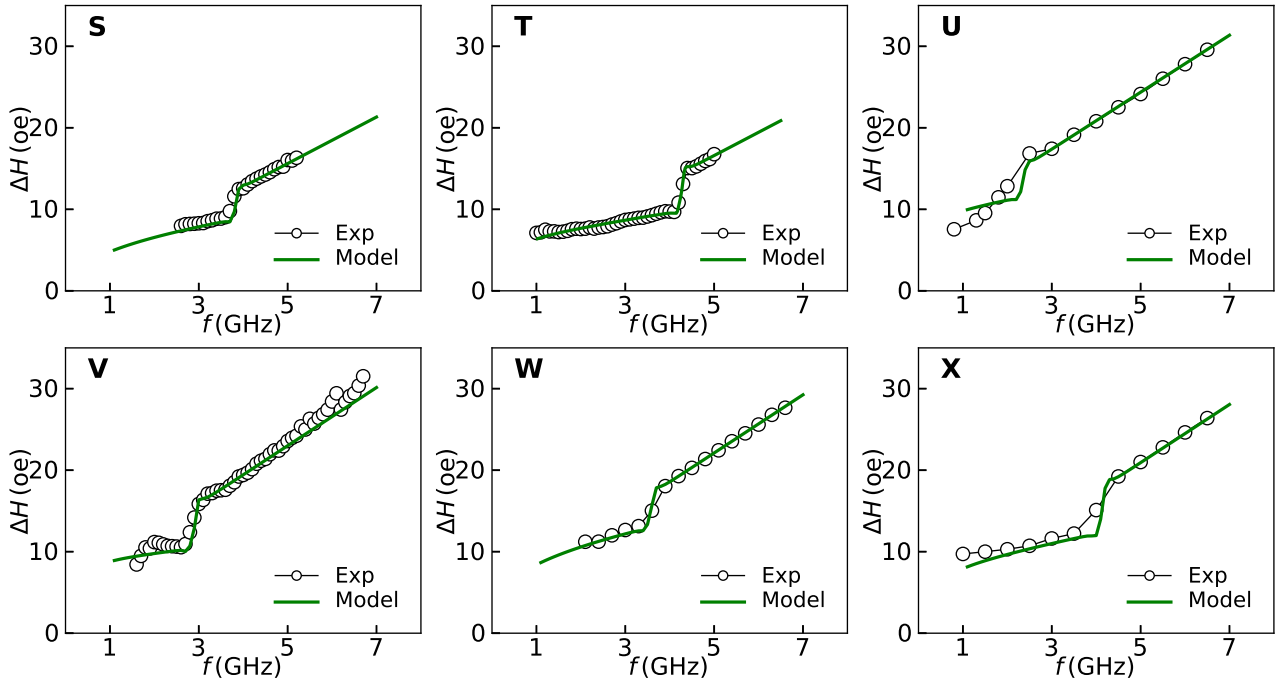

Figure 4.19: Field linewidth measurements vs. frequency for the acoustic mode of all samples.

Our experimental data is well-fitted to our LLG + ΔH_0 model with manually added ΔH_0 (see table 4.5) for each sample, except for a bit deviation in sample U and V. We believe this deviation comes from the perpendicular anisotropy field $H_\perp$, which we already explained in earlier section 4.5.

Samples						
Samples	S	T	U	V	W	X
ΔH_0 (Oe)	1.32	2.3	6.86	5.14	4.25	3.06
α	0.008	0.008	0.0098	0.011	0.010	0.010

Table 4.5: Damping α and inhomogeneous linewidth ΔH_0 used in figure 4.19

The ΔH results of optical mode for all samples are shown in figure 4.20.

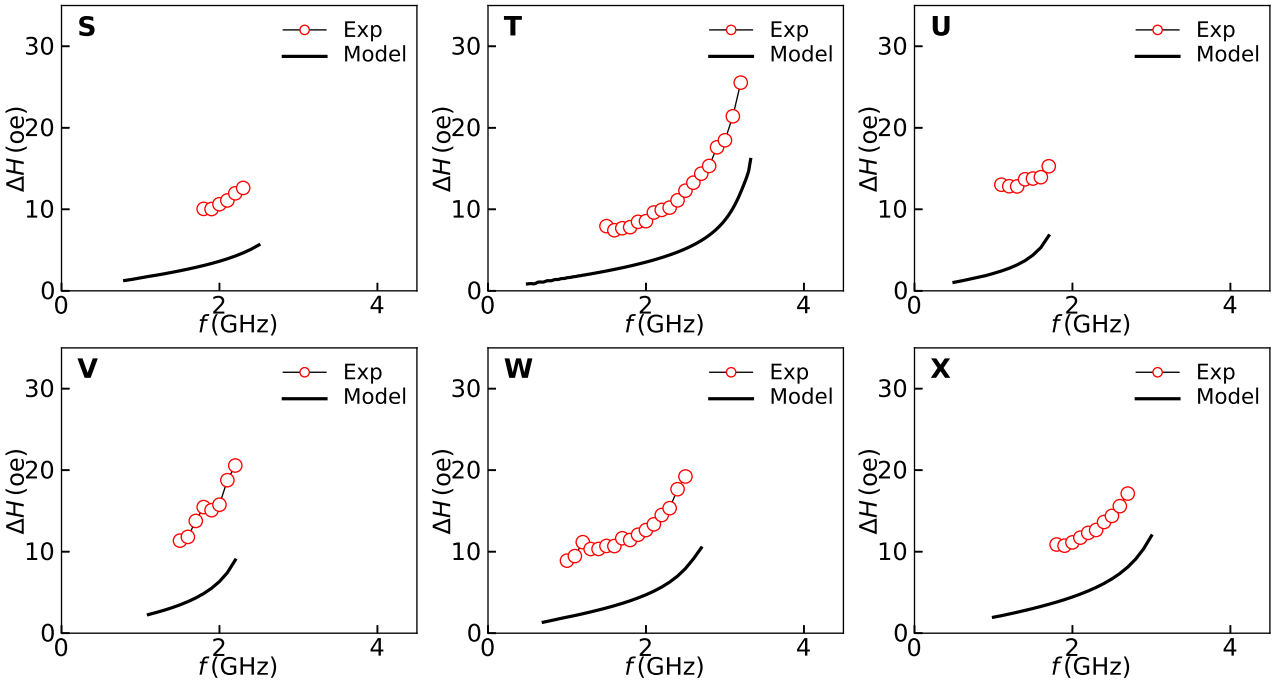

Figure 4.20: Field linewidth measurements vs. frequency for the optical mode

We can see a clear enhancement linewidth in all samples as compared to our LLG model. We believe that these linewidth enhancements to the optical mode out-of-phase oscillations, are due to the interlayer spins currents do not compensate each other. All the magnetic parameters used in calculation of linewidth ΔH and damping parameters α are given in table 4.5

4.7 Discussion

Our main results on analysis of ΔH in SAF systems are summarized in figures. 4.17, 4.18 , 4.19 and 4.20, where we present the experimental linewidth in both the saturated and spin flop states of a SAF system. We will first analyze the acoustic mode. For a symmetric SAF, as it is our case, we do not expect any linewidth enhancement due to interlayer spin pumping, as both spin currents compensate each other [51,68]. Thus, for a saturated state the linewidth ΔH should behave in the well known linear relation

$$\Delta H = 2\pi\alpha_0 f/\gamma + \Delta H_0 \tag{4.21}$$

where γ is the gyromagnetic ratio, α_0 is the intrinsic damping coefficient of the magnetic layers and ΔH_0 is the phenomenological inhomogeneous linewidth not predicted by the LLG theory. The sole addition of the ΔH_0 to the results from our LLG model ends in an excellent agreement with the experimental data not only for the saturated state but also for the spin flop state. This agreement with the LLG theory indicates that in fact, the interlayer spin current interactions do not produce any significant damping enhancement in neither saturated nor spin flop states. As the ΔH vs. f relationship in the spin flop region is almost linear, one could be temped to use equation 4.21 for this region, this would result in a lower damping parameter α and a larger ΔH_0, when expressed into a saturated state. But this interpretation is wrong. A better picture is obtained from the frequency linewidth Δf measurements (only calculated for sample T) that are almost continuous and slightly decrease with the field. Δf calculated from the LLG model, like the experimental data, does not show a transition between the magnetic states. In fact, the different ΔH slopes on the spin flop and saturated regions are governed by the slopes in their respective dispersion relation. This effect is clear in figure 4.19 where the transitions occur at different frequencies due to the different coupling fields in the samples.

On the contrary, in the case of the optical mode, we observe a disagreement between the LLG model and the experimental results. For this mode (see figure 4.18), the LLG model shows that Δf is smaller when compared to the acoustic mode and decreases with H in the spin flop region. While experimental Δf is larger for the optical mode and increases with field. Although the sharp increase over 200 Oe could be an experimental artifact due to the large slope of the dispersion relation over this field. Measured ΔH linewidth is also larger than the LLG model prediction. We correlate these linewidth enhancements to the optical mode out-of-phase oscillations, where the interlayer spins currents do not compensate each other.

4.8 Conclusions

In conclusion, we have measured the FMR response of a six SAF systems for both RF field perpendicular and parallel to the DC field to obtain the acoustic and optical FMR modes

responses. For these two modes, we obtained both, field and frequency linewidth, along the dispersion relations in the spin flop and saturated magnetic states. Our results for the acoustic mode are well explained by using the LLG equation with the addition of the inhomogeneous linewidth broadening, but without the need of additional spin torque terms. For the optical mode, we observed an increase in the experimental linewidth which should be explained by the non compensated interlayer spin currents in the SAF. Nevertheless, the LLG model already explained most of the features observed in the field linewidth measurements. Our results provide further insights into the magnetic damping behavior in SAF systems.

5 Spin current to charge current conversion in SAF systems

In this chapter, we study the spin current to charge current conversion in NiFe based bilayers and SAF systems. For this end we have measured the generated DC voltage in the samples due to spin currents exited by broadband ferromagnetic resonance. First section, will be dedicated to geometry considerations on the DC voltage signal generated by inverse spin hall effect. Second section, will be about spin to charge conversion in NiFe based systems. In third section, we present and discuss the measured DC voltages in SAF systems, in all their magnetic states.

5.1 Geometry considerations in ISHE

The voltage measured in ISHE experiments will depend not only on the ISHE angle of the materials used or polarization orientation of the spin currents, but also on the chosen polarity on the voltage terminals in the experimental setup. To show all this we considered two geometries of NiFe/Ru bilayers grown on Si/SiO_2 substrate. These samples are show in figure 5.1, in which, (a) NiFe is under the ruthenium and (b) NiFe is over the ruthenium layer. The direction of spin current J^S (presented by the black arrow) always flows from the ferromagnet towards the ruthenium layer.

Our experimental geometry for the ISHE measurements is shown in figure 5.2. According to this figure the magnetic field H is applied in the $\hat{y}$ direction and the radio frequency field h_{rf} is perpendicular to it. Due to the spin pumping induced by the ferromagnetic layer, the spin

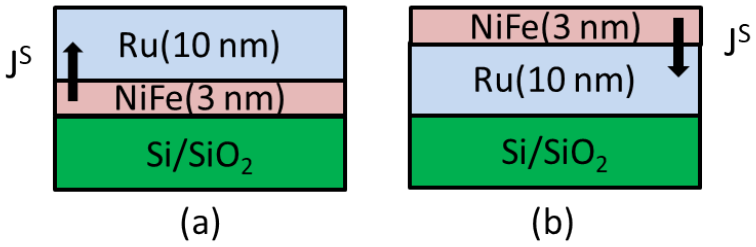

Figure 5.1: Samples for investigating ISHE, (a) NiFe/Ru, (b) Ru/NiFe

current J^S will flow in the $+\hat{z}$ or in the $-\hat{z}$ direction depending on the ferromagnet position in the sample stack. For saturated samples, the polarization of J^S will be along the H direction. The important parameter on our setup is the chosen polarity of the voltage terminals placed on top of the sample, that will determine the sign of the measured ISHE voltage. We place the $+V$ terminal on the $+\hat{x}$ side of the sample, while the $-V$ terminal is on the $-\hat{x}$ side.

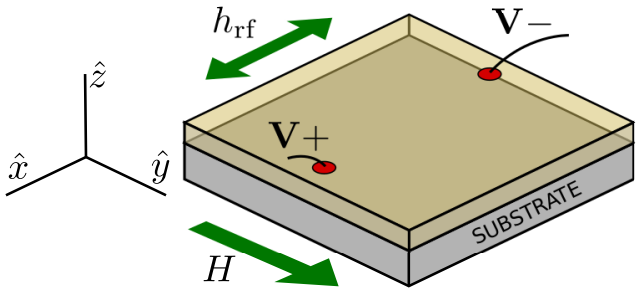

Figure 5.2: Geometry in ISHE experimental setup

Consider the sample shown in 5.1a, the J^S is flows towards $+\hat{z}$ axis, while, for $+H$, its polarization is in the $+\hat{y}$ direction. So only the $J^S{}_{\hat{z}\hat{y}}$ component is not zero and equation 2.26 takes the form

$$J^C_{\hat{x}} = -\frac{e}{\hbar}\,\Theta_{SH}\,\epsilon_{\hat{x}\hat{z}\hat{y}}\,J^S_{\hat{z}\hat{y}} \tag{5.1}$$

as ϵ_{xzy} = - 1, therefore, equation 5.1 becomes,

$$J^C = +\frac{e}{\hbar}\,\Theta_{SH}\,|J^S|\hat{x} \tag{5.2}$$

As Θ_{SH} is positive for Ru then the positive sign in equation 5.2 indicates that the electrical charge current will flow towards $+\hat{x}$ axis i.e. from $-V$ voltage terminal towards $+V$ voltage

terminal. Therefore, we will get $-V_{ISHE}$ for $+H$. If we reverse the direction of applied magnetic field, we will get $+V_{ISHE}$. For sample geometry shown in 5.1b, the spin current is J^S flowing towards $-\hat{z}$ axis, then the charge current J^C will flow towards $-x$ axis, and we get $+V_{ISHE}$ for $+H$ or $-V_{ISHE}$ for $-H$.

In figure 5.3 we show the measured ISHE voltages for the samples shown in figure 5.1. In this figure we observe the correct voltage signs predicted by the previously described theory, including the sign inversion on reversing the field direction and on inverting the layers order. We also observe the basic features of ISHE signals [67]: The maximum amplitude of V_{ISHE} is seen at the resonance fields of the NiFe. The V_{ISHE} peaks fields positions changes with the frequency following the FMR dispersion relation. And the peaks shape is almost symmetric around the resonance fields.

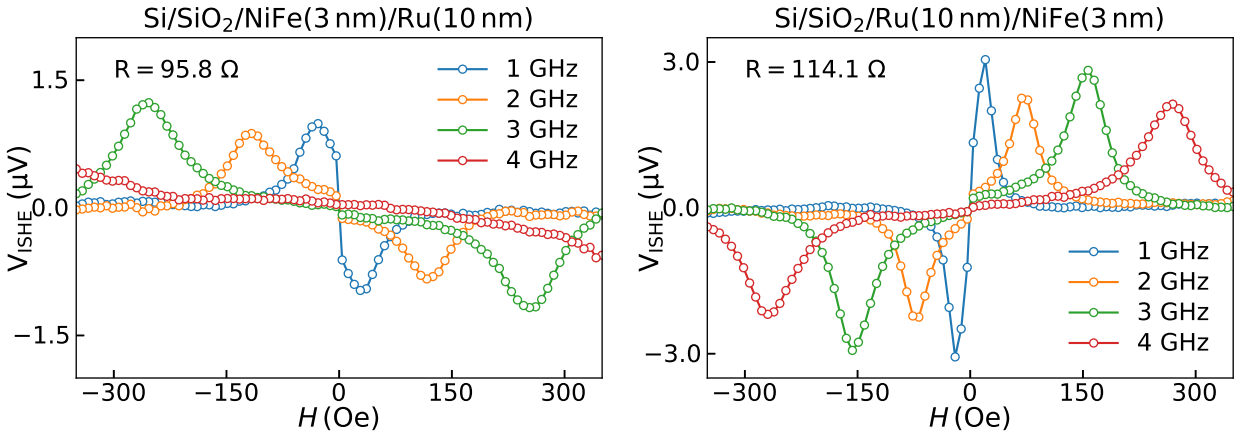

Figure 5.3: V_{ISHE} vs H response, over fixed frequencies for the samples presented in figure 5.1.

5.2 Spin to charge conversion in NiFe

ISHE is commonly used to study the spin orbit interactions in non-magnetic (NM) heavy metals in contact with a ferromagnet (FM) using FM/NM bilayers. At resonance frequency, the FM layer pumps a spin current into the NM layer and ISHE converts the spin current to charge current. In this experiments, it is very difficult to distinguish the contribution from the FM and from the NM layer in the conversion of spin to charge current, so this difference is

mostly neglected [67]. Self induced charge current can be generated in NiFe [103, 104] at room temperature, and it occurs through ISHE by spin orbit interactions in ferromagnets. This self induced voltage in NiFe samples are studied in details in ref [67, 105–107].

For a bilayer NiFe/Ru system, the overall voltage amplitude is a combination of NiFe and Ru layers contributions, mathematically:

$$\mathrm{V_{DC}(Total) = R\,J^{C}(Total) = R\,[J^{C}_{ISHE}(Ru) + J^{C}_{DC}(NiFe)]} \tag{5.3}$$

where R is the sample's resistance between the voltage contacts and $\mathrm{J^{C}_{DC}}$ are the charge currents. For convenience we express equation 5.3 in terms of the voltages generated by each layer, $\mathrm{V_{ISHE}(Ru) = R\,J^{C}_{ISHE}(Ru)}$ and $\mathrm{V_{DC}(NiFe) = R\,J^{C}_{DC}(NiFe)}$, and obtain

$$\mathrm{V_{DC}(Total) = V_{ISHE}(Ru) + V_{DC}(NiFe)} \tag{5.4}$$

although this interpretation has no direct physical significance as the Ru and NiFe contributions do not behave as two voltage sources connected in series.

For the geometry shown in figure 5.2 the signal contribution of a NM capping layer with positive Θ_{SH} is a negative ISHE voltage $-\mathrm{V_{ISHE}}$. While the NiFe layer produces a positive ISHE voltage $+\mathrm{V_{ISHE}}$ with amplitude dependant on the NiFe layer thickness. This can be seen in figure 5.4 where we present the measured DC voltage of this system, at 3.0 GHz, for different NiFe layer thickness. In this figure we observe that NiFe(3 nm)/Ru(10 nm) sample presents a negative voltage which correspond to the sign of $\mathrm{V_{ISHE}(Ru)}$. On the hand, the other samples with shows positive voltages, with increasing amplitude for thicker NiFe. All this observations are easily explained using equation 5.4. Where we can take $\mathrm{V_{ISHE}(Ru)}$ as a negative voltage with the same amplitude for all layers, while $\mathrm{V_{DC}(NiFe)}$ is positive, but its amplitude depends on the NiFe layer thickness.

To reinforce the fact that the DC voltage signal we observe in our experiments is dominated by the NiFe signal, we show in figure 5.5 measurements for NiFe/Pt and NiFe/Ta systems. Even if Pt and Ta have opposite ISHE angles, both systems produce positive voltages for all

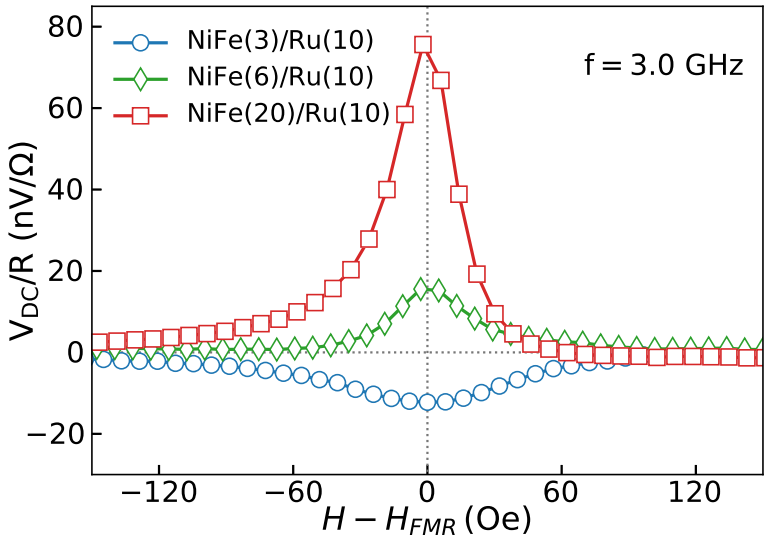

Figure 5.4: Measured DC voltage of NiFe/Ru systems for different NiFe layer thickness. In order to eliminate the geometry factors, the measured V_{DC} is divided by its corresponding sample's resistance R.

the excitation frequencies. But using equation 5.4 we can explain the difference in the amplitude of the signals. In the NiFe/Ta system both NM and NiFe contributions are positive, while in the NiFe/Pt system they are opposite. This results in a larger signal for NiFe/Ta and smaller signal for NiFe/Pt, yet still positive due to the NiFe contribution.

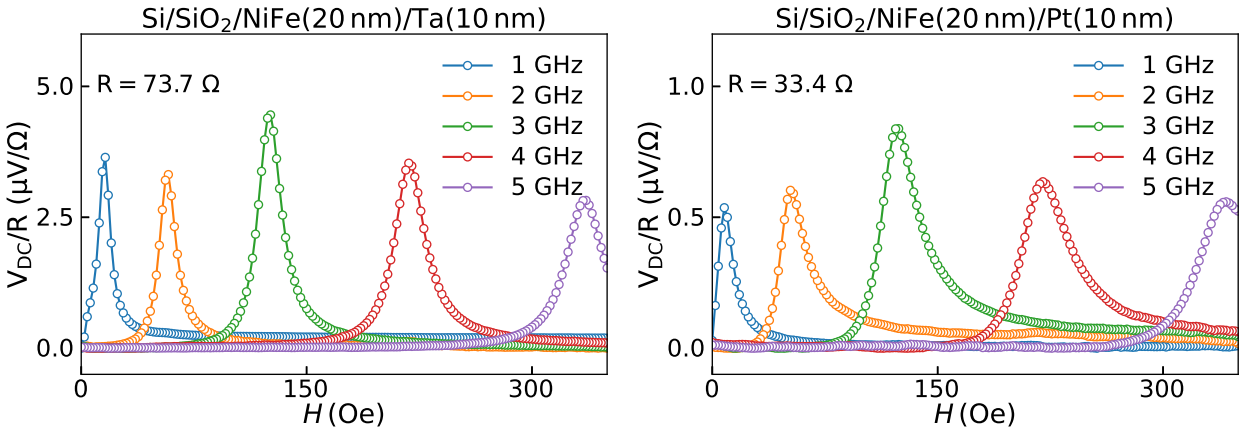

Figure 5.5: Generated V_{DC} signals for the NiFe/Ta and NiFe/Pt systems. Even if Pt and Ta have opposite ISHE angles, both systems produce positive voltages for $H > 0$ due to the NiFe V_{DC} contribution, that is larger than the V_{ISHE} in the capping layers .

5.3 Spin to charge conversion in SAF systems

In this section we analyse the generated V_{DC} due to FMR excitation in the SAF systems presented in chapter 4 (see figure 4.2). First we will show the complete picture of V_{DC} of sample T in all the magnetic states (saturation, spin flop and anti-parallel) and for a large range of frequencies. This is done in figure 5.6 where we plot the V_{DC} curves vs H measured at fixed excitation frequencies. These measurements were performed for frequencies ranging from 1 GHz up to 5 GHz with frequency steps of 0.2 GHz. The vertical offset of each V_{DC} series was chosen such that its baseline is aligned with its corresponding measurement frequency showed on the frequency scale on the right of the figure.

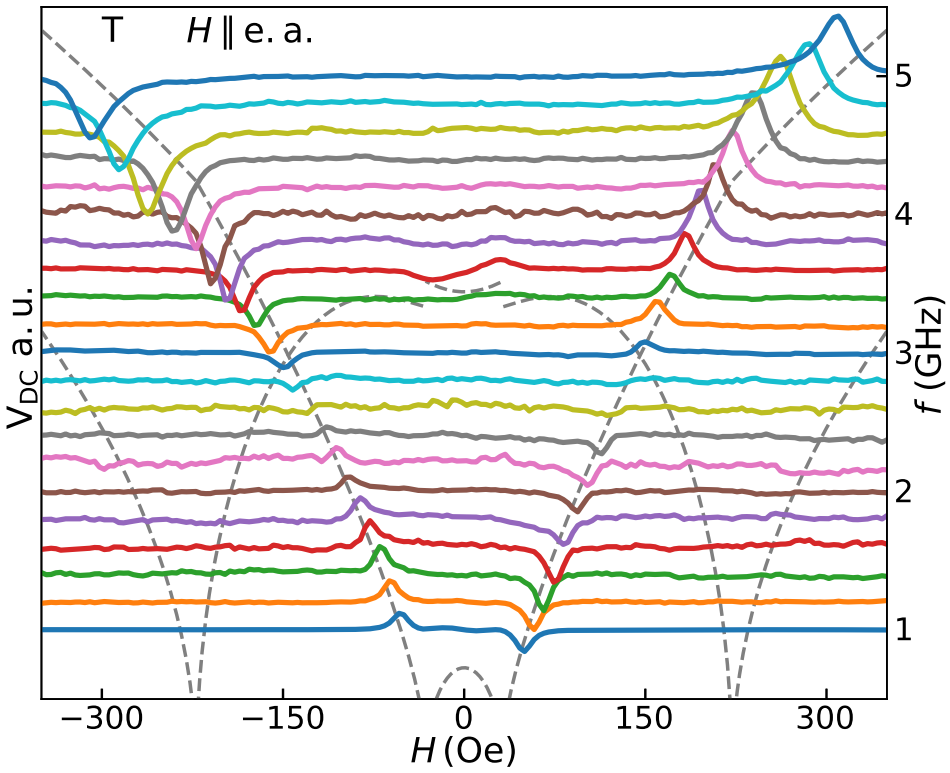

Figure 5.6: Measured DC voltages for a SAF system (sample T) for different fixed frequencies, along all the magnetization states. The vertical offset of each V_{DC} series is chosen such that its baseline is aligned with its measurement frequency on the frequency scale on the right. The dashed lines correspond to the dispersion relations of the FMR modes plotted against the right axis.

From figure 5.6 we observe two voltage peaks at each excitation frequency. The field position of these peaks follows the dispersion relation of the acoustic FMR mode (dashed lines). Also,

these peaks are almost symmetric with respect to the resonant field. In the regions far from the FMR condition the V_{DC} amplitude is very small. On the saturated state, for $+H$, the V_{DC} signal is positive and large when compared to the other magnetic states. The V_{DC} gradually reduces its peak intensity and then invert its sign in the spin flop region. This transition happens at around 2.6 GHz We have also noticed a V_{DC} signal corresponding to the FMR mode in the antiparallel state. For all the measured spectra we can see that the voltage is an odd function of H and behaves just like ISHE signals.

5.3.1 DC voltage sign inversion in the spin flop state

In this section, we will focus on the experimentally observed V_{DC} sign inversion on the spin flop state. We will show that this sign inversion is a feature of SAF systems and occurs when the angle between the top and bottom magnetization is 90°.

The V_{DC} sign inversion in the spin flop state for sample T is presented in figure 5.6. We also measured DC voltages for sample X in the spin flop state, for external field H parallel ($H \parallel e.a$) and perpendicular ($H \perp e.a$) to the anisotropy axis. These measurements are presented in figure 5.7, in both cases we observe the V_{DC} sign inversion. This inversion can be seen around the point where the layers' magnetization make an angle of 90°, which field H is marked by the vertical dotted line. This line crosses the dispersion relation at a frequency of around 2.5 GHz and 2.7 GHz for $H \parallel e.a$ and $H \perp e.a$, respectively. Thus the V_{DC} sign inversion is indeed related to the 90° angle between the layers' magnetization, independent on which field or frequency it occurs. The measured V_{DC} will be positive when this angle is smaller than 90° and negative when in larger than 90°

For Sample U, we have measured the V_{DC} in slip flop state for $H \parallel e.a.$ (see figure 5.8); V_{DC} amplitude signal is positive around resonance frequency of 2.0 GHz and gradually decrease in amplitude for lower frequency values and then the signal inverts just as the other samples, but for lower fields and frequencies due to the reduced coupling interactions. The peak positions and inversion of V_{DC} does not exactly follows the presented dispersion relation. This is probably an effect of the large out of plane anisotropy present in this sample (see section 4.5) that can also

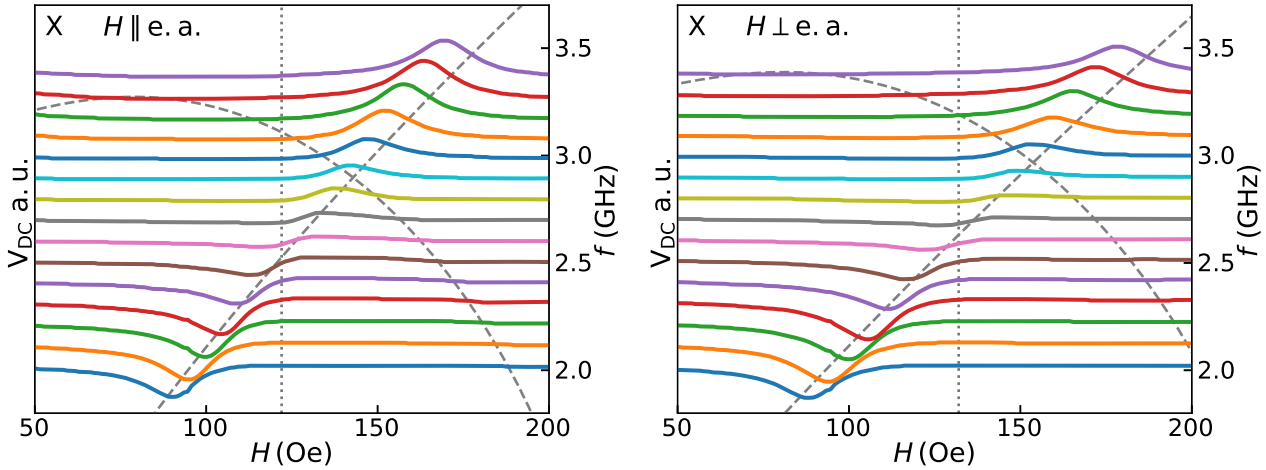

Figure 5.7: Measured DC voltages for sample X in the spin flop state, for H along (left) and perpendicular (right) to the anisotropy axis. The dashed lines correspond to the FMR dispersion relations and the dotted vertical line correspond to the field where the layers' magnetization make a 90°. The vertical offsets scheme is the same as in figure 5.6.

induce an out of plane magnetization component in the analyzed fields. Even so, we observe the V_{DC} sign inversion close to the calculated 90°, indicating that this effect is related to the magnetization directions in the SAF systems.

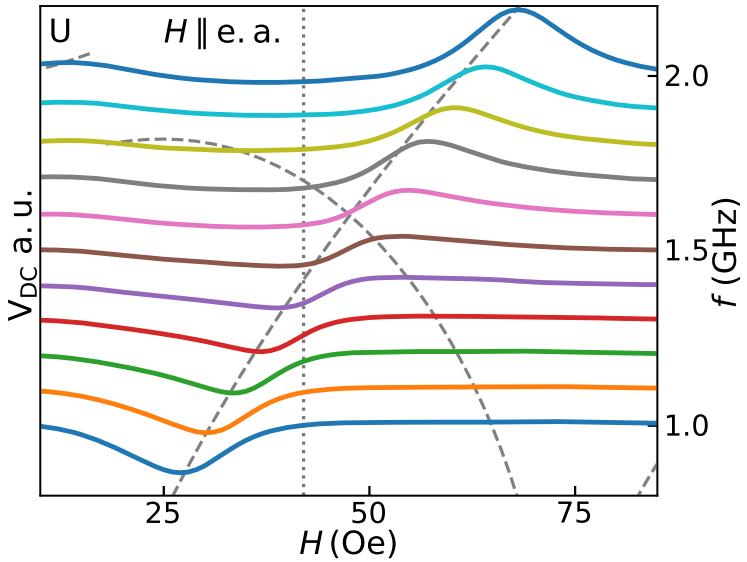

Figure 5.8: Measured DC voltages for sample U in the spin flop state. The dashed lines correspond to the FMR dispersion relations and the dotted vertical line correspond to the field where the layers' magnetization make a 90° angle. The vertical offsets scheme is the same as in figure 5.6.

5.3.2 DC voltage in the antiparallel state

In this section we focus on the experimental V_{DC} measured in the antiparallel state, this signal is shown in figure 5.9 for sample T and sample X. In both samples V_{DC} has a zero amplitude close to $H = 0$. Also, both samples show positive voltage amplitude $+V_{DC}$ for $+H$ and negative voltage amplitude $-V_{DC}$ for $-H$, this $+V_{DC}$ has an odd symmetry with H.

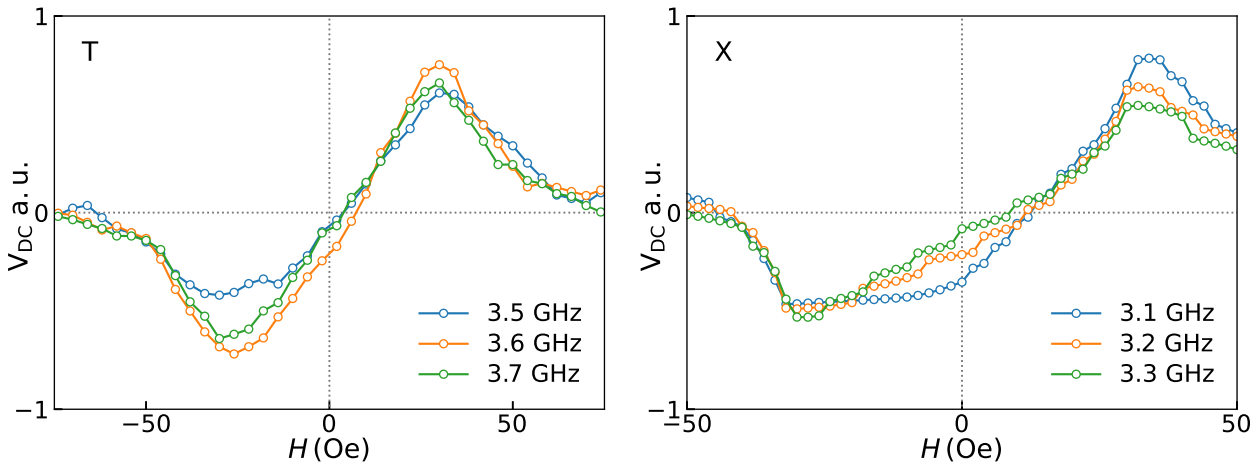

Figure 5.9: Measured DC voltages for samples T (left) and X (right) in the anti-parallel state. The chosen measurement frequencies are around the resonant frequency of the exited FMR mode in the anti-parallel state of each sample.

5.3.3 Discussion and conclusions

In the SAF systems we have measured a characteristic V_{DC} signal including a sign inversion in the spin flop state and a particular response in the antiparallel state. Here we will present a simple model that explains the signals measured for the saturated and antiparallel state, and discard other models presented in literature [108] as they do not reproduce the experimental data. We propose that each NiFe layer contributes independently with a DC voltage, due to the anisotropic magneto resistance AMR, that is proportional to the amplitude of oscillating part of the magnetization $|m_{osc}|$ and has a angle dependence like $\cos\phi\cos 2\phi$

$$V_{DC} \propto |m_{osc}| \cos\phi \cos 2\phi \tag{5.5}$$

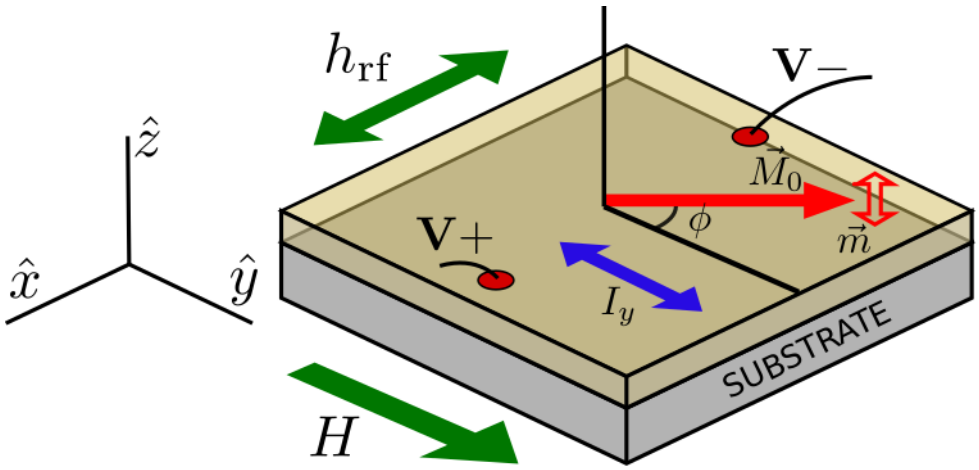

Figure 5.10: Schematic for measurements of V_{DC} of SAF. Magnetization vector $\vec{M}_0$, magnetization oscillating vector $\vec{m}$, angle between magnetization and easy axis ϕ, voltage terminals, directions of H and $h_{\rm rf}$ and induced a radio frequency current I_y (due to shortcircuit microstrip waveguide) are shown.

where ϕ is the angle between the layer's magnetization and the field direction.

We present this model using the figure 5.10. Here, the central conductor of the microstrip waveguide (not show) is along the $\hat{y}$ direction and generates a radio frequency field $h_{\rm rf}$ perpendicular to the external H field. This $h_{\rm rf}$ field, makes the magnetization oscillate and also induces, due to Lenz law, a radio frequency electric current I_y. This current has the same direction as the current in the central conductor of the microstrip waveguide, but opossite phase. I_y is related to a current density J_y and is proportional to the amplitude of $h_{\rm rf}$.

$$J_y = \frac{I_y}{A} \propto |h_{\rm rf}| \tag{5.6}$$

On the other hand, the total magnetization $\vec{M}$ is the sum of the static part $\vec{M}_0$ and the oscillating part $\vec{m}$.

$$\vec{M} = \vec{M}_0 + \vec{m} \tag{5.7}$$

The static magnetization $\vec{M}_0$ has an amplitude M_S and makes an angle ϕ with the electric

current I_y direction. So, we can write M_0 in terms of it's $\hat{x}$ and $\hat{y}$ components.

$$\vec{M_0} = M_S(\sin\phi\,\hat{x} + \cos\phi\,\hat{y}) \tag{5.8}$$

Similarly, the in plane oscillating part of $\vec{m}$ has an in plane amplitude $m_{\rm osc}$ and $\hat{x}$ and $\hat{y}$ components:

$$\vec{m} = -m_{\rm osc}(\cos\phi\,\hat{x} + \sin\phi\,\hat{y}) \tag{5.9}$$

with

$$m_{\rm osc} = \chi\cos\phi|h_{\rm rf}| \tag{5.10}$$

where χ is the in plane magnetic susceptibility and the $cos\phi$ term in this equation is due to the coupling efficiency between $h_{\rm rf}$ and $\vec{M_0}$

In order to obtain the spin rectification voltage V_{DC}, due to the coupling of the magnetization oscillation and the oscillating electric current, we start with the generalized Ohm law´s (see equation 2.5 in ref [93]).

$$E = \rho_\perp J + \frac{\Delta\rho_0}{H^2}(\vec{J}.\vec{H})H + \frac{\Delta\rho_0}{M^2}(\vec{J}.\vec{M})M - \frac{\rho_H}{|H|}(J\times H) - \frac{\rho_{AHE}}{|M|}(J\times M) \tag{5.11}$$

In this equation, we have included the nonlinear effects introduced by the presence of magnetic fields and a nonzero magnetization. The second and third terms describe ordinary magnetoresistance (OMR) and AMR respectively while the fourth and fifth terms describe the ordinary Hall effect (OHE) and the anomalous Hall effect (AHE). The AHE will not produce any voltage along the current direction due to the cross product, and therefore in a microstrip configuration there will be no AHE voltage along the length of the strip.

Taking only the AMR term

$$\vec{E} = \frac{\Delta\rho_0}{M_0^2}(\vec{J}.\vec{M})\vec{M} \tag{5.12}$$

and plugging the total magnetization $\vec{M} = \vec{M}_0 + \vec{m}$ expression, we get:

$$\vec{E} = \frac{\Delta\rho}{M_0^2}\left[(\vec{J}.\vec{M}_0)\vec{M}_0 + (\vec{J}.\vec{M}_0)\vec{m} + (\vec{J}.\vec{m})\vec{M}_0 + (\vec{J}.\vec{m})\vec{m}\right] \tag{5.13}$$

furthermore, to obtain V_{DC} we need to calculate the temporal average of the E field along the $\hat{x}$ direction, and multiply it by the distance l between the $+V$ and $-V$ electrodes. So, the first and last term of equation 5.13 will vanish as the first is constant and the former is very small, and we get:

$$-V_{DC} = <\vec{E}.\hat{x}> l = \frac{\Delta\rho}{M_0} l\left[- < J_y m_{osc} > \cos^2\phi + [< J_y m_{osc} > \sin^2\phi\right] \tag{5.14}$$

Finally, simplifying and using equations 5.10 and 5.6 we obtain:

$$V_{DC} \propto \frac{\Delta\rho}{M_0} l |h_{\mathrm{rf}}|^2 \chi \cos 2\phi \cos\phi \tag{5.15}$$

This equation is equivalent to equation 5.5 if we use $|m_{\mathrm{osc}}| = \chi|h_{\mathrm{rf}}|$ as the oscillating magnetization amplitude, which is independent of the radio frequency field coupling with the magnetization.

For our SAF system, we use this model and consider that the contribution from the Ru layer is negligible, which is in agreement with the experimental data seen in section 5.2. Using the same idea as in equations 5.3 and 5.4 we express the measured DC voltage as the voltage contributions from each layer

$$\mathrm{V}_{\mathrm{DC}}^{\mathrm{Total}} = \mathrm{V}_{\mathrm{DC}}^{\mathrm{T}} + \mathrm{V}_{\mathrm{DC}}^{\mathrm{B}} \tag{5.16}$$

or expressed in terms of $|m_{osc}|$ and ϕ

$$V_{DC}^{Total} \propto |m_{osc}^{T}| \cos\phi_T \cos 2\phi_T + |m_{osc}^{B}| \cos\phi_B \cos 2\phi_B \tag{5.17}$$

For the saturated states both magnetization are parallel to H and $\phi_B = \phi_T = \phi$, with $\phi = 0$ for $+H$ or $\phi = \pi$ for $-H$, also both oscillations are equal $m_{osc}^{T} = m_{osc}^{B} = m_{osc}$. Therefore, the solution to equation 5.17 in the saturated state is

$$V_{DC}^{Saturation} \propto \pm 2|m_{osc}| \tag{5.18}$$

which is positive for $+H$ and negative for $-H$ and agrees with the experimental data presented in figure 5.6.

In a antiparallel (AP) state, we suppose that the bottom layer is in $+H$ direction or $\phi_B = 0$ while for the top layer $\phi_T = \pi$ so we obtain:

$$V_{DC}^{AP\ state} \propto |m_{osc}^{B}| - |m_{osc}^{T}| \tag{5.19}$$

But, unlike the saturated state, the oscillations in the AP state are not equal, the layer oriented towards the field direction will have larger oscillation. This can be clearly seen in figure 5.11 where we present calculated oscillation amplitudes for the AP state. On the $+H$ side of the graph, the bottom layer has larger $|m_{osc}^{B}|$, while on the $-H$ the top layer oscillates with larger amplitude. The $|m_{osc}^{B}| - |m_{osc}^{T}|$ term is also shown in this figure and it has a similar shape observed to what is observed in the experimental voltage. The left panel of figure 5.11 shows that the experimental $V_{DC}^{AP\ state}$ does not have sharp transitions like the $|m_{osc}^{B}| - |m_{osc}^{T}|$ calculated with H oriented exactly towards the anisotropy axis (0° in the rigth panel of fig. 5.11). We attribute this to the expected anisotropy distributions present in the SAF that will smooth any sharp magnetic transition. For this reason we also included the calculation of $|m_{osc}^{B}| - |m_{osc}^{T}|$ when the H makes an angle of 10° with the anisotropy axis that behaves more like the experimental data.

For the spin flop region, in the acoustic mode, both oscillation have the same amplitude

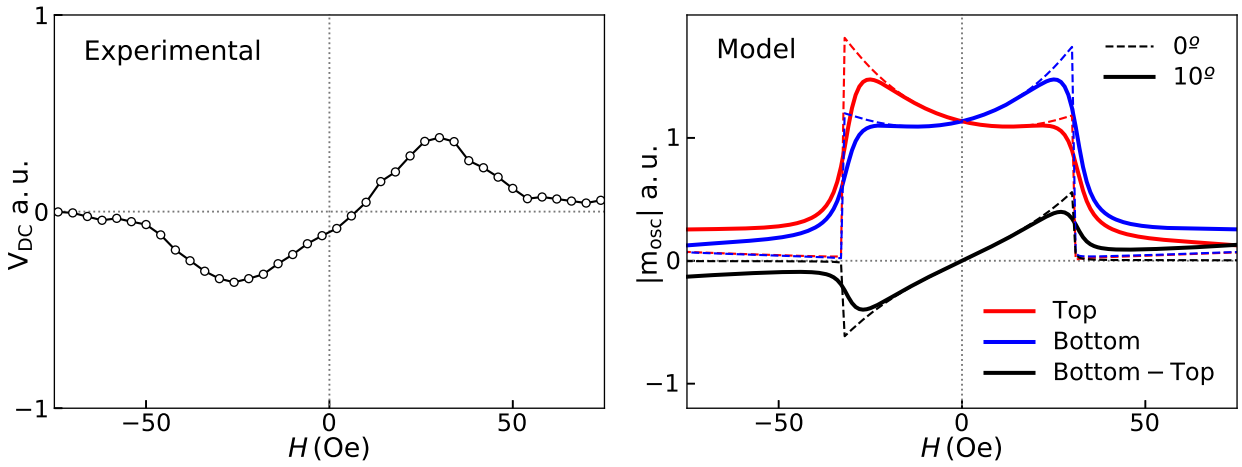

Figure 5.11: Left: Measured DC voltage at 3.6 GHz for sample T in the anti-parallel state. Right: Calculated in plane magnetization oscillation amplitudes $|m_{osc}|$ at 3.6 GHz, for the top and bottom layers of sample T, around the anti-parallel state. Note that the sharp transitions in $|m_{osc}|$ calculated for H parallel to the anisotropy axis (dashed lines) are smoothed for $|m_{osc}|$ calculated when H makes a 10 degree angle with the anisotropy axis (solid lines).

$|m_{osc}|$ and opposite angles $\phi_B = -\phi_T$. So, by using equation 5.17 we obtain:

$$V_{DC}^{\text{Spin flop}} \propto 2|m_{osc}| \cos\phi \cos 2\phi \tag{5.20}$$

Here, the $\cos 2\phi$ term will invert it sign when $\phi = \pm 45°$ and as both magnetization orientations deviate from each other, at this point the angle between the magnetization will be 90°. This $V_{DC}^{\text{Spin flop}}$ sign inversion is in accordance to the experiments.

Reference [108] proposed a model for the V_{DC} generated in a SAF system. This model propose/ suppose that V_{DC} is generated only by the ISHE on the capping layer due to only the top layer generated spin current. This implies that V_{DC} is proportional to $\cos\phi_T$. As seen earlier this model will fail for the antiparallel state as it were the V_{DC} solution should have a shape as the red line on the right panel of figure 5.11, and will also fail to explain the sign inversion in the spin flop state.

5.4 Conclusion

In the study of spin rectification, the effects that generate DC voltage were identified: the inverse spin Hall effect (ISHE) and the transverse anisotropic magnetoresistance (AMR) rectification, also known as the planar Hall effect. This second effect is due to the particular geometry of our measurement system, where the microstrip type waveguide used induces a radio frequency (RF) current in the sample. It is shown that the ISHE signal is observed for NiFe thin layers, while for layers larger than 10 nm the AMR effect is dominant. Spin rectification in SAFs was measured for the acoustic mode over the entire dispersion relation, including the antiparallel, non-collinear and saturated state. In the non-collinear state, the inversion of the DC voltage signal is observed and analyzed when the magnetization between the SAF layers makes an angle of 90^{o}. The antiparallel state also generates a DC voltage signal with an antisymmetric profile with respect to the zero field. These results are explained by the rectification of an RF current, induced in the sample, due to the anisotropic magnet resistance and result in the generation of a DC voltage transverse to the current direction.

In the future, we can further extend our work by studying the damping and linewidth in both ferromagnetic modes in systems with antiferromagnets e.g. SAF/AFM. In the future , we can use laser writer and e line to prepare the SAF structures in reduced dimensions, and study their dynamic magnetization properties. It will give us more understanding about the damping and linewidth in acoustic and optical ferromagnetic modes.

6 Conclusion and future perspectives

We have successfully prepared symmetric SAFs NiFe/Ru/NiFe with different capping layers of Pt, Ru and Ta. Moreover, we have investigated, not only the magnetization damping in SAFs using broadband ferromagnetic resonance but also calculated the field and frequency linewidth for both FMR dynamical modes of the system, i,e. acoustic and optical modes, were measured all along the dispersion relation. The obtained results were compared with a model based on the Landau Lifshitz Gilbert equation without additional spin pumping or spin torque terms. The results show that this model explains most of the features observed in the field linewidth measurements, with very good agreement for the acoustic mode, while for the optical mode it is clear that spin pumping is needed to explain the observed linewidth enhancement. Our results provide further insights into the magnetic damping behavior in SAF systems.

Furthermore, we have studied the geometric importance for ISHE measurements and moreover, we have prepared and studied the FM/NM, NM/FM and SAF/NM samples with FMR, for voltage measurements V_{DC} induced due to, (1) spin rectification (because of dynamic AMR, present in these systems by virtue of FMR radio frequency field h_{rf} and static field H) and (2) ISHE.

In the study of spin rectification, the effects that generate DC voltage were identified: the inverse spin Hall effect (ISHE) and the transverse anisotropic magnet resistance (AMR) rectification, also known as the planar Hall effect. This second effect is due to the particular geometry of our measurement system, where the microstrip type waveguide used induces a radio frequency (RF) current in the sample. It is shown that the ISHE signal is observed for NiFe thin layers, while for layers larger than 10 nm the AMR effect is dominant. Spin rectification

in SAFs was measured for the acoustic mode over the entire dispersion relation, including the antiparallel, non-collinear and saturated state. In the non-collinear state, the inversion of the DC voltage signal is observed and analyzed when the magnetization between the SAF layers makes an angle of 90^{o}. The antiparallel state also generates a DC voltage signal with an anti-symmetric profile with respect to the zero field. These results are explained by the rectification of an RF current, induced in the sample, due to the anisotropic magnetoresistance and result in the generation of a DC voltage transverse to the current direction.

In the future, we can further extend our work by studying the damping and linewidth in both ferromagnetic modes in non symmetric SAF systems, symmetric and non symmetric SAFs with antiferromagnets e.g. SAF/AFM. AMR spin rectification will be further studied in nano structures and and nano antennas. We can extend this work by preparing the SAF based on CoFe or CoFeB and study the AMR and ISHE. All these results will give us, more insight of these phenomena.

Bibliography

[1] M. N. Baibich, J. M. Broto, A. Fert, F. N. Van Dau, F. Petroff, P. Etienne, G. Creuzet, A. Friederich, and J. Chazelas, "Giant magnetoresistance of (001) fe/(001) cr magnetic superlattices," *Physical review letters*, vol. 61, no. 21, p. 2472, 1988.

[2] S. Wolf, D. Awschalom, R. Buhrman, J. Daughton, v. S. von Molnár, M. Roukes, A. Y. Chtchelkanova, and D. Treger, "Spintronics: a spin-based electronics vision for the future," *science*, vol. 294, no. 5546, pp. 1488–1495, 2001.

[3] I. Žutić, J. Fabian, and S. D. Sarma, "Spintronics: Fundamentals and applications," *Reviews of modern physics*, vol. 76, no. 2, p. 323, 2004.

[4] M.-H. Phan and H.-X. Peng, "Giant magnetoimpedance materials: Fundamentals and applications," *Progress in Materials Science*, vol. 53, no. 2, pp. 323–420, 2008.

[5] A. P. Guimarães, "Magnetism of thin films and multilayers," in *Principles of Nanomagnetism*, pp. 125–150, Springer, 2017.

[6] E. Montoya, T. Sebastian, H. Schultheiss, B. Heinrich, R. E. Camley, and Z. Celinski, "Magnetization dynamics," in *Handbook of Surface Science*, vol. 5, pp. 113–167, Elsevier, 2015.

[7] E. F. d. Silva, M. A. Corrêa, R. Della Pace, C. P. Cid, P. Kern, M. Carara, C. Chesman, O. A. Santos, R. Rodríguez-Suárez, A. Azevedo, *et al.*, "Thickness dependence of the magnetic anisotropy and dynamic magnetic response of ferromagnetic nife films," *Journal of Physics D: Applied Physics*, vol. 50, no. 18, p. 185001, 2017.

[8] A. Viegas, M. Corrêa, L. Santi, R. Da Silva, F. Bohn, M. Carara, and R. Sommer, "Thickness dependence of the high-frequency magnetic permeability in amorphous fe 73.5 cu 1 nb 3 si 13.5 b 9 thin films," *Journal of applied physics*, vol. 101, no. 3, p. 033908, 2007.

[9] R. Da Silva, M. Corrêa, E. Silva, T. Mori, R. Della Pace, R. Dutra, A. Viegas, F. Bohn, and R. Sommer, "Angular dependence of asymmetric magnetoimpedance in exchange biased nife/irmn multilayers," *Applied Physics Letters*, vol. 104, no. 10, p. 102405, 2014.

[10] E. F. d. Silva, M. Gamino, A. De Andrade, M. A. Corrêa, M. Vázquez, and F. Bohn, "Tunable asymmetric magnetoimpedance effect in ferromagnetic nife/cu/co films," *Applied Physics Letters*, vol. 105, no. 10, p. 102409, 2014.

[11] J. H. Griffiths, "Anomalous high-frequency resistance of ferromagnetic metals," *Nature*, vol. 158, no. 4019, pp. 670–671, 1946.

[12] C. Kittel, "On the theory of ferromagnetic resonance absorption," *Physical review*, vol. 73, no. 2, p. 155, 1948.

[13] S. Li, Q. Li, J. Xu, S. Yan, G.-X. Miao, S. Kang, Y. Dai, J. Jiao, and Y. Lü, "Tunable optical mode ferromagnetic resonance in fecob/ru/fecob synthetic antiferromagnetic trilayers under uniaxial magnetic anisotropy," *Advanced Functional Materials*, vol. 26, no. 21, pp. 3738–3744, 2016.

[14] M. Farle, "Ferromagnetic resonance of ultrathin metallic layers," *Reports on progress in physics*, vol. 61, no. 7, p. 755, 1998.

[15] S. S. Kalarickal, P. Krivosik, M. Wu, C. E. Patton, M. L. Schneider, P. Kabos, T. J. Silva, and J. P. Nibarger, "Ferromagnetic resonance linewidth in metallic thin films: Comparison of measurement methods," *Journal of Applied Physics*, vol. 99, no. 9, p. 093909, 2006.

[16] O. Mosendz, B. Kardasz, and B. Heinrich, "Dynamics studies in magnetic bilayer fe/ au/ fe (001) structures using network analyzer measurements," *Journal of applied physics*, vol. 99, no. 8, p. 08F303, 2006.

[17] C. Bilzer, T. Devolder, P. Crozat, C. Chappert, S. Cardoso, and P. Freitas, "Vector network analyzer ferromagnetic resonance of thin films on coplanar waveguides: Comparison of different evaluation methods," *Journal of applied physics*, vol. 101, no. 7, p. 074505, 2007.

[18] E. Montoya, T. McKinnon, A. Zamani, E. Girt, and B. Heinrich, "Broadband ferromagnetic resonance system and methods for ultrathin magnetic films," *Journal of magnetism and magnetic materials*, vol. 356, pp. 12–20, 2014.

[19] S. S. P. Parkin, N. More, and K. P. Roche, "Oscillations in exchange coupling and magnetoresistance in metallic superlattice structures: Co/ru, co/cr, and fe/cr," *Phys. Rev. Lett.*, vol. 64, pp. 2304–2307, May 1990.

[20] P. Bruno and C. Chappert, "Ruderman-kittel theory of oscillatory interlayer exchange coupling," *Phys. Rev. B*, vol. 46, pp. 261–270, Jul 1992.

[21] H.-G. Park, D. H. Yun, W. M. Jeong, O. Lee, and B.-C. Min, "Interlayer exchange coupling with ir/(ru, mo, or w)/ir composite spacers in perpendicular synthetic antiferromagnets," *Journal of the Korean Physical Society*, pp. 1–6, 2021.

[22] X. Liu, H. T. Nguyen, J. Ding, M. Cottam, and A. Adeyeye, "Interlayer coupling in ni 80 fe 20/ru/ni 80 fe 20 multilayer films: Ferromagnetic resonance experiments and theory," *Physical Review B*, vol. 90, no. 6, p. 064428, 2014.

[23] J. C. Slonczewski, "Conductance and exchange coupling of two ferromagnets separated by a tunneling barrier," *Physical Review B*, vol. 39, no. 10, p. 6995, 1989.

[24] S. Parkin, N. More, and K. Roche, "Oscillations in exchange coupling and magnetoresistance in metallic superlattice structures: Co/ru, co/cr, and fe/cr," *Physical review letters*, vol. 64, no. 19, p. 2304, 1990.

[25] P. Bruno, "Theory of interlayer magnetic coupling," *Physical Review B*, vol. 52, no. 1, p. 411, 1995.

[26] J. De Jong, I. Razdolski, A. Kalashnikova, R. Pisarev, A. Balbashov, A. Kirilyuk, T. Rasing, and A. Kimel, "Coherent control of the route of an ultrafast magnetic phase transition via low-amplitude spin precession," *Physical review letters*, vol. 108, no. 15, p. 157601, 2012.

[27] T. Chiba, G. E. Bauer, and S. Takahashi, "Magnetization damping in noncollinear spin valves with antiferromagnetic interlayer couplings," *Physical Review B*, vol. 92, no. 5, p. 054407, 2015.

[28] A. Veloso and P. P. Freitas, "Spin valve sensors with synthetic free and pinned layers," *J. Appl. Phys.*, vol. 87, no. 9, pp. 5744–5746, 2000.

[29] D. Apalkov, B. Dieny, and J. Slaughter, "Magnetoresistive random access memory," *Proc. IEEE*, vol. 104, no. 10, pp. 1796–1830, 2016.

[30] D. Houssameddine, J. Sierra, D. Gusakova, B. Delaet, U. Ebels, L. Buda-Prejbeanu, M.-C. Cyrille, B. Dieny, B. Ocker, J. Langer, *et al.*, "Spin torque driven excitations in a synthetic antiferromagnet," *Appl. Phys. Lett.*, vol. 96, no. 7, p. 072511, 2010.

[31] E. Monteblanco, F. Garcia-Sanchez, D. Gusakova, L. Buda-Prejbeanu, and U. Ebels, "Spin transfer torque nano-oscillators based on synthetic ferrimagnets: Influence of the exchange bias field and interlayer exchange coupling," *J. Appl. Phys.*, vol. 121, no. 1, p. 013903, 2017.

[32] R. A. Duine, K.-J. Lee, S. S. P. Parkin, and M. D. Stiles, "Synthetic antiferromagnetic spintronics," *Nature Physics*, vol. 14, pp. 217–219, Mar 2018.

[33] L. Avilés-Félix, A. Butera, D. E. González-Chávez, R. L. Sommer, and J. E. Gómez, "Pure spin current manipulation in antiferromagnetically exchange coupled heterostructures," *J. Appl. Phys.*, vol. 123, no. 12, p. 123904, 2018.

[34] A. Kamimaki, S. Iihama, K. Suzuki, N. Yoshinaga, and S. Mizukami, "Parametric amplification of magnons in synthetic antiferromagnets," *Phys. Rev. Applied*, vol. 13, p. 044036, Apr 2020.

[35] Z. Zhang, L. Zhou, P. E. Wigen, and K. Ounadjela, "Using ferromagnetic resonance as a sensitive method to study temperature dependence of interlayer exchange coupling," *Phys. Rev. Lett.*, vol. 73, pp. 336–339, Jul 1994.

[36] M. Belmeguenai, T. Martin, G. Woltersdorf, G. Bayreuther, V. Baltz, A. Suszka, and B. Hickey, "Microwave spectroscopy with vector network analyzer for interlayer exchange-coupled symmetrical and asymmetrical nife/ru/nife," *J. Phys.: Condens. Matter*, vol. 20, no. 34, p. 345206, 2008.

[37] H. Waring, Y. Li, C. Moutafis, I. J. Vera-Marun, and T. Thomson, "Magnetization dynamics in synthetic ferromagnetic thin films," *Physical Review B*, vol. 104, no. 1, p. 014419, 2021.

[38] S. Sorokin, R. Gallardo, C. Fowley, K. Lenz, A. Titova, G. P. Atcheson, G. Dennehy, K. Rode, J. Fassbender, J. Lindner, *et al.*, "Magnetization dynamics in synthetic antiferromagnets: Role of dynamical energy and mutual spin pumping," *Physical Review B*, vol. 101, no. 14, p. 144410, 2020.

[39] B. Heinrich, J. Cochran, M. Kowalewski, J. Kirschner, Z. Celinski, A. Arrott, and K. Myrtle, "Magnetic anisotropies and exchange coupling in ultrathin fcc co (001) structures," *Physical Review B*, vol. 44, no. 17, p. 9348, 1991.

[40] S.-s. Yan, R. Schreiber, F. Voges, C. Osthöver, and P. Grünberg, "Oscillatory interlayer coupling in fe/mn/fe trilayers," *Physical Review B*, vol. 59, no. 18, p. R11641, 1999.

[41] H. Du, Q. Xue, S. Li, G.-X. Miao, X.-M. Chu, Y. Dai, M. Yu, G. Zhao, and S. Yan, "[(fecob/ru/fecob)/zno] n superlattice multilayer: A real optical mode ferromagnetic resonance thick-film," *Applied Physics Letters*, vol. 116, no. 15, p. 152403, 2020.

[42] A. Layadi, "A theoretical investigation of ferromagnetic resonance linewidth and damping constants in coupled trilayer and spin valve systems," *AIP Advances*, vol. 5, no. 5, p. 057113, 2015.

[43] B. Buford, P. Dhagat, and A. Jander, "A technique for error estimation of linewidth and damping parameters extracted from ferromagnetic resonance measurements," *Journal of Applied Physics*, vol. 117, no. 17, p. 17E109, 2015.

[44] Y. Sun, H. Chang, M. Kabatek, Y.-Y. Song, Z. Wang, M. Jantz, W. Schneider, M. Wu, E. Montoya, B. Kardasz, *et al.*, "Damping in yttrium iron garnet nanoscale films capped by platinum," *Physical review letters*, vol. 111, no. 10, p. 106601, 2013.

[45] Z. Zhang, L. Zhou, P. E. Wigen, and K. Ounadjela, "Angular dependence of ferromagnetic resonance in exchange-coupled co/ru/co trilayer structures," *Phys. Rev. B*, vol. 50, pp. 6094–6112, Sep 1994.

[46] B. Negulescu, D. Lacour, M. Hehn, A. Gerken, J. Paul, and C. Duret, "On the control of spin flop in synthetic antiferromagnetic films," *J. Appl. Phys.*, vol. 109, no. 10, p. 103911, 2011.

[47] S. Sorokin, R. A. Gallardo, C. Fowley, K. Lenz, A. Titova, G. Y. P. Atcheson, G. Dennehy, K. Rode, J. Fassbender, J. Lindner, and A. M. Deac, "Magnetization dynamics in synthetic antiferromagnets: Role of dynamical energy and mutual spin pumping," *Phys. Rev. B*, vol. 101, p. 144410, Apr 2020.

[48] B. Heinrich, Y. Tserkovnyak, G. Woltersdorf, A. Brataas, R. Urban, and G. E. W. Bauer, "Dynamic exchange coupling in magnetic bilayers," *Phys. Rev. Lett.*, vol. 90, p. 187601, May 2003.

[49] Y. Tserkovnyak, A. Brataas, and G. E. W. Bauer, "Dynamic stiffness of spin valves," *Phys. Rev. B*, vol. 67, p. 140404, Apr 2003.

[50] J.-V. Kim and C. Chappert, "Magnetization dynamics in spin-valve structures with spin pumping," *J. Magn. Magn. Mater.*, vol. 286, pp. 56–60, 2005. Proceedings of the 5th International Symposium on Metallic Multilayers.

[51] S. Takahashi, "Giant enhancement of spin pumping in the out-of-phase precession mode," *Appl. Phys. Lett.*, vol. 104, no. 5, p. 052407, 2014.

[52] Y. Tserkovnyak, A. Brataas, and G. E. Bauer, "Enhanced gilbert damping in thin ferromagnetic films," *Physical review letters*, vol. 88, no. 11, p. 117601, 2002.

[53] K. Tanaka, T. Moriyama, M. Nagata, T. Seki, K. Takanashi, S. Takahashi, and T. Ono, "Linewidth broadening of optical precession mode in synthetic antiferromagnet," *Appl. Phys. Expr.*, vol. 7, p. 063010, jun 2014.

[54] A. A. Timopheev, Y. G. Pogorelov, S. Cardoso, P. P. Freitas, G. N. Kakazei, and N. A. Sobolev, "Dynamic exchange via spin currents in acoustic and optical modes of ferromagnetic resonance in spin-valve structures," *Phys. Rev. B*, vol. 89, p. 144410, Apr 2014.

[55] A. Kamimaki, S. Iihama, T. Taniguchi, and S. Mizukami, "All-optical detection and evaluation of magnetic damping in synthetic antiferromagnet," *Appl. Phys. Lett.*, vol. 115, no. 13, p. 132402, 2019.

[56] T. Chiba, G. E. W. Bauer, and S. Takahashi, "Magnetization damping in noncollinear spin valves with antiferromagnetic interlayer couplings," *Phys. Rev. B*, vol. 92, p. 054407, Aug 2015.

[57] M. Belmeguenai, T. Martin, G. Woltersdorf, M. Maier, and G. Bayreuther, "Frequency- and time-domain investigation of the dynamic properties of interlayer-exchange-coupled ni 81 fe 19/ ru/ ni 81 fe 19 thin films," *Physical Review B*, vol. 76, no. 10, p. 104414, 2007.

[58] A. Sud, C. W. Zollitsch, A. Kamimaki, T. Dion, S. Khan, S. Iihama, S. Mizukami, and H. Kurebayashi, "Tunable magnon-magnon coupling in synthetic antiferromagnets," *Phys. Rev. B*, vol. 102, p. 100403, Sep 2020.

[59] Y. Tserkovnyak, A. Brataas, G. E. Bauer, and B. I. Halperin, "Nonlocal magnetization dynamics in ferromagnetic heterostructures," *Reviews of Modern Physics*, vol. 77, no. 4, p. 1375, 2005.

[60] A. Manchon and S. Zhang, "Theory of spin torque due to spin-orbit coupling," *Physical Review B*, vol. 79, no. 9, p. 094422, 2009.

[61] M. Obstbaum, M. Härtinger, H. Bauer, T. Meier, F. Swientek, C. Back, and G. Woltersdorf, "Inverse spin hall effect in ni 81 fe 19/normal-metal bilayers," *Physical Review B*, vol. 89, no. 6, p. 060407, 2014.

[62] V. E. Demidov, S. Urazhdin, H. Ulrichs, V. Tiberkevich, A. Slavin, D. Baither, G. Schmitz, and S. O. Demokritov, "Magnetic nano-oscillator driven by pure spin current," *Nature materials*, vol. 11, no. 12, pp. 1028–1031, 2012.

[63] L. Liu, O. Lee, T. Gudmundsen, D. Ralph, and R. Buhrman, "Current-induced switching of perpendicularly magnetized magnetic layers using spin torque from the spin hall effect," *Physical review letters*, vol. 109, no. 9, p. 096602, 2012.

[64] M. Harder, Z. Cao, Y. Gui, X. Fan, and C.-M. Hu, "Analysis of the line shape of electrically detected ferromagnetic resonance," *Physical Review B*, vol. 84, no. 5, p. 054423, 2011.

[65] W. Zhang, B. Peng, F. Han, Q. Wang, W. T. Soh, C. K. Ong, and W. Zhang, "Separating inverse spin hall voltage and spin rectification voltage by inverting spin injection direction," *Applied Physics Letters*, vol. 108, no. 10, p. 102405, 2016.

[66] W. T. Soh, B. Peng, G. Chai, and C. Ong, "Note: Electrical detection and quantification of spin rectification effect enabled by shorted microstrip transmission line technique," *Review of Scientific Instruments*, vol. 85, no. 2, p. 026109, 2014.

[67] O. Gladii, L. Frangou, A. Hallal, R. Seeger, P. Noël, G. Forestier, S. Auffret, M. Rubio-Roy, P. Warin, L. Vila, *et al.*, "Self-induced inverse spin hall effect in ferromagnets: Demonstration through nonmonotonic temperature dependence in permalloy," *Physical Review B*, vol. 100, no. 17, p. 174409, 2019.

[68] H. Yang, Y. Li, and W. E. Bailey, "Large spin pumping effect in antisymmetric precession of ni79fe21/ru/ni79fe21," *Appl. Phys. Lett.*, vol. 108, no. 24, p. 242404, 2016.

[69] S. Chikazumi, "Physics of magnetism john wiley," *New York*, 1964.

[70] H. Kronmuller, H. Kronmüller, and M. Fähnle, *Micromagnetism and the microstructure of ferromagnetic solids*. Cambridge university press, 2003.

[71] G. Bertotti, *Hysteresis in magnetism: for physicists, materials scientists, and engineers*. Gulf Professional Publishing, 1998.

[72] A. Hubert and R. Schäfer, *Magnetic domains: the analysis of magnetic microstructures*. Springer Science & Business Media, 2008.

[73] J. Osborn, "Demagnetizing factors of the general ellipsoid," *Physical review*, vol. 67, no. 11-12, p. 351, 1945.

[74] A. Aharoni, "Demagnetizing factors for rectangular ferromagnetic prisms," *Journal of applied physics*, vol. 83, no. 6, pp. 3432–3434, 1998.

[75] A. Harres and J. Geshev, "A polycrystalline model for magnetic exchange bias," *Journal of Physics: Condensed Matter*, vol. 24, no. 32, p. 326004, 2012.

[76] T. L. Gilbert, "A phenomenological theory of damping in ferromagnetic materials," *IEEE transactions on magnetics*, vol. 40, no. 6, pp. 3443–3449, 2004.

[77] A. Barman and A. Haldar, "Time-domain study of magnetization dynamics in magnetic thin films and micro-and nanostructures," *Solid State Physics*, vol. 65, pp. 1–108, 2014.

[78] C. Diego, *Magnetic properties of thin films: a study by ferromagnetic resonance broadband:*. PhD thesis, Centro Brasileiro de Pesquisas Físicas, 2013.

[79] L. Lu, *Damping mechanisms in magnetic recording materials & microwave-assisted magnetization reversal*. PhD thesis, Colorado State University, 2014.

[80] J. Smith and H. Beljers, "Ferromagnetic resonance absorbtion in bafe12o19, a highly anisotropic crystall," *Philips Res. Rep*, vol. 10, pp. 113–130, 1955.

[81] R. Silsbee, A. Janossy, and P. Monod, "Coupling between ferromagnetic and conduction-spin-resonance modes at a ferromagnetic—normal-metal interface," *Physical Review B*, vol. 19, no. 9, p. 4382, 1979.

[82] Y. Tserkovnyak, A. Brataas, and G. E. Bauer, "Spin pumping and magnetization dynamics in metallic multilayers," *Physical Review B*, vol. 66, no. 22, p. 224403, 2002.

[83] E. Saitoh, M. Ueda, H. Miyajima, and G. Tatara, "Conversion of spin current into charge current at room temperature: Inverse spin-hall effect," *Applied physics letters*, vol. 88, no. 18, p. 182509, 2006.

[84] A. Brataas, Y. V. Nazarov, and G. E. Bauer, "Finite-element theory of transport in ferromagnet–normal metal systems," *Physical Review Letters*, vol. 84, no. 11, p. 2481, 2000.

[85] K. Ando and E. Saitoh, "Observation of the inverse spin hall effect in silicon," *Nature communications*, vol. 3, no. 1, pp. 1–6, 2012.

[86] M. B. Jungfleisch, *Spin pumping and inverse spin Hall effect in yttrium iron garnet/platinum heterostructures*. PhD thesis, Citeseer, 2013.

[87] M. I. Dyakonov and A. Khaetskii, *Spin physics in semiconductors*, vol. 157. Springer, 2008.

[88] M. Tsoi, A. Jansen, J. Bass, W.-C. Chiang, V. Tsoi, and P. Wyder, "Generation and detection of phase-coherent current-driven magnons in magnetic multilayers," *Nature*, vol. 406, no. 6791, pp. 46–48, 2000.

[89] S. I. Kiselev, J. Sankey, I. Krivorotov, N. Emley, R. Schoelkopf, R. Buhrman, and D. Ralph, "Microwave oscillations of a nanomagnet driven by a spin-polarized current," *nature*, vol. 425, no. 6956, pp. 380–383, 2003.

[90] M. Costache, S. Watts, M. Sladkov, C. Van Der Wal, and B. Van Wees, "Large cone angle magnetization precession of an individual nanopatterned ferromagnet with dc electrical detection," *Applied Physics Letters*, vol. 89, no. 23, p. 232115, 2006.

[91] M. Costache, M. Sladkov, S. Watts, C. Van Der Wal, and B. Van Wees, "Electrical detection of spin pumping due to the precessing magnetization of a single ferromagnet," *Physical review letters*, vol. 97, no. 21, p. 216603, 2006.

[92] J. Sankey, P. Braganca, and A. Garcia, "In kriv orotov, ra buhrman, and dc ralph," *Phys. Rev. Lett*, vol. 96, p. 227601, 2006.

[93] M. Harder, Y. Gui, and C.-M. Hu, "Electrical detection of magnetization dynamics via spin rectification effects," *Physics Reports*, vol. 661, pp. 1–59, 2016.

[94] T. McGuire and R. Potter, "Anisotropic magnetoresistance in ferromagnetic 3d alloys," *IEEE Transactions on Magnetics*, vol. 11, no. 4, pp. 1018–1038, 1975.

[95] A. Malozemoff, "Anisotropic magnetoresistance of amorphous and concentrated polycrystalline iron alloys," *Physical Review B*, vol. 32, no. 9, p. 6080, 1985.

[96] D. Roberta, *Magnetization dynamics in Magnetic Multilayers and Magnetic Micro / Nanoobjects:*. PhD thesis, Centro Brasileiro de Pesquisas Físicas, 2014.

[97] M. Yasaka *et al.*, "X-ray thin-film measurement techniques," *The Rigaku Journal*, vol. 26, no. 2, pp. 1–9, 2010.

[98] G. Woltersdorf, *Spin-pumping and two-magnon scattering in magnetic multilayers*. PhD thesis, Sinon Fraser University, 2004.

[99] E. Abarra, A. Inomata, H. Sato, I. Okamoto, and Y. Mizoshita, "Longitudinal magnetic recording media with thermal stabilization layers," *Applied Physics Letters*, vol. 77, no. 16, pp. 2581–2583, 2000.

[100] E. E. Fullerton, D. Margulies, M. E. Schabes, M. Carey, B. Gurney, A. Moser, M. Best, G. Zeltzer, K. Rubin, H. Rosen, *et al.*, "Antiferromagnetically coupled magnetic media layers for thermally stable high-density recording," *Applied Physics Letters*, vol. 77, no. 23, pp. 3806–3808, 2000.

[101] D. Gusakova, D. Houssameddine, U. Ebels, B. Dieny, L. Buda-Prejbeanu, M. Cyrille, and B. Delaët, "Spin-polarized current-induced excitations in a coupled magnetic layer system," *Physical Review B*, vol. 79, no. 10, p. 104406, 2009.

[102] Z. Zhang, L. Zhou, P. Wigen, and K. Ounadjela, "Angular dependence of ferromagnetic resonance in exchange-coupled co/ru/co trilayer structures," *Physical Review B*, vol. 50, no. 9, p. 6094, 1994.

[103] A. Tsukahara, Y. Ando, Y. Kitamura, H. Emoto, E. Shikoh, M. P. Delmo, T. Shinjo, and M. Shiraishi, "Self-induced inverse spin hall effect in permalloy at room temperature," *Physical Review B*, vol. 89, no. 23, p. 235317, 2014.

[104] O. Mosendz, V. Vlaminck, J. Pearson, F. Fradin, G. Bauer, S. Bader, and A. Hoffmann, "Detection and quantification of inverse spin hall effect from spin pumping in permalloy/normal metal bilayers," *Physical Review B*, vol. 82, no. 21, p. 214403, 2010.

[105] B. Miao, S. Huang, D. Qu, and C. Chien, "Inverse spin hall effect in a ferromagnetic metal," *Physical review letters*, vol. 111, no. 6, p. 066602, 2013.

[106] A. Azevedo, R. Cunha, F. Estrada, O. A. Santos, J. Mendes, L. Vilela-Leão, R. Rodríguez-Suárez, and S. Rezende, "Electrical detection of ferromagnetic resonance in single layers of permalloy: Evidence of magnonic charge pumping," *Physical Review B*, vol. 92, no. 2, p. 024402, 2015.

[107] Y. Omori, E. Sagasta, Y. Niimi, M. Gradhand, L. E. Hueso, F. Casanova, and Y. Otani, "Relation between spin hall effect and anomalous hall effect in 3 d ferromagnetic metals," *Physical Review B*, vol. 99, no. 1, p. 014403, 2019.

[108] L. Avilés-Félix, A. Butera, D. González-Chávez, R. Sommer, and J. E. Gomez, "Pure spin current manipulation in antiferromagnetically exchange coupled heterostructures," *Journal of Applied Physics*, vol. 123, no. 12, p. 123904, 2018.